NUREG/CR-4667, Vol. 36
ANL-06/33

Environmentally Assisted Cracking in Light Water Reactors

Annual Report
January – December 2005

Argonne National Laboratory

U.S. Nuclear Regulatory Commission
Office of Nuclear Regulatory Research
Washington, DC 20555-0001

NUREG/CR-4667, Vol. 36
ANL-06/33

Environmentally Assisted Cracking in Light Water Reactors

Annual Report
January – December 2005

Manuscript Completed: August 2006
Date Published: August 2007

Prepared by
B. Alexandreanu, Y. Chen, O.K. Chopra, H.M. Chung, E.E. Gruber, W.J. Shack, and W.K. Soppet

Argonne National Laboratory
9700 South Cass Avenue
Argonne, IL 60439

S. Crane, NRC Project Manager

Prepared for
Division of Fuel, Engineering and Radiological Research
Office of Nuclear Regulatory Research
U.S. Nuclear Regulatory Commission
Washington, DC 20555-0001
NRC Job Code Y6388

Previous Documents in Series

Environmentally Assisted Cracking in Light Water Reactors Semiannual Report
April-September 1985, NUREG/CR-4667 Vol. I, ANL-86-31 (June 1986).
October 1985-March 1986, NUREG/CR-4667 Vol. II, ANL-86-37 (September 1987).
April-September 1986, NUREG/CR-4667 Vol. III, ANL-87-37 (September 1987).
October 1986-March 1987, NUREG/CR-4667 Vol. IV, ANL-87-41 (December 1987).
April-September 1987, NUREG/CR-4667 Vol. V, ANL-88-32 (June 1988).
October 1987-March 1988, NUREG/CR-4667 Vol. 6, ANL-89/10 (August 1989).
April-September 1988, NUREG/CR-4667 Vol. 7, ANL-89/40 (March 1990).
October 1988-March 1989, NUREG/CR-4667 Vol. 8, ANL-90/4 (June 1990).
April-September 1989, NUREG/CR-4667 Vol. 9, ANL-90/48 (March 1991).
October 1989-March 1990, NUREG/CR-4667 Vol. 10, ANL-91/5 (March 1991).
April-September 1990, NUREG/CR-4667 Vol. 11, ANL-91/9 (May 1991).
October 1990-March 1991, NUREG/CR-4667 Vol. 12, ANL-91/24 (August 1991).
April-September 1991, NUREG/CR-4667 Vol. 13, ANL-92/6 (March 1992).
October 1991--March 1992, NUREG/CR-4667 Vol. 14, ANL-92/30 (August 1992).
April-September 1992, NUREG/CR-4667 Vol. 15, ANL-93/2 (June 1993).
October 1992-March 1993, NUREG/CR-4667 Vol. 16, ANL-93/27 (September 1993).
April-September 1993, NUREG/CR-4667 Vol. 17, ANL-94/26 (June 1994).
October 1993-March 1994, NUREG/CR-4667 Vol. 18, ANL-95/2 (March 1995).
April-September 1994, NUREG/CR-4667 Vol. 19, ANL-95/25 (September 1995).
October 1994-March 1995, NUREG/CR-4667 Vol. 20, ANL-95/41 (January 1996).
April-December 1995, NUREG/CR-4667 Vol. 21, ANL-96/1 (July 1996).
January 1996-June 1996, NUREG/CR-4667 Vol. 22, ANL-97/9 (June 1997).
July 1996-December 1996, NUREG/CR-4667 Vol. 23, ANL-97/10 (October 1997).
January 1997-June 1997, NUREG/CR-4667 Vol. 24, ANL-98/6 (April 1998).
July 1997-December 1997, NUREG/CR-4667 Vol. 25, ANL-98/18 (September 1998).
January 1998-June 1998, NUREG/CR-4667 Vol. 26, ANL-98/30 (December 1998).
July 1998-December 1998, NUREG/CR-4667 Vol. 27, ANL-99/11 (October 1999).
January 1999-June 1999, NUREG/CR-4667 Vol. 28, ANL-00/7 (July 2000).
July 1999-December 1999, NUREG/CR-4667 Vol. 29, ANL-00/23 (November 2000).
January 2000-June 2000, NUREG/CR-4667 Vol. 30, ANL-01/08 (June 2001).
July 200-December 2000, NUREG/CR-4667 Vol. 31, ANL-01/09 (April 2002).
Environmentally Assisted Cracking in Light Water Reactors Annual Report
January-December 2001, NUREG/CR-4667 Vol. 32, ANL-02/33 (June 2003).
January-December 2002, NUREG/CR-4667 Vol. 33, ANL-03/36 (June 2005).
January-December 2003, NUREG/CR-4667 Vol. 34, ANL-05/17 (May 2006).
January-December 2004, NUREG/CR-4667 Vol. 35, ANL-05/31 (September 2006).

Abstract

This report summarizes work performed from January to December 2005 by Argonne National Laboratory on fatigue and environmentally assisted cracking in light water reactors (LWRs).

Existing statistical models for estimating the fatigue life of carbon and low-alloy steels and austenitic stainless steels (SSs) as a function of material, loading, and environmental conditions were updated. Also, the ASME Code fatigue adjustment factors of 2 on stress and 20 on life were critically reviewed to assess the possible conservatism in the current choice of the margins. An approach, based on an environmental fatigue correction factor, for incorporating the effects of LWR environments into ASME Section III fatigue evaluations is discussed**.**

The susceptibility of austenitic stainless steels and their welds to irradiation-assisted stress corrosion cracking (IASCC) is being evaluated as a function of the fluence level, water chemistry, material chemistry, and fabrication history. For this task, crack growth rate (CGR) tests and slow strain rate tensile (SSRT) tests are being conducted on various austenitic SSs irradiated in the Halden boiling water reactor. The SSRT tests are currently focused on investigating the effects of the grain boundary engineering process on the IASCC of the austenitic SSs. The CGR tests were conducted on Type 316 SSs irradiated to 0.45-3.0 dpa, and on sensitized Type 304 SS and SS weld heat-affected-zone material irradiated to 2.16 dpa. The CGR tests on materials irradiated to 2.16 dpa were followed by a fracture toughness test in a water environment. The effects of material composition, irradiation, and water chemistry on growth rates are discussed.

The susceptibility of austenitic SS core internals to IASCC and void swelling is also being evaluated for pressurized water reactors. Both SSRT tests and microstructural examinations are being conducted on specimens irradiated in the BOR-60 reactor in Russia to doses up to 20 dpa.

Crack growth rate data, obtained in the pressurized water reactor environment, are presented on Ni-alloy welds prepared in the laboratory or obtained from the nozzle-to-pipe weld of the V. C. Summer reactor. The experimental CGRs under cyclic and constant load are compared with the existing CGR data for Ni-alloy welds to determine the relative susceptibility of these materials to environmentally enhanced cracking under a variety of loading conditions.

This page is intentionally left blank

Foreword

For more than 35 years, Argonne National Laboratory (ANL) has served the U.S. Nuclear Regulatory Commission (NRC), Office of Nuclear Regulatory Research (RES), as a prime contractor for studies of the environmental degradation of structural materials in light-water reactor environments. As Volume 36 in the NUREG/CR-4667 series, this document represents the annual report of ANL program studies for Calendar Year 2005. The program is divided into four tasks:

- Task 1 focused on the environmental degradation of fatigue life of pressure boundary materials, and has concluded. This report briefly reviews the main findings.
- Task 2 addresses irradiation-assisted stress-corrosion cracking (IASCC) of stainless steels in boiling-water reactor (BWR) environments, while the parallel program in Task 3 addresses IASCC of stainless steels in pressurized-water reactor (PWR) environments. The effort in Task 2 is nearing completion, while the effort in Task 3 is increasing accordingly.
- Task 4, the study of crack growth rates in nickel-base alloys typically used in vessel penetrations, is currently focused on testing Alloy 600 and its associated weld metals, Alloys 82 and 182, and has begun the transition toward testing the more resistant Alloys 152 and 690, which are used in replacement components and new reactor structures.

Task 1 studies of the environmental degradation of fatigue life of pressure boundary materials was closed out this year. During 2006, the contractor and NRC staff completed Draft Regulatory Guide 1144, dated July 2006, which proposed new design curves and a revised methodology for incorporating the effects of the coolant environment in calculations of the degradation of fatigue life for light-water reactor components. In March 2007, the NRC formally released this guidance as Regulatory Guide 1.207, which represents the culmination of about 25 years of experimental programs in this area.

The Task 2 and 3 evaluations of the effects of irradiation on mechanical properties, stress-corrosion cracking, and fracture toughness of stainless steels and nickel-base alloys used in reactor core internal structures are a major part of the ANL program. In addition, Task 3 crack growth rate testing of Type 304 and 304L stainless steel heat-affected zones continued to establish the threshold for IASCC as functions of material composition, water chemistry, and irradiation damage. Future stress-corrosion cracking tests will be conducted in simulated PWR coolant chemistry on stainless steels with greater irradiation damage, and the IASCC tests will be augmented by microstructural characterization of such materials, to assess the effects of radiation-induced segregation of the alloy constituents.

Task 4 evaluations of the stress-corrosion crack growth resistance of nickel-base alloys continued during this period, and will continue for the duration of this program. Nonetheless, emphasis in this area is shifting toward testing of specimens taken from discarded or replaced reactor components, to assist in root cause analysis and to assess any effects of aging under normal operating reactor conditions.

This report contains primary water stress-corrosion cracking data for weldments removed from hot leg “A” of the Virgil C. Summer Nuclear Station. In future years, the stress-corrosion cracking studies of nickel-base alloys will begin to focus more on Alloy 690 and its associated weld metal, Alloy 152, including cold-worked and heat-affected zone forms of the wrought material.

Brian W. Sheron, Director
Office of Nuclear Regulatory Research
U.S. Nuclear Regulatory Commission

This page is intentionally left blank

Contents

Figures

This page is intentionally left blank

Tables

Executive Summary

This report summarizes work performed from January to December 2005 by Argonne National Laboratory on environmentally assisted cracking (EAC) in light water reactors (LWRs). Topics that have been investigated include: (a) environmental effects on fatigue crack initiation in carbon and low-alloy steels and austenitic stainless steels (SSs), (b) irradiation-assisted stress corrosion cracking (IASCC) of austenitic SSs in boiling water reactors (BWRs), (c) causes and mechanisms of irradiation-assisted cracking of austenitic SS in pressurized water reactors (PWRs), and (d) cracking in Ni alloys and welds.

Fatigue Crack Initiation: The current Section-III design fatigue curves of the American Society of Mechanical Engineers (ASME) Boiler and Pressure Vessel Code are based primarily on strain-controlled fatigue tests of small polished specimens at room temperature in air. Recent fatigue-strain-vs.-life (ε-N) data obtained in the U.S. and Japan demonstrated that LWR environments can have potentially significant effects on the fatigue resistance of materials. The existing fatigue ε-N data for carbon and low-alloy steels and wrought and cast austenitic SSs in air and LWR environments have been reviewed. The effects of various material, loading, and environmental parameters on the fatigue lives of these steels are summarized. The results indicate that the ASME mean curve for low-alloy steels in air is in good agreement with the available experimental data, and the corresponding curve for carbon steels is somewhat conservative. However, the ASME mean curve for SSs in air is not consistent with the experimental data for strain amplitudes <0.5% or stress amplitudes <975 MPa (<141 ksi); the data suggest that the current mean curve for SSs is nonconservative.

The fatigue lives of both carbon and low-alloy steels and austenitic SSs are decreased in LWR environments. The key parameters that influence fatigue life in these environments have been identified. They are temperature, dissolved-oxygen (DO) level in water, strain rate, strain (or stress) amplitude, and, for carbon and low-alloy steels, S content of the steel. Also, the ranges of values of these parameters for which environmental effects are significant have been clearly defined. Statistical models developed earlier to predict fatigue lives of small, smooth specimens of carbon and low-alloy steels and wrought and cast austenitic SSs as a function of material, loading, and environmental parameters have been updated/revised by drawing upon a larger fatigue ε-N database. This report discusses an approach that can be used to incorporate the effects of LWR coolant environments into the ASME Code fatigue evaluations, based on an environmental fatigue correction factor, F_{en}.

A critical review of the ASME Code fatigue adjustment factors of 2 on stress and 20 on life is also presented to assess the possible conservatism in the current choice of these factors. The results suggest that for both carbon and low-alloy steels and austenitic SSs, the current ASME Code requirement of a factor of 20 on cycles to account for the effects of material variability and data scatter, size, surface finish, and loading history in low cycle fatigue contains at least a factor of 1.7 conservatism. To reduce this conservatism, fatigue design curves could be developed from the ANL statistical model by first accounting for mean stress effects and then reducing the mean-stress adjusted curve by a factor of 2 on stress or 12 on cycles, whichever is more conservative.

Irradiation-Assisted Stress Corrosion Cracking in BWRs: The susceptibility of austenitic SSs and their welds to IASCC as a function of the fluence level, water chemistry, material chemistry, and fabrication history is being evaluated. Crack growth rate (CGR) tests and slow strain rate tensile (SSRT) tests are being conducted on various austenitic SSs irradiated at ≈288°C (550°F) in a helium environment in the Halden boiling heavy water reactor. The experimental effort is currently focused on investigating the effects of grain boundary engineering (GBE) on the IASCC behavior of austenitic SSs.

Slow-strain-rate tensile tests have been completed in high-purity 289°C (552°F) water on several austenitic SSs, Alloy 690, and their GBE counterparts that were irradiated to 2.0-2.4 dpa in the Halden phase-II study. In general, all materials showed significant irradiation hardening and loss of ductility, and the uniform elongation for all materials, except GBE Alloy 690, was less than 6%. Uniform elongation for the GBE Alloy 690 was ≈22%. Strain hardening was observed for the high-C Types 304 and 316 SS, whereas strain softening occurred for the low-C Type 304L SS. The results for the uniform elongation suggest that, at the dose level of the present study, GBE does not seem to have a significant effect on the IASCC behavior of austenitic SSs.

The SSRT test results are consistent with the finding from the Halden phase-I study that a minimum C content (≥0.04 wt.%) is required for IASCC resistance. However, the beneficial effect of low S on IASCC resistance observed in the Halden phase-I study could not be confirmed from the present results.

Crack growth rate tests have been conducted in BWR environments on Type 316 SS irradiated to 0.45, 1.35, and 3.0 dpa, and on sensitized Type 304 SS and SS weld heat-affected zone (HAZ) material irradiated to 2.16 dpa. The CGR tests on materials irradiated to 2.16 dpa were followed by a fracture toughness (J-R curve) test in the water environment. The weld HAZ specimens were obtained from a shielded metal arc (SMA) weld prepared from a 30-mm (1.18-in.) plate of Type 304 SS.

In the normal water chemistry (NWC) BWR environment, the cyclic CGRs of SSs irradiated to ≈0.45 dpa are the same as those for nonirradiated materials, whereas the CGRs of SSs irradiated to 0.75-3.0 dpa are significantly higher. The CGRs are decreased by more than an order of magnitude when the DO level is decreased. A superposition model has been used to represent the experimental CGRs. The CGR in the BWR environment is expressed as the superposition of the rate in air (mechanical fatigue) and the rates due to corrosion fatigue and stress corrosion cracking (SCC).

Similarly, in the NWC BWR environment, the SCC growth rates of nonirradiated SSs or materials irradiated to ≈0.45 dpa are either comparable to or slightly lower than the disposition curve in NUREG-0313 for sensitized SSs in water with 8 ppm DO. For austenitic SSs irradiated to 0.75-3.0 dpa, the CGRs are a factor of ≈6 higher than the NUREG-0313 disposition curve. The results also indicate a benefit from a low-DO environment. In general, for the materials and irradiation conditions investigated in the present study, the CGRs decreased more than an order of magnitude when the DO level was decreased from NWC to the hydrogen water chemistry BWR environment. However, a few specimens did not show the benefit of the low-DO environment. It is not clear whether this is due to artifacts of the test (a loss of constraint in the specimen) or to an actual decrease in the effectiveness of reducing the DO level with increasing fluence.

The results of the J-R curve tests in the NWC BWR environment show the same general trend observed for tests in air; however, the fracture toughness J_{Ic} values in water are slightly lower than those in air. A water environment could influence fracture toughness in two ways. An intergranular starter crack compared to a transgranular fatigue crack may decrease the J_{Ic} value for the material, and the effect of the corrosion/oxidation reaction during crack extension may decrease the tearing modulus. Controlled companion tests in air on the same materials are in progress to better determine the effect of the water environment on fracture toughness.

Irradiation-Assisted Stress Corrosion Cracking in PWRs: The IASCC susceptibility and void swelling behavior of austenitic SS core internals in PWR environments are also being evaluated. Both SSRT tests and microstructure examination are being conducted on SS specimens irradiated in the BOR-60 reactor in Russia. Irradiations to ≈5, 10, and 20 dpa have been completed, and the specimens are

available for testing. The SSRT tests will be conducted in the facility currently being used for tests on the Halden specimens. The existing loading fixtures have been modified for the BOR-60 tensile specimens. To avoid bending or twisting of the specimens, a sample holder has been designed for use when installing the specimens in the system. To avoid premature loading of the specimen during heating and pressurization, smaller diameter pull rods have been fabricated and tested at the PWR pressure and temperature conditions.

Small-specimen testing techniques have been reviewed to explore the possibility of extracting fracture toughness information from 3-mm (0.118-in.) disk samples prepared for transmission electron microscopy. Several "punch" tests and instrumented micro-indentation tests have been developed over the years. The basic procedure of punch tests is to drive a small indenter into a flat sample mounted on a die, while load-displacement is recorded for the process. The results indicate that, although the instrumented micro-indentation test is the easiest one to implement because of its commercial availability, the ball punch (bulge) test shows the most promise of providing meaningful information on fracture toughness as well as tensile properties.

The available database on void swelling and density change of austenitic SSs has been critically reviewed. Irradiation conditions, test procedures, and microstructural characteristics were carefully examined, and key factors that are important to determine the relevance of the database to PWR conditions were evaluated. The results indicate that swelling in thin-walled tubes and baffle bolts in a PWR is not a concern. The PWR baffle reentrant corners are the regions where high swelling rates are most likely to occur, especially in locations where the irradiation temperature is high. However, void swelling in a reentrant corner is unlikely to exceed the threshold level of ≈4% beyond which the swelling rate reaches the steady state of 1%/dpa. This estimation is only preliminary, and the maximum temperature of reentrant corners needs to be more accurately quantified.

Cracking of Ni Alloys and Welds: The resistance of Ni alloys to environmentally assisted cracking (EAC) in simulated LWR environments is being evaluated. During the current reporting period, CGR tests were completed in the PWR environment on laboratory-prepared Alloy 182 and field Alloy 82 and Alloy 182 welds from the V. C. Summer nozzle-to-pipe weld. The results are compared with the existing CGR data for Ni alloys and welds to determine the relative susceptibility of these materials to EAC under a variety of loading conditions. The tensile properties, microstructure, and fracture morphology of the nozzle material have also been characterized.

The environmental enhancement of CGRs under cyclic loading was determined relative to the CGRs that would be expected under the same loading conditions for Alloy 600 in air. In general, the CGRs of Alloy 182 in the PWR environment are a factor of ≈5 higher than those of Alloy 600 in air under the same loading conditions. This result is independent of rise time or frequency in the test conditions and indicates that there is minimal environmental enhancement of CGRs of the Alloy 182 weld metal in the PWR environment under this type of loading condition. The dependence of SCC growth rates on the stress intensity factor for Ni-alloy welds can be represented by the Scott model. Material heat-to-heat variations of the CGR are considered and represented in terms of variability in the parameter A in the Scott model. The available data were used to estimate the cumulative distribution of A for the population of Alloy 182 and 82 welds. Values of the parameter A as a function of the percentage of the population bounded and the confidence level are presented. The results suggest that under similar loading and environmental conditions, the mean CGRs for Ni-alloy welds appear to be a factor of ≈2 higher than the mean CGRs for Alloy 600.

The fatigue CGRs of both Alloy 82 weld and Alloy 182 butter from the V. C. Summer weld spool piece are significantly lower than those typically observed for these alloys in air. The SCC growth rates for the V. C. Summer weld and butter alloys are lower than data obtained by others on the same alloys and lower than the proposed disposition curve. These results are not so statistically unlikely that they can be said to prove that there is a difference between field and laboratory welds, but such a difference would be consistent with the observations that operating experience indicates that primary water SCC appears to occur more frequently in wrought Ni-base Alloy 600 components than in the weld metal Alloys 82 and 182 used with Alloy 600, despite the fact that in laboratory tests in PWR coolant environments, the SCC susceptibility of Alloy 182 is usually found to be greater than that of Alloy 600, while that of Alloy 82 is comparable to that of Alloy 600.

Acknowledgments

The authors thank T. M. Galvin, E. Listwan, L. A. Knoblich, R. W. Clark, and J. Tezak for their contributions to the experimental effort. This work is sponsored by the Office of Nuclear Regulatory Research, U.S. Nuclear Regulatory Commission, under Job Code Y6388; Program Manager: W. H. Cullen, Jr.

This page is intentionally left blank

Abbreviations

ABI	Automated Ball Indentation
ANL	Argonne National Laboratory
ASME	American Society of Mechanical Engineers
ASTM	American Society for Testing and Materials
BWR	Boiling Water Reactor
CGR	Crack Growth Rate
CIR	Cooperative IASCC Research
CRDM	Control Rod Drive Mechanism
CSL	Coincident Site Lattice
CT	Compact Tension
CUF	Cumulative Usage Factor
CW	Cold Worked
DO	Dissolved Oxygen
EAC	Environmentally Assisted Cracking
EDS	Energy Dispersive X-ray Microscopy
ECP	Electrochemical Potential
EOL	End of Life
GBE	Grain Boundary Engineered
GBCD	Grain Boundary Character Distribution
GBO	Grain Boundary Optimized
GG	Grand Gulf
GTA	Gas Tungsten Arc
HAZ	Heat Affected Zone
HWC	Hydrogen Water Chemistry
IASCC	Irradiation Assisted Stress Corrosion Cracking
IG	Intergranular
LMFBR	Liquid Metal Fast Breeder Reactor
LVDT	Linear Variable Displacement Transducer
LWR	Light Water Reactor
MA	Mill Annealed
MPA	Materialprufungsanstalt
NRC	Nuclear Regulatory Commission
NRR	Nuclear Reactor Regulation
NWC	Normal Water Chemistry
OIM	Orientation Imaging Microscopy

PVRC	Pressure Vessel Research Council
PWSCC	Primary Water Stress Corrosion Cracking
PWR	Pressurized Water Reactor
RIAR	Research Institute of Atomic Reactors
RIS	Radiation-Induced Segregation
SA	Submerged Arc
SEM	Scanning Electron Microscopy
SCC	Stress Corrosion Cracking
SHE	Standard Hydrogen Electrode
SMA	Shielded Metal Arc
SS	Stainless Steel
SSRT	Slow Strain Rate Tensile
TEM	Transmission Electron Microscopy
TG	Transgranular
UTS	Ultimate Tensile Strength

1 Introduction

Since 1967, the Nuclear Regulatory Commission (NRC) and its predecessor, the Atomic Energy Commission, have conducted research programs that address aging of reactor components. The results of this research have been used to evaluate and establish regulatory guidelines to ensure acceptable levels of reliability for light water reactor (LWR) components. The products of this program (i.e., technical reports, methodologies for evaluating licensee submittals, and other inputs to the regulatory process) have led to the resolution of regulatory issues, as well as the development, validation, and improvement of regulations and regulatory guides. The research on the effects of the environment on component cracking was initiated in response to the determination that environmental effects were critical to several important cracking phenomena in LWR components. A major research program at Argonne National Laboratory (ANL) was initiated in 1979 to address pipe-cracking problems in boiling water reactors (BWRs). Since that time, in response to needs for additional research to support the Office of Nuclear Reactor Regulation (NRR) in assessing cracking problems in aging reactors, the focus of the project has shifted to address other problems in environmental cracking of LWR components. In recent years this activity has been supplemented by NRC participation in the Cooperative Irradiation Assisted Stress Corrosion Cracking Research (CIR) Program, an activity in which groups in several countries contribute money that is used to support research on irradiation-assisted stress corrosion cracking (IASCC) problems of common interest.

This project consists of several tasks with differing objectives, so the objectives are best described on a task-by-task basis:

Task 1: Environmental Effects on Fatigue Crack Initiation.

The objective of this task is to provide information on the effects of LWR coolant environments on fatigue crack initiation in carbon and low-alloy steels and austenitic stainless steels (SSs) and to develop procedures for incorporating environmental effects into the American Society of Mechanical Engineers (ASME) Code fatigue evaluations. The contractor will review and evaluate issues related to environmental effects on fatigue as required by the NRC and will participate in ASME Code committees to incorporate the effects of LWR environments in fatigue life analyses.

Task 2: Evaluation of the Causes and Mechanisms of IASCC in BWRs.

The objectives of this task are to (a) investigate the effects of material chemistry and irradiation level on the susceptibility of SSs to IASCC, (b) develop technical information needed to assure that selected inspection intervals are adequate to assure structural integrity, and (c) verify the effectiveness of industry-proposed mitigative measures. This task will evaluate the susceptibility of austenitic SSs and their welds to IASCC as a function of fluence level, water chemistry, material chemistry, welding process, and fabrication history. It will provide data and technical support required for determination of inspection intervals to help NRC address various issues that arise in license renewal or other licensee submittals. Crack growth rate (CGR) tests and slow strain rate tensile (SSRT) tests have been completed on model SSs irradiated up to 2.0×10^{21} n/cm^2 (E >1 MeV) (≈3.0 dpa) during the Halden phase-I experiment (carried out under NRC JC W6610). Crack growth tests are currently being conducted on submerged arc (SA) and shielded metal arc (SMA) welds of Types 304L and 304 SS irradiated up to $\approx 1.2 \times 10^{21}$ n/cm^2 (≈1.8 dpa) during the Halden phase-II experiment. Also, SSRT tests are being carried out on grain-boundary-optimized (GBO) model SS alloys to study the effect of grain boundary geometry

on IASCC and investigate the prospect of using grain boundary optimization as a mitigative measure. Models and codes developed under CIR and from industry sources will be benchmarked and used in conjunction with this work.

Industry-developed crack growth models will be analyzed and assessed. Also, the effectiveness of mitigative water chemistry measures (e.g., hydrogen water chemistry) will be assessed. Much of this assessment will depend on data provided by industry, available in the literature, and developed as part of this task. However, for CGR models for irradiated materials, it is anticipated that relatively few data will be available because of the expense and difficulty of testing.

Task 3: Evaluation of Causes and Mechanisms of IASCC of Austenitic SS in Pressurized Water Reactors (PWRs).

The current database and mechanistic understanding of IASCC under the PWR conditions of higher temperature and higher fluence are very limited. This task will evaluate (a) the effects of high fluence characteristic of PWR components near or beyond end-of-life on IASCC, (b) neutron irradiation embrittlement (e.g., loss of fracture toughness), and (c) void swelling behavior in austenitic SSs. Tests will be conducted on materials irradiated in the BOR-60 reactor in Russia. The test matrix includes 80 tensile specimens and 222 transmission electron microscopy (TEM) disk specimens. These specimens include (a) cold-worked and solution-annealed heats of Types 304, 304L, 316, 316 LN, and 347 SS, (b) CF-3 and CF-8 cast austenitic SSs, (c) GBO Types 304 and 316 SS and Alloy 690, and (d) several laboratory and commercial heats of austenitic SSs that contain low or high concentrations of S or O. Irradiation to ≈5 and 10 dpa for the tensile specimens and ≈5, 10, and 20 dpa for the TEM disks has been completed; irradiation to 40 dpa is in progress.

Microstructural studies will be conducted to characterize the void swelling behavior of irradiated disk specimens in terms of chemical composition, heat treatment, and microstructure of the material. Ball punch or disk bend tests will be conducted on the disk or coupon specimens to obtain mechanical or fracture properties of the material as a function of neutron damage (dpa). In addition, SSRT tests will be conducted.

Task 4: Cracking of Nickel Alloys and Weldments.

The objective of this task is to provide the NRC with technical data on the implications of cracks in Ni-alloy components and welds for residual life, inspection, and repair. Many vessel penetrations, piping butt welds, and a few reactor vessel internal components and their attachment welds are made of alloys, such as Alloy 600, Alloy X750, and Alloy 182, that are susceptible to primary water stress corrosion cracking (PWSCC). The causes and mechanisms of this cracking and the implications of microstructure, microchemistry, and surface finish for component life are not well understood, and thus lead to greater uncertainty in licensee submissions that address issues such as damage accumulation and inspection intervals. The NRC research program will address these issues and provide data required to support staff assessment of industry CGR models, as well as potential crack detection and mitigation measures. This task will (a) evaluate the effects of material and environmental parameters on the susceptibility of nickel alloys and their welds to PWSCC and (b) develop crack growth data for these alloys in PWR environments to assure that selected inspection intervals are adequate to assess structural integrity.

Task 5: Investigation of Other Modes of Degradation in High-Fluence Materials in PWR Environments.

The objective of this task is to study the potential for other degradation phenomena at high irradiation levels that are not currently being addressed in this program or other industry efforts. The work in this task is focused on developing technical letter reports on various aspects of the degradation of high-dose (>10 dpa) reactor internals in PWR environments, e.g., issues of void swelling, stress corrosion cracking, and the possible synergistic effects of thermal and radiation embrittlement of cast and wrought stainless steels, are being evaluated. The contents of these reports shall be drawn from available literature, the products of past and ongoing industry or DOE programs, and the background sections of the reports published in this series.

This page is intentionally left blank

2 Effect of LWR Coolant Environments on Fatigue Crack Initiation (O. K. Chopra and W. J. Shack)

2.1 Introduction

The ASME Boiler and Pressure Vessel Code Section III, Subsection NB, which contains rules for the design of Class 1 components for nuclear power plants, recognizes fatigue as a possible mode of failure in pressure vessel steels and piping materials. Fatigue has been a major consideration in the design of rotating machinery and aircraft, where the components are subjected to a very large number of cycles (e.g., high-cycle fatigue) and the primary concern is the endurance limit (i.e., the stress that can be applied an infinite number of times without failure). However, cyclic loadings on a reactor pressure boundary component occur because of changes in mechanical and thermal loadings as the system goes from one load set (e.g., pressure, temperature, moment, and force loading) to another. The number of cycles applied during the design life of the component seldom exceeds 10^5 and is typically less than a few thousand (e.g., low-cycle fatigue). The main difference between high- and low-cycle fatigue is that the former involves little or no plastic strain, whereas the latter involves strains in excess of the yield strain. Therefore, design curves for low-cycle fatigue are based on tests in which strain rather than stress is the controlled variable.

The ASME Code fatigue evaluation procedures are described in NB-3200, "Design by Analysis," and NB-3600, "Piping Design." For each stress cycle or load set pair, an individual fatigue usage factor is determined by the ratio of the number of cycles anticipated during the lifetime of the component to the allowable cycles. Figures I-9.1 through I-9.6 of the mandatory Appendix I to Section III of the ASME Boiler and Pressure Vessel Code specify fatigue design curves that define the allowable number of cycles as a function of applied stress amplitude. The cumulative usage factor (CUF) is the sum of the individual usage factors, and ASME Code Section III requires that the CUF at each location must not exceed 1.

The ASME Code fatigue design curves, given in Appendix I of Section III, are based on strain-controlled tests of small polished specimens at room temperature in air. The design curves have been developed from the best-fit curves to the experimental fatigue-strain-vs.-life (ε-N) data, which are expressed in terms of the Langer equation[1] of the form

$$\varepsilon_a = A1(N)^{-n1} + A2, \tag{1}$$

where ε_a is the applied strain amplitude, N is the fatigue life, and A1, A2, and n1 are coefficients of the model. Equation 1 may be written in terms of stress amplitude S_a, which is the product of ε_a and elastic modulus E (i.e., $S_a = E \cdot \varepsilon_a$). In tests performed during the last three decades, fatigue life has been defined in terms of the number of cycles for tensile stress to decrease 25% from its peak or steady-state value. For typical specimens used in these studies, this corresponds to the number of cycles needed to produce an ≈ 3-mm-deep (≈0.118-in.-deep) crack in the test specimen. Thus, the fatigue life of a material is actually being described in terms of three parameters, viz., strain, cycles, and crack depth. The best-fit curve to the existing fatigue ε-N data describes, for given strain amplitude, the number of cycles needed to develop a 3-mm (0.118 in.) crack. The fatigue ε-N data are typically expressed by rewriting Eq. 1 as

$$\ln(N) = A - B \ln(\varepsilon_a - C), \tag{2}$$

where A, B, and C are constants; C represents the fatigue limit of the material; and B is the slope of the log-log plot of ε-N data.

The Code fatigue design curves have been obtained from the best-fit (or mean-data) curves by first adjusting for the effects of mean stress using a modified Goodman relationship,[2] and then decreasing the fatigue life at each point on the adjusted curve by a factor of 2 on strain or 20 on cycles, whichever is more conservative.

The factors of 2 and 20 are not safety margins but rather adjustment factors that should be applied to the small-specimen data to obtain reasonable estimates of the lives of actual reactor components. As described in the Section III criteria document,[2] these factors were intended to account for data scatter (including material variability) and differences in surface condition and size between the test specimens and actual components. In comments about the initial scope and intent of the Section III fatigue design procedures, Cooper[3] states that the factor of 20 on life was regarded as the product of three subfactors:

Scatter of data (minimum to mean)	2.0
Size effect	2.5
Surface finish, atmosphere, etc.	4.0

Although the Section III criteria document[2] states that these factors were intended to cover such effects as environment, Cooper[3] further states that the term "atmosphere" was intended to reflect the effects of an industrial atmosphere in comparison with an air-conditioned laboratory, not the effects of a specific coolant environment. Subsection NB-3121 of Section III of the Code explicitly notes that the data used to develop the fatigue design curves did not include tests in the presence of corrosive environments that might accelerate fatigue failure. Article B-2131 in Appendix B to Section III states that the owner's design specifications should provide information about any reduction to fatigue design curves that is necessitated by environmental conditions.

Existing fatigue ε-N data illustrate potentially significant effects of LWR coolant environments on the fatigue life of carbon and low-alloy steels and austenitic SSs.[4-28] Therefore, the margins in the ASME Code may be less conservative than originally intended.

The fatigue ε-N data are consistent with the much larger database on enhancement of crack growth rates in these materials in simulated LWR environments. The key parameters that influence fatigue life in these environments [e.g., temperature, dissolved-oxygen (DO) level in water, strain rate, strain amplitude, and, for carbon and low-alloy steels, S content of the steel] have been identified. Also, the range of the values of these parameters within which environmental effects are significant has been clearly defined. If these critical loading and environmental conditions exist during reactor operation, then environmental effects will be significant and need to be included in the ASME Code fatigue evaluations. Experience with nuclear power plants worldwide indicates that the critical range of loading and environmental conditions that leads to significant environmental effects on fatigue crack initiation in laboratory experiments is observed during plant operation.[28] A study conducted with SS pipe bend specimens in simulated PWR environments at 240°C (464°F) concluded that the reactor coolant environment can have a significant effect on the fatigue life of austenitic SSs.[29]

Two approaches have been proposed for incorporating the environmental effects into ASME Section III fatigue evaluations for primary pressure boundary components in operating nuclear power plants: (a) develop new fatigue design curves for LWR applications or (b) use an environmental fatigue correction factor, F_{en}, to account for the effects.

In the first approach, following the same procedures used to develop the current fatigue design curves of the ASME Code, environmentally adjusted fatigue design curves are developed from fits to

experimental data obtained in LWR environments. However, because, in LWR environments, the fatigue life of reactor structural materials depends on several loading and environmental parameters, such an approach would require developing several design curves to cover all possible conditions encountered during plant operation.

The second approach, proposed initially by Higuchi and Iida,[11] considers the effects of reactor coolant environments on fatigue life in terms of F_{en}, which is the ratio of fatigue life in air at room temperature to that in water under reactor operating conditions. To incorporate environmental effects into fatigue evaluations, the fatigue usage factor for a specific stress cycle or load set pair, based on the ASME Code design curves, is multiplied by F_{en}.

This section presents an overview of the existing fatigue ε-N data for carbon and low-alloy steels and wrought and cast austenitic SSs in air and LWR environments. The data are evaluated to (a) identify the various material, environmental, and loading parameters that influence fatigue crack initiation and (b) establish the effects of key parameters on the fatigue life of these steels. Statistical models, presented in earlier reports, for estimating fatigue life as a function of material, loading, and environmental conditions, have been updated by using a larger fatigue ε-N database. This section also presents a critical review of the ASME Code fatigue adjustment factors of 2 on stress and 20 on life and assesses the possible conservatism in the current choice of these factors (recommending a factor of 12 on life to remove unnecessary conservatism). Based on the results, new fatigue design curves have been developed for these materials in air. The F_{en} approach for incorporating effects of LWR environments into ASME Section III fatigue evaluations is described.

2.2 Fatigue Strain vs. Life Data

The existing fatigue ε-N data obtained at various research laboratories worldwide have been compiled by the Pressure Vessel Research Council (PVRC), Working Group on ε-N Curve and Data Analysis. The database used in the ANL studies is an updated version of the PVRC database. The sources included in the database are summarized in Table 1.

Table 1. Sources of the fatigue ε-N data on reactor structural materials in air and water environments.

Source	Material	Environment	Reference
General Electric Co.	Carbon steel, Type 304 SS	Air and BWR water	8,9
Japan, including Ishikawajima-Harima Heavy Industries Co., Mitsubishi Heavy Industries Ltd., Hitachi Research Laboratory	Carbon and low-alloy steel, wrought and cast austenitic SS, Alloy 600	Air, BWR, and PWR water	JNUFAD* database, 10-22
Argonne National Laboratory	Carbon and low-alloy steel, wrought and cast austenitic SS	Air, BWR, and PWR water	4-7,23-25
Materials Engineering Associates Inc.	Carbon steel, austenitic SS	Air and PWR water	26
Germany, including MPA	Carbon steel	Air and BWR water	27-28
France, including studies sponsored by Electricite de France	Austenitic SS	Air and PWR water	30-32
Jaske and O'Donnell	Austenitic SS, Ni alloys	Air	33

*Private communication from M. Higuchi, Ishikawajima-Harima Heavy Industries Co. (Japan), to M. Prager of the Pressure Vessel Research Council, 1992. The old database "Fadal" has been revised and renamed "JNUFAD."

Unless otherwise mentioned, smooth cylindrical gauge specimens were tested under strain control with a fully reversed loading (i.e., strain ratio of -1). In nearly all tests, fatigue life is defined as the number of cycles, N_{25}, necessary for tensile stress to drop 25% from its peak or steady-state value. Some of the earlier tests in air were carried out to complete failure of the specimen, and life in some tests is defined as the number of cycles for peak tensile stress to decrease by 1-5%. Also, in fatigue tests that were performed using tube specimens, life was represented by the number of cycles to develop a leak. For the tests where fatigue life was defined by a criterion other than 25% drop in peak tensile stress, fatigue lives were normalized to the 25% drop values before performing the data analysis.[4]

An analysis of the existing fatigue data and the procedures for incorporating environmental effects into the Code fatigue evaluations has been presented in several review articles[34-36] and ANL topical reports.[4,6,7,23-25] The key material, loading, and environmental parameters that influence the fatigue lives of carbon and low-alloy steels and austenitic stainless steels have been identified, and the range of these key parameters where environmental effects are significant has been defined. The significant results have been summarized in earlier reports.[24,25]

2.3 Statistical Models

Statistical models based on the existing fatigue ε-N data have been developed at ANL for estimating the fatigue lives of carbon and low-alloy steels and austenitic SSs in air and LWR environments.[4,23,24] In LWR environments, the effects of key parameters, such as temperature, strain rate, and DO content in water, as well as S content for carbon and low-alloy steels, are included in the correlations. The functional forms for the effects of these parameters were based on the data trends. In the present report, statistical models developed earlier have been updated/revised by drawing upon a larger fatigue ε-N database. Also, a single model is presented for austenitic SSs instead of the separate models presented earlier for Type 304 or 316 SS and Type 316NG.

Predictive models are commonly established through least-square curve fitting of the data to minimize the sum of the square of the residual errors for either fatigue life or strain amplitude. A model based on a least-square fit on life yields accurate values of the constant A in the modified Langer equation but is biased for low strain amplitudes. On the other hand, a least-squares fit on strain yields accurate values of the constant C but does not work well for higher strain amplitudes.

The ANL models were developed by combining the two methods, i.e., by minimizing the sum of the squared Cartesian distances from the data point to the predicted curve. However, the adequacy of predictive models based on a least-square fit of experimental data depends on the sample of data used in the analysis. The models should not only describe the available data well, but also describe the fatigue lives of the much larger number of heats of material that are found in the field. For example, if most of the data were from a heat of material that has poor resistance to fatigue damage or were obtained under loading conditions that show significant environmental effects, the results may be conservative for most of the materials or service conditions of interest. Conversely, if most data were from a heat of material with a high resistance to fatigue damage, the results could be nonconservative for many heats in service.

In the present report, the statistical models were revised by considering the best-fit curves determined from tests on individual heats of materials or loading conditions as samples of the much larger population of heats of materials and service conditions of interest. The fatigue behavior of each of the heats or loading conditions was characterized by the value of the constant A in Eq. 2. The values of A for the various data sets were ordered, and median ranks were used to estimate the cumulative distribution of A for the population.[37,38] The distributions were fit to lognormal curves. No rigorous statistical

evaluation was performed, but the fits seem reasonable and describe the observed variability adequately. Results for carbon and low-alloy steels and austenitic SSs in air and water environments are shown in Fig. 1. The A values that describe the 5th percentile of these distributions give fatigue curves that are expected to bound the fatigue lives of 95% of the heats of the material.

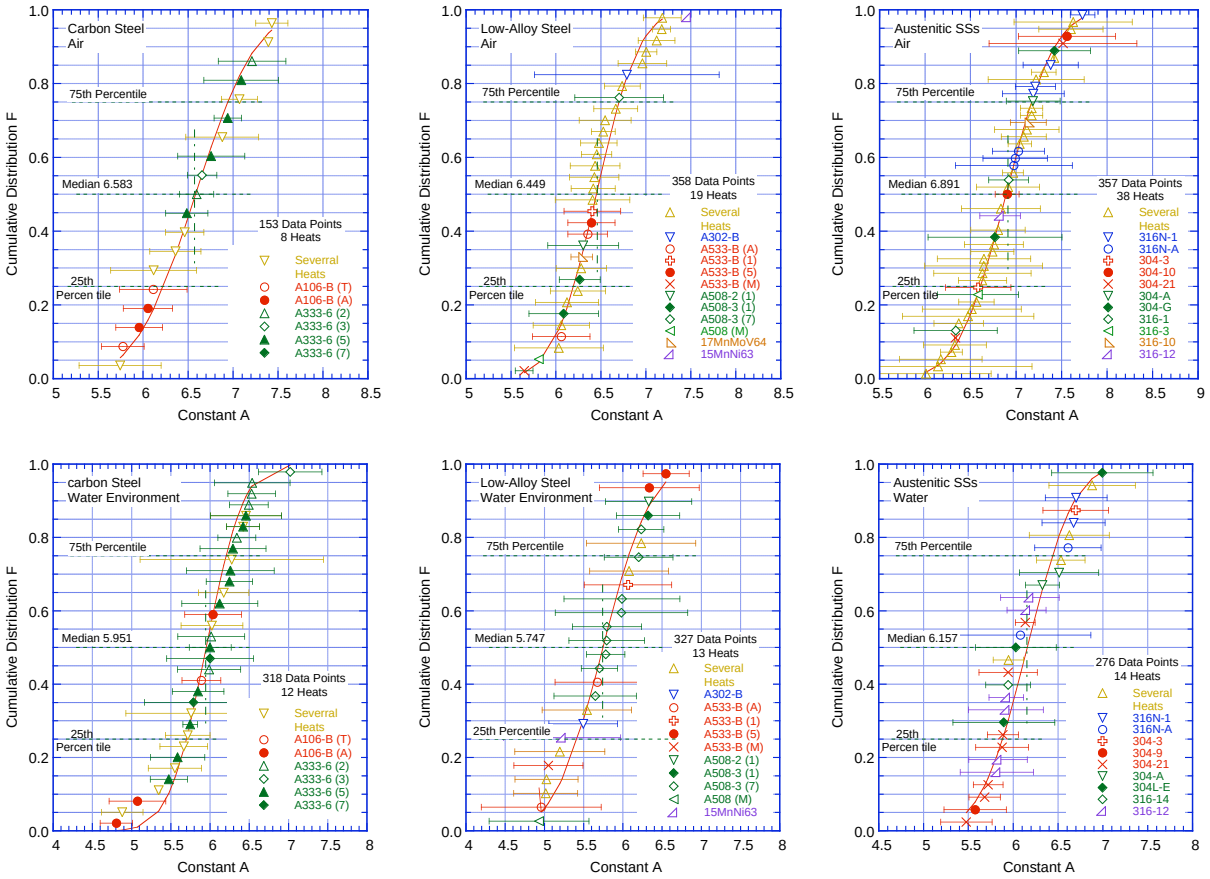

Figure 1. Estimated cumulative distribution of constant A in statistical models for fatigue life with heats of carbon and low-alloy steels and austenitic stainless steels in air and water environments.

The results of these analyses were used to update the statistical models. In room-temperature air, the fatigue life, N, of carbon steels is represented by

$$\ln(N) = 6.583 - 1.975 \ln(\varepsilon_a - 0.113), \quad (3)$$

and that of low-alloy steels, by

$$\ln(N) = 6.449 - 1.808 \ln(\varepsilon_a - 0.151), \quad (4)$$

where ε_a is applied strain amplitude (%). In LWR environments, the fatigue life of carbon steels is represented by

$$\ln(N) = 5.951 - 1.975 \ln(\varepsilon_a - 0.113) + 0.101\, S^* T^* O^* \dot{\varepsilon}^*, \quad (5)$$

and that of low-alloy steels, by

$$\ln(N) = 5.747 - 1.808 \ln(\varepsilon_a - 0.151) + 0.101\, S^* T^* O^* \dot{\varepsilon}^*, \quad (6)$$

where S^*, T^*, O^*, and $\dot{\varepsilon}^*$ are transformed S content, temperature, DO level, and strain rate, respectively, defined as:

$$\begin{aligned} S^* &= 0.015 && (DO > 1.0 \text{ ppm}) \\ S^* &= S && (DO \leq 1.0 \text{ ppm and } S \leq 0.015 \text{ wt.\%}) \\ S^* &= 0.015 && (DO \leq 1.0 \text{ ppm and } S > 0.015 \text{ wt.\%}) \end{aligned} \quad (7)$$

$$\begin{aligned} T^* &= 0 && (T < 150°C) \\ T^* &= T - 150 && (T \leq 150 \leq 350°C) \end{aligned} \quad (8)$$

$$\begin{aligned} O^* &= 0 && (DO \leq 0.04 \text{ ppm}) \\ O^* &= \ln(DO/0.04) && (0.04 \text{ ppm} < DO \leq 0.5 \text{ ppm}) \\ O^* &= \ln(12.5) && (DO > 0.5 \text{ ppm}) \end{aligned} \quad (9)$$

$$\begin{aligned} \dot{\varepsilon}^* &= 0 && (\dot{\varepsilon} > 1\%/s) \\ \dot{\varepsilon}^* &= \ln(\dot{\varepsilon}) && (0.001 \leq \dot{\varepsilon} \leq 1\%/s) \\ \dot{\varepsilon}^* &= \ln(0.001) && (\dot{\varepsilon} < 0.001\%/s). \end{aligned} \quad (10)$$

In air, at temperatures up to 400°C (752°F), the fatigue lives of Types 304, 304L, 316, 316L, and 316NG SS are represented by

$$\ln(N) = 6.891 - 1.920 \ln(\varepsilon_a - 0.112). \quad (11)$$

In LWR environments, fatigue data for austenitic SSs are best represented by the equation:

$$\ln(N) = 6.157 - 1.920 \ln(\varepsilon_a - 0.112) + T'\, \dot{\varepsilon}'\, O', \quad (12)$$

where T', $\dot{\varepsilon}'$, and O' are transformed temperature, strain rate, and DO, respectively, defined as follows:

$$\begin{aligned} T' &= 0 && (T < 150°C) \\ T' &= (T - 150)/175 && (150 \leq T < 325°C) \\ T' &= 1 && (T \geq 325°C) \end{aligned} \quad (13)$$

$$\begin{aligned} \dot{\varepsilon}' &= 0 && (\dot{\varepsilon} > 0.4\%/s) \\ \dot{\varepsilon}' &= \ln(\dot{\varepsilon}/0.4) && (0.0004 \leq \dot{\varepsilon} \leq 0.4\%/s) \\ \dot{\varepsilon}' &= \ln(0.0004/0.4) && (\dot{\varepsilon} < 0.0004\%/s) \end{aligned} \quad (14)$$

$$O' = 0.281 \quad \text{(all DO levels).} \quad (15)$$

These models are recommended for predicted fatigue lives $\leq 10^6$ cycles. Equations 12-15 can be used for cast austenitic SSs such as CF-3, CF-8, and CF-8M. Also, because the influence of DO level on the fatigue life of austenitic SSs may be influenced by the material heat treatment, the ANL statistical model may be somewhat conservative for certain SSs in high-DO water.

2.4 Margins in Code Fatigue Design Curves

Conservatism in the ASME Code fatigue evaluations may arise from (a) the fatigue evaluation procedures and/or (b) the fatigue design curves. The evaluation procedures (e.g., stress analysis rules and cycle counting) have generally been quite conservative. However, the Code permits new and improved approaches to fatigue evaluations (e.g., finite-element analyses, fatigue monitoring, and improved K_e factors) that can significantly decrease the conservatism in these procedures.

The other possible source of conservatism is in the choice of the margins of 2 and 20 that are used to obtain the fatigue design curves from the mean data curve. These margins were intended to cover the effects of variables that can influence fatigue life but were not investigated in the tests that provided the data for the design curves. The variables that must be considered in developing the design curves may be divided in four groups, viz., material variability and data scatter, specimen size and geometry, surface finish, and loading sequence.

2.4.1 Material Variability and Data Scatter

The effects of material variability and data scatter have been evaluated for the various materials (carbon steel, low-alloy steel, and SS) by considering the best-fit curves determined from tests on individual heats of materials or loading conditions as samples; the number of data sets in the sample, as well as the median value of A and the standard deviation for each sample, are listed in Table 2. The 95/95 value of the margin on the median value used to account for material variability and data scatter varies from 2.1 to 2.8 for the samples. These margins are applied to the mean value of life determined from the statistical models and provide 95% confidence that the fatigue life of 95% of the materials and loading conditions of interest will be greater than the resultant value.

Table 2. The median value of A and standard deviation for the various fatigue ε-N data sets used to evaluate material variability and data scatter.

	Air			Water		
	Median A	Standard Deviation	Data Sets	Median A	Standard Deviation	Data Sets
Carbon Steel	6.583	0.477	17	5.951	0.376	33
Low-Alloy Steel	6.449	0.375	32	5.747	0.484	26
Stainless Steel	6.891	0.417	51	6.328	0.462	36

2.4.2 Size and Geometry

The effect of specimen size on the fatigue life was reviewed in earlier reports.[6,24] Various studies conclude that the "size effect" is not a significant parameter in the design curve margins when the fatigue curve is based on data from axial strain control rather than bending tests. No intrinsic size effect has been observed for smooth specimens tested in axial loading or plain bending. However, a size effect does occur in specimens tested in rotating bending; the fatigue endurance limit decreases by ≈25% if the specimen size is increased from 2 to 16 mm (0.08 to 0.63 in.) but does not decrease further with larger sizes. Also, some effect of size has been observed on small-scale-vessel tests conducted at the Ecole Polytechnique in conjunction with the large-size-pressure-vessel tests carried out by the Southwest Research Institute.[39] The fatigue lives determined from tests on the small-scale vessels were 30-50%

lower than those obtained from tests on small, smooth fatigue specimens. However, the difference in fatigue lives in these tests cannot be attributed to specimen size alone; it is due to the effects of both size and surface finish.

During cyclic loading, cracks generally form at surface irregularities either already in existence or produced by slip bands, grain boundaries, second phase particles, etc. In smooth specimens, formation of surface cracks is affected by the specimen size; crack initiation is easier in larger specimens because of the increased number of sites for crack initiation. Specimen size is not likely to influence crack initiation in specimens with rough surfaces because cracks initiate at existing irregularities on the rough surface. As discussed in the next section, surface roughness has a large effect on fatigue life. Consequently, for rough surfaces, the effect of specimen size need not be considered in the margin on life. However, conservatively, a factor of 1.2-1.4 on life may be used to incorporate size effects on fatigue life in the low-cycle regime.

2.4.3 Surface Finish

Fatigue life is sensitive to surface finish; cracks can initiate at surface irregularities that are normal to the stress axis. The height, spacing, shape, and distribution of surface irregularities are important for crack initiation. The effect of surface finish on crack initiation is expressed by

$$N_i(R_q) = 1012\ R_q^{-0.21}, \tag{16}$$

where the root-mean-square value of surface roughness R_q is in μm. The roughness of machined surfaces or natural finishes can range from ≈0.8 to 6.0 μm. The typical surface finish for various machining processes is in the range of 0.2-1.6 μm for cylindrical grinding, 0.4-3.0 μm for surface grinding, 0.8-3.0 μm for finish turning and drilling, and 1.6-4.0 μm for milling. For fabrication processes, it is in the range of 0.8-3.0 μm for extrusion and 1.6-4.0 μm for cold rolling. Thus, from Eq. 16, the fatigue life of components with rough surfaces may be a factor of 2-3.5 lower than that of a smooth specimen.

Limited data indicate that the effects of surface roughness are the same in air and water environments for austenitic SSs but are insignificant in water for carbon and low-alloy steels. Thus, in LWR environments, a factor of 2.0-3.5 on life may also be used to account for surface finish effects for SSs, but the factor may be lower for carbon and low-alloy steels.

2.4.4 Loading Sequence

The effects of variable amplitude loading of smooth specimens were also reviewed in an earlier report.[24] In a variable loading sequence, the presence of a few cycles at high strain amplitude causes the fatigue life at smaller strain amplitude to be significantly lower than that at constant-amplitude loading (i.e., the fatigue limit of the material is lower under variable loading histories).

Under the variable loading conditions encountered during service of power plants, cracks created by growth of microstructurally small cracks at high stresses to depths larger than the transition crack depth can grow to an engineering size even at stress levels below the fatigue limit. Studies on fatigue damage in Type 304 SS under complex loading histories[40] indicate that the loading sequence of decreasing strain levels (i.e., high strain level followed by low strain level) is more damaging than that of increasing strain levels. At low strain levels, the fatigue life of the steel decreased by a factor of 2-4 under a decreasing-strain sequence. In another study, the fatigue limit of medium carbon steels was

lowered even after low-stress high-cycle fatigue; the higher the stress, the greater the decrease in fatigue threshold.[41] Because variable loading histories primarily influence fatigue life at low strain levels, the mean fatigue ε-N curves are lowered to account for damaging cycles that occur below the constant-amplitude fatigue limit of the material.[42] However, conservatively, a factor of 1.2-2.0 on life may be used to incorporate the possible effects of load histories on fatigue life in the low-cycle regime.

2.4.5 Fatigue Design Curve Margins Summarized

The ASME Code fatigue design curves are currently obtained from the mean data curves by first adjusting for the effects of mean stress, and then reducing the life at each point of the adjusted curve by a factor of 2 on strain and 20 on life, whichever is more conservative. The factors on strain are needed primarily to account for the variation in the fatigue limit of the material caused by material variability, component size, surface finish, and load history. Because these variables affect life through their influence on the growth of short cracks (<100 μm), the adjustment on strain to account for such variations is typically not cumulative (i.e., the portion of the life can only be reduced by a finite amount). Thus, it is controlled by the variable that has the largest effect on life. In relating the fatigue lives of laboratory test specimens to those of actual reactor components, the factor of 2 on strain that is currently being used to develop the Code design curves is adequate to account for the uncertainties associated with material variability, component size, surface finish, and load history.

The factors on life are needed to account for variations in fatigue life in the low-cycle regime. Based on the discussions presented above, the effects of various parameters on fatigue life may be summarized as follows:

(a) The results in Table 2 may be used to obtain the margins that need to be applied to the mean value of life to ensure that the resultant value of life would bound a specific percentile of the materials/loading conditions of interest.

(b) For rough surfaces, specimen size is not likely to influence fatigue life, and therefore, the effect of specimen size need not be considered in the margin of 20 on life. However, conservatively, a factor of 1.2-1.4 on life may be used to incorporate size effects on fatigue life.

(c) A factor of 2.0-3.5 on life may be used to account for surface finish effects for carbon and low-alloy steels and austenitic SSs in air and water environments.

(d) Variable loading histories primarily influence fatigue life in the high-cycle regime, and the mean fatigue ε-N curves are lowered by a factor of 2 on strain to account for damaging cycles that occur below the constant-strain fatigue limit of the material. Conservatively, a factor of 1.2-2.0 on life may be used to incorporate the effects of load histories on fatigue life in the low-cycle regime.

The subfactors that are needed to account for the effects of the various material, loading, and environmental parameters on fatigue life are summarized in Table 3. The total adjustment on life varies from 6 to 27. Because the maximum adjustment (27) represents a relatively poor heat of material and assumes the maximum effects of size, surface finish, and loading history, it is likely to be quite conservative. A value of 20 is currently being used to develop the Code design curves from the mean-data curves.

To determine a suitable value for the adjustment factor on life, Monte Carlo simulations were performed using the material variability and data scatter results in Table 2, and the margins needed to

account for the effects of size, surface finish, and loading history listed in Table 3. A lognormal distribution was also assumed for the effects of size, surface finish, and loading history; and the minimum and maximum values of the adjustment factors (e.g., 1.2-1.4 for size) were assumed to represent the 95th and 5th percentile, respectively.

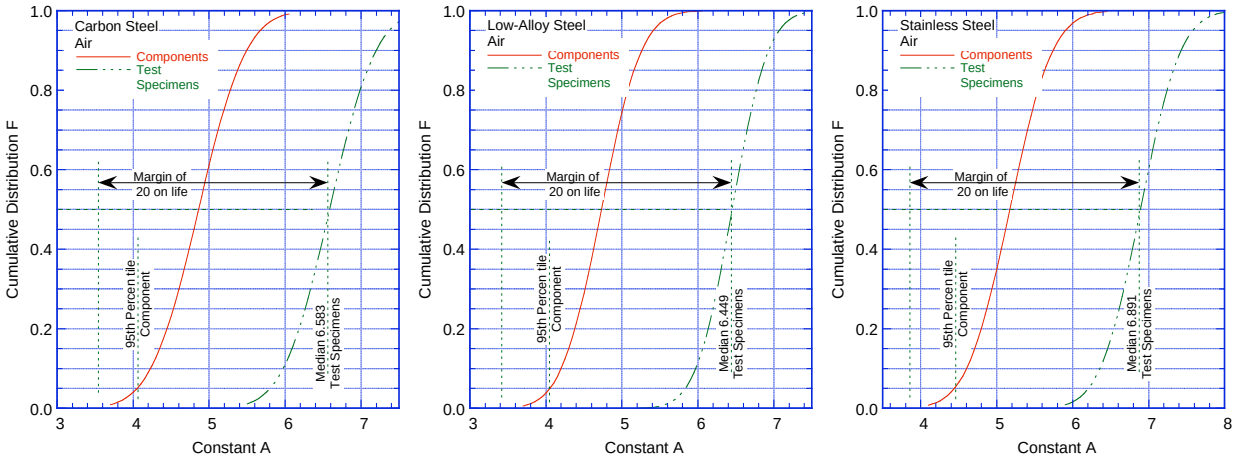

Figure 2. Estimated cumulative distribution of parameter A in statistical models that represent the fatigue life of test specimens and actual components in air.

Table 3. Factors on life applied to mean fatigue ε-N curve to account for the effects of various material, loading, and environmental parameters.

Parameter	Section III Criterion Document	Present Report
Material Variability and Data Scatter (minimum to mean)	2.0	2.1-2.8
Size Effect	2.5	1.2-1.4
Surface Finish, etc.	4.0	2.0-3.5*
Loading History	-	1.2-2.0
Total Adjustment	20	6.0-27.4

*A factor of 2 on life may be used for carbon and low-alloy steels in LWR environments.

The distribution of the values of A in the fatigue curve for test specimens and the adjusted curve that represents the behavior of actual components are shown in Fig. 2. The curves indicate that, to account for the effects of size, surface finish, and loading history, the median value of constant A for the component curve decreased by a factor of 5.6 relative to the specimen curve, and the standard deviation of the heat-to-heat variation in the component curve increased by 6-10%. The margin that has to be applied to the mean data curve for test specimens to obtain the component curve that would bound 95% of the population is 11.0-12.6 (average 11.8); the values are given in Table 4 for the three steels. The choice of bounding the 95th percentile of the population for a design curve is somewhat arbitrary. It is done with the understanding that the design curve controls fatigue initiation, not failure. The choice also recognizes that conservatisms are implied in the choice of log normal distributions, which have an infinite tail, and in the identification of what in many cases are bounding values of the effects as 95th percentile values.

These results suggest that for all materials, the current ASME Code requirements of a factor of 20 on cycles to account for the effects of material variability and data scatter, as well as specimen size,

surface finish, and loading history, contain at least a factor of 1.7 conservatism (i.e., 20/11.8 ≈ 1.7). Thus, a value of 12 on life may be used to develop fatigue design curves from the mean data curve.

Table 4. Margin applied to the mean values of fatigue life to bound 95% of the population.

Material	Margins
Carbon Steels	12.6
Low-Alloy Steels	11.0
Austenitic Stainless Steels	11.6

2.5 Fatigue Design Curves

The current ASME Code mean curve for low-alloy steels is consistent with the existing fatigue ε-N data, whereas that for carbon steels is conservative for fatigue lives $\geq 5 \times 10^5$ cycles. For SSs, the current Code mean curve is nonconservative with respect to the existing fatigue ε-N data. Fatigue design curves that are consistent with the existing data may be obtained from Eqs. 3, 4, and 11, by following the same procedure that was used to develop the current fatigue design curve.

However, as discussed above, the current Code requirement of a factor of 20 on cycles, to account for the effects of material variability and data scatter, specimen size, surface finish, and loading history, is conservative by a factor of ≈1.7. Thus, to reduce this conservatism, fatigue design curves may be developed from the ANL models by first correcting the best-fit curves for mean stress effects and then lowering the adjusted curves by a factor of 2 on stress and 12 on cycles, whichever is more conservative.

2.6 Environmental Fatigue Correction Factor

The effects of LWR coolant environments on the fatigue life of reactor materials may be expressed in terms of F_{en}, which is defined as the ratio of life in air at room temperature, N_{RTair}, to that in water at the service temperature, N_{water}. Values of F_{en} can be obtained from the statistical model, where

$$\ln(F_{en}) = \ln(N_{RTair}) - \ln(N_{water}). \quad (17)$$

The environmental fatigue correction factor for carbon steels is given by

$$F_{en} = \exp(0.632 - 0.101\, S^*\, T^*\, O^*\, \dot{\varepsilon}^*), \quad (18)$$

and for low-alloy steels, by

$$F_{en} = \exp(0.702 - 0.101\, S^*\, T^*\, O^*\, \dot{\varepsilon}^*), \quad (19)$$

where S^*, T^*, $\dot{\varepsilon}^*$, and O^* are defined in Eqs. 7-10. The fatigue life correction factor for austenitic SSs is given by

$$F_{en} = \exp(0.734 - T'\, \dot{\varepsilon}'\, O'), \quad (20)$$

where the constants T', $\dot{\varepsilon}'$, and O' are defined in Eqs. 13-15.

Note that although environmental effects are independent of strain amplitude, they occur only at strain amplitudes above a threshold value (i.e., $F_{en} = 1$ at strain amplitudes below the threshold value). The threshold strain amplitude is 0.07% [145 MPa (21.0 ksi) stress amplitude] for carbon and low-alloy steels and 0.11% [195 MPa (28.3 ksi) stress amplitude] for austenitic SSs.

To incorporate environmental effects into the Section III fatigue evaluation, the fatigue usage factor based on the fatigue design curve in air is multiplied by F_{en}. The usage factors in air are obtained from the Code fatigue design curves provided they are consistent, or conservative, with respect to the existing fatigue ε-N data.

Because environmental effects on fatigue life depend on parameters such as strain rate, temperature, DO in water, and, for carbon and low-alloy steels, S content, values for these parameters are needed to calculate F_{en} for each stress cycle or load set pair. The following guidance may be used to determine these parameters:

(1) An average strain rate for the transient always yields a conservative estimate of F_{en}. The saturation strain rate of 0.001%/s for carbon and low-alloy steels or 0.0004%/s for austenitic SSs can be used to obtain a conservative value.

(2) When the results of detailed transient analyses are available, an average temperature (i.e., average of the maximum and minimum temperatures for the transients) may be used to calculate F_{en}. The maximum temperature can be used to obtain a conservative value.

(3) For carbon and low-alloy steels, the DO content associated with a stress cycle is the highest level in the transient, and for austenitic stainless steels, it is the lowest level.

(4) The sulfur content in terms of weight percent can be obtained from the certified material test report. If the S content is unknown, then its value shall be assumed as the maximum value specified in the procurement specification.

3 Irradiation-Assisted Stress Corrosion Cracking of Austenitic Stainless Steel in BWRs

The objectives of this task are to (a) investigate the effects of material chemistry and irradiation level on the susceptibility of SSs to IASCC, (b) develop technical information needed to assure that selected inspection intervals are adequate to assure structural integrity, and (c) verify the effectiveness of industry-proposed mitigative measures. Crack growth and SSRT tests are being conducted on model SSs, irradiated at ≈288°C (≈550°F) in a helium environment in the Halden boiling heavy water reactor, to investigate the effects of material chemistry and irradiation level on the susceptibility of SSs to IASCC. Slow strain rate tensile tests are also being carried out on grain boundary engineered (GBE) model SS alloys to study the effect of grain boundary geometry on IASCC and investigate the prospect of using GBE as a mitigative measure. Crack growth tests are being conducted on irradiated specimens of SA and SMA welds of Types 304 and 304L SS to establish the effects of fluence level, material chemistry, and welding process on IASCC. Models and codes developed under CIR and from industry sources will be benchmarked and used in conjunction with this work.

3.1 Irradiation-Assisted Stress Corrosion Cracking of Austenitic Stainless Steels from Halden Phase-II Irradiations (Y. Chen, W. K. Soppet, and O. K. Chopra)

3.1.1 Introduction

As nuclear power plants age and exposure to neutron irradiation increases, failures of reactor core internal components have increased. Examples of such failures include cracking of the core shroud, jet pump assembly, top guide, and core plate in BWRs[43-49] and baffle former bolts in PWRs.[50] When exposed to neutron irradiation for extended periods, various nonsensitized austenitic SSs and also Ni alloys become susceptible to intergranular (IG) failure, a form of degradation commonly referred to as irradiation-assisted stress corrosion cracking. In recent years, to address issues related to plant aging and license renewal, IASCC studies have attracted increasing attention.

Neutron irradiation plays a key role in IASCC of LWR internal components. A characteristic rise in IASCC susceptibility is observed above a "threshold" neutron fluence of ≈5 x 10^{20} n/cm^2 (E >1 MeV)* (≈0.75 dpa) in BWR environments,[51] and at fluences approximately one order of magnitude higher in PWRs.[52] Irradiation-induced microstructural (e.g., radiation defects) and microchemistry (e.g., radiation-induced segregation) changes in the material combined with changes in water chemistry (e.g., radiolysis) contribute to the increased susceptibility of IG cracking.[53,54]

Early mechanistic studies of IASCC focused mainly on the depletion of Cr at grain boundaries and its influence on grain boundary oxidation.[55-57] Radiation-induced segregation (RIS) was considered as the main reason for the sharp Cr depletion at grain boundaries. It is generally believed that the absence of protective oxide layers stimulates the cracking behavior along grain boundaries in IASCC. More recently, the role of impurity elements such as Si, P, and S on IASCC susceptibility has also been investigated.[54,58] Although redistribution of impurities around grain boundaries due to RIS is evident, no clear correlations have yet been found between the original concentration of impurities in the bulk material and IASCC susceptibility. The Halden phase-I study is such an effort to investigate the IASCC susceptibility in various austenitic SSs as a function of alloy composition.[59-61] The result of the Halden phase-I study indicates that the S content plays a key role in low-C SSs but is less critical in the high-C

* All references to fluence levels are calculated for E ≥1 MeV.

SSs. [61,62] Recent studies on IASCC have associated radiation hardening and localized deformation with the cracking behavior. It has been suggested that localized plastic deformation contributes to the rupture of the oxide film near the grain boundary and, therefore, is a critical factor for IASCC susceptibility.[63]

Based on the mechanistic understanding on the IASCC progress, various engineering methods to mitigate the effect of IASCC on LWR core internal components have been proposed. Because of the strong dependence of IASCC susceptibility on the corrosion potential between -100 and 0 V (SHE),[58] the most effective way to mitigate IASCC is perhaps by controlling the electrochemical corrosion potential. Meanwhile, because of the predominately intergranular nature of IASCC, considerable attention has also been paid on the role of grain boundaries. It is generally believed that coincident site lattice (CSL) grain boundaries with low Σ numbers* (<29) are more resistant to IG cracking.[64-66] Grain boundary engineering technology, a thermomechanical treatment that systematically modifies grain boundary distribution and increases the population of low Σ CSL grain boundaries, is considered a promising approach to improve the resistance of the steels to IASCC.

In the Halden phase-II study, the effects of grain boundary engineering on IASCC behavior are being investigated. SSRT tests are being conducted in simulated BWR water at 289°C (552°F) on several austenitic SSs, Alloy 690, and their GBE counterparts that were irradiated to the same dose level in the Halden reactor. The IASCC susceptibility of the materials is determined by fractographic analyses. In addition to the study of GBE effects, the Halden phase-II test matrix also provides opportunities to investigate the effects of O content and Ti doping on the IASCC behavior of these steels.

3.1.2 Halden Phase-II Irradiation

The Halden phase-II irradiation experiment, a dry irradiation conducted in helium capsules, was carried out between August 2001 and October 2004 in the Halden boiling heavy water reactor in Norway. A total of 32 SSRT specimens and 28 compact tension (CT) specimens were irradiated in the Halden phase-II experiment. The SSRT specimens were flat, dog-bone tensile specimens, as shown in Fig. 3. All 32 SSRT specimens were packed in two irradiation capsules and loaded in the Halden reactor core position 1-00. All SSRT specimens along with the 28 CT specimens were discharged from the reactor in December 2004 and transferred to ANL in March 2005. The chemical compositions of Halden phase-II SSRT specimens are given in Table 5.

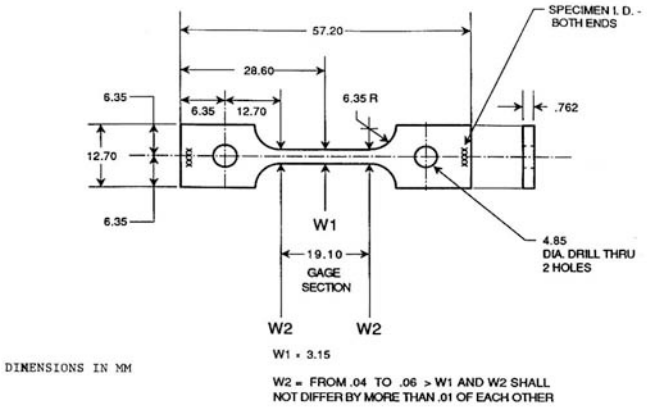

Figure 3.
Halden SSRT test specimen geometry.

* Σ is the reciprocal of the density of coincident sites. For example, Σ of 17 means that one in every 17 sites in one grain coincides with a site from the neighboring grain, and the density of coincident sites is 1/17.

Table 5. Chemical composition of Halden phase-II SSRT specimens.

Heat ID	Composition (wt%)								
	Ni	Si	P	S	Mn	C	N	Cr	Others
GB304	8.19	0.41	0.029	0.006	1.73	0.054	0.052	18.28	Mo 0.23, Co 0.10, Cu 0.31
333	8.45	0.68	0.027	0.019	1.38	0.04	0.068	18.54	Mo 0.37
304L	8.33	0.45	0.028	0.007	1.74	0.023	0.09	18.35	Mo 0.37, Co 0.13, Cu 0.35
GB304L	8.33	0.45	0.028	0.007	1.74	0.02	0.09	18.35	Mo 0.37, Cu 0.35
327	9.54	0.01	0.001	0.002	1.12	0.006	<0.001	19.71	Mo 0.02, O 0.008
945	9.03	0.03	<0.005	0.005	1.11	0.005	0.003	19.21	Mo <0.005, O 0.047
L15	8	1.82	0.01	0.013	1.07	0.02	0.085	17.8	O 0.011
GB316	11.16	0.35	0.029	0.025	1.59	0.041	0.05	16.34	Mo 2.07, Cu 0.37, Co 0.09
623	12.2	0.7	0.007	0.002	0.97	0.019	0.103	17.23	Cu 0.21, Mo 2.38
625	12.3	0.72	0.007	0.002	0.92	0.012	0.064	17.25	Ti 0.027, Cu 0.21, Mo 2.39
690	61.49	0.05	-	0.001	0.15	0.03	-	29.24	Fe 9.02, Co 0.007, Cu 0.01
GB690	59.4	0.42	0.026	0.003	0.42	0.01	-	29.1	Fe 10.26, Al 0.22, Ti 0.29
151	23.49	0.06	0.006	0.005	1.39	0.004	0.001	24.02	Mo 0.002

The target neutron fluence for all Halden phase-II SSRT specimens was 1.2 x 10^{21} n/cm^2 (1.8 dpa). The actual neutron dose was monitored by an Al/1% Co wire (for thermal neutrons) and by Fe and Ni wires (for fast neutrons) attached to the external surface of the irradiation capsules. During irradiation, specimen temperature was also monitored by two sets of melting alloy temperature monitors in each irradiation capsule. The post-irradiation analyses of dosimeter wires and temperature monitors provided the actual conditions of Halden phase-II irradiation. The results are summarized in Table 6.

Table 6. Irradiation conditions for Halden phase-II SSRT specimens.

Heat ID	Material	Available Specimens	Neutron fluence E >1 MeV (x10^{21} n/cm^2)	Damage Dose (dpa)	Irr. Temp. (°C)
GB304	Grain-boundary- optimized 304 SS	3	1.31	1.96	296-305
333	ABB 304 SS	3	1.63	2.44	290-296
304L	304L SS, commercial heat	2	1.31	1.96	296-305
GB304L	Grain-boundary-optimized 304L SS	3	1.31	1.96	296-305
327	High-purity 304L SS, low O	3	1.63	2.44	290-296
945	High-purity 304L SS, high O	3	1.63	2.44	290-296
L15	304 SS, laboratory heat	1	1.63	2.44	290-296
GB316	Grain-boundary-optimized 316 SS	3	1.31	1.96	296-305
623	316LN (high N, low C)	2	1.63	2.44	290-296
625	316LN, Ti-doped	2	1.63	2.44	290-296
690	Alloy 690	2	1.31	1.96	296-305
GB690	Grain-boundary-optimized Alloy 690	3	1.31	1.96	296-305
151	Fe-Cr-Ni model alloy, Fe-20Cr-24Ni	2	1.63	2.44	290-296

3.1.3 SSRT Tests and Results

3.1.3.1 SSRT Tests

The SSRT tests were carried out in a test facility that is located in hot cell #1 of the Irradiated Materials Laboratory at Argonne. The SSRT testing is equipped with a worm gear actuator, a set of gear

reducers, and a variable speed motor with speed control. The high-purity high-DO water environment was provided by the recirculating loop shown schematically in Fig. 4. The water loop consists of a storage tank, 0.2 micron filter, high-pressure pump, regenerative heat exchanger, autoclave preheater, test autoclave, electrochemical potential (ECP) cell preheater, ECP cell, air-cooled heat exchanger, Mity Mite^{TM} back-pressure regulator, two ion-exchange cartridges, another 0.2 micron filter, and return line to the storage tank. The high-pressure portion of the system extends from the high-pressure pump (item 10) to the back-pressure regulator (item 27). Overpressurization of the loop is prevented by a rupture disk (set at 2300 psig) installed upstream of the high-pressure pump.

1. Cover gas supply tank
2. Two stage high-pressure regulator
3. Low-pressure regulator
4. Compound vacuum & pressure gauge
5. Feed water storage tank
6. Sparger
7. Tank water sample port
8. Solenoid valve
9. 0.2 micro filter
10. High-pressure pump
11. Rupture disk
12. Check valve
13. High-pressure gauge
14. Heat exchanger
15. Autoclave preheater
16. Tube autoclave
17. Thermocouple well
18. ECP cell preheater
19. Preheater thermocouple
20. ECP cell
21. ECP cell thermocouple
22. SS electrode
23. Standard reference electrode
24. Platinum electrode
25. Heat exchanger
26. Cooling fan
27. Back-pressure regulator
28. Outlet vent port
29. Loop water sampling port (not in use)

29B. Loop water sampling port (new)

30. Ion exchange bed
31. 2nd ion exchange bed
32. 0.2 micron filter
33. Feed water fill port
34. Recirculating pump
35. Check valve
36. Pressure relief valve to tank
37. Check valve
38. Bypass pressure relief valve

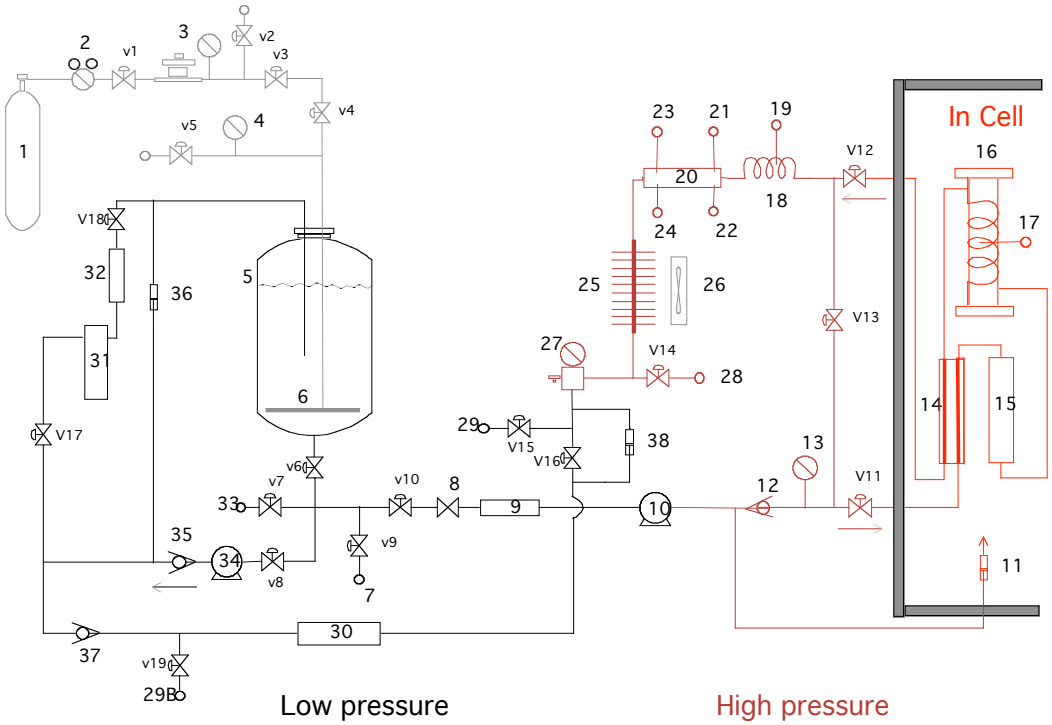

Figure 4. Schematic diagram of the recirculating water system.

SSRT tests on Halden phase-II specimens were conducted at 289°C in high-purity water containing ≈8 ppm DO. The system pressure was maintained at ≈9.31 MPa (≈1350 psig) during the tests. The conductivity and pH of water at room temperature were maintained at 0.06-0.10 µS/cm and 6.4-7.2, respectively. The flow rate of the system was 15-30 ml/min, and water samples were taken periodically from ports 7 and 29B to monitor the resistivity, pH, and DO level in the effluent. The ECP of a Pt electrode and a SS sample located downstream from the autoclave was monitored continuously during the test. The strain rate during the SSRT tests was held constant at 3.31 x 10^{-7} s^{-1}.

Because of the relatively small thickness [≈0.76 mm (0.03 in.)] and cross section area [≈2.4 mm^2 (0.0037 $in.^2$)] of the Halden SSRT specimens, precautions were taken during specimen installation and pressurization of the autoclave to prevent premature straining. During installation, each specimen was first loaded on the sample grip and then inserted into a tube autoclave. The assembled autoclave was then hung on the test frame without lower pin in place to maintain a stress-free condition on the specimen until the desired temperature and pressure were achieved. The specimen was then soaked in the test environment [289°C, ≈9.3 MPa (552°F, ≈1350 psi)] for about 24 hours under a tensile stress less than ≈140 MPa (≈20.3 ksi) prior to the SSRT test.

3.1.3.2 SSRT Results

Eight SSRT tests have been completed to date: seven on irradiated and one on nonirradiated specimens. The characteristic tensile properties were determined by the scheme illustrated in Fig. 5. The results from a selection of the irradiated specimens are shown in Fig. 6. If a well-defined upper yield point was present in the engineering stress vs. engineering strain curve, the stress at the upper yield point was selected as the yield stress. Otherwise, the stress at the 0.2% plastic stain was defined as the yield stress. If no strain hardening was observed in an SSRT test, the ultimate tensile strength (UTS) was considered the same as the yield stress. Accordingly, the uniform elongation in this case was taken at the point where the post-yield engineering stress vs. engineering strain curve starts to deviate from linearity. See Fig. 5. If a small amount of strain hardening remained in an SSRT test, the nominal definition of uniform elongation (i.e., the plastic strain at UTS) was used. The characteristic tensile properties determined using this scheme for all Halden SSRT tests are summarized in Table 7.

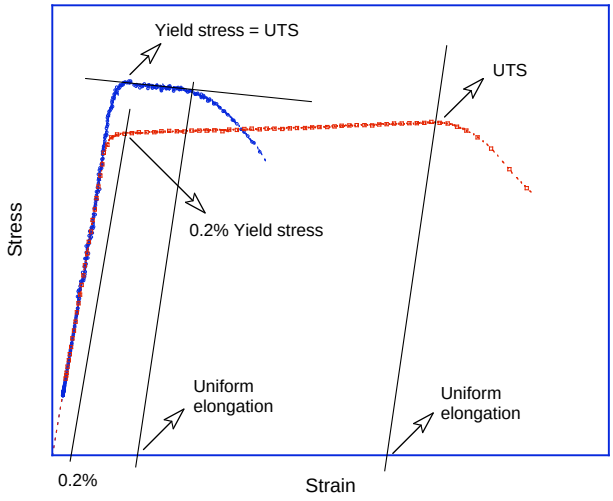

Figure 5.
Schematic for determining SSRT properties.

The results to date from SSRT tests on Halden phase-II specimens show a significant amount of irradiation hardening. Irradiation embrittlement was also evident among these materials except for GBE Alloy 690, in which more than 22% uniform elongation remained after irradiation. For austenitic SSs, a minimum amount of strain hardening remained in Types 304 and 316 SS, while no strain hardening was observed in Type 304L SS. For Alloy 690, a considerable amount of strain hardening occurred in the GBE alloy, whereas only limited strain hardening was observed in the alloy without the GBE treatment. Dynamic strain aging was observed in both Alloy 690 materials, with and without GBE.

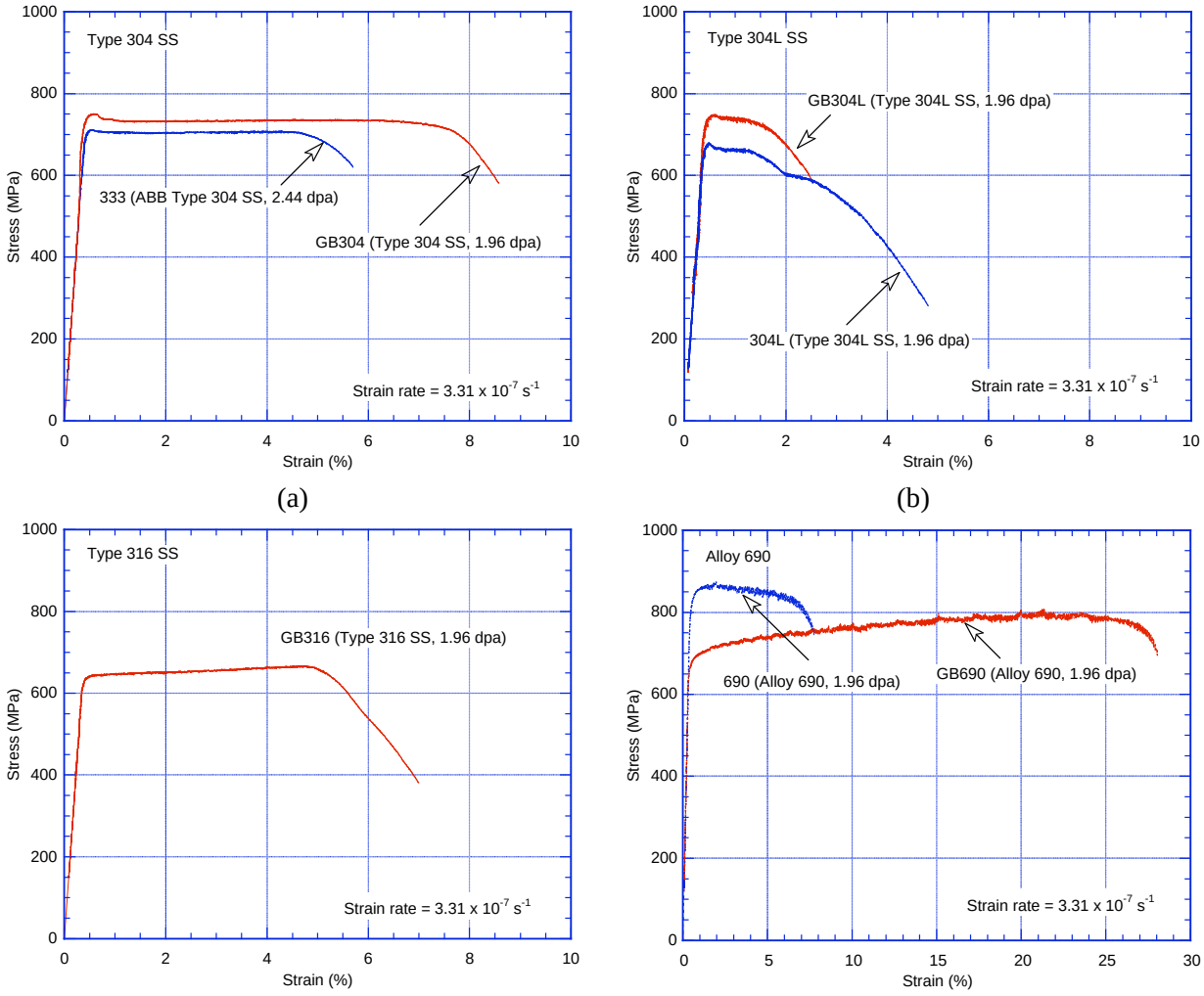

Figure 6. Stress-strain curves of Halden phase-II SSRT specimens tested in simulated BWR water environment: (a) Type 304 SS, (b) Type 304L SS, (c) Type 316 SS, and (d) Alloy 690.

Table 7. Results of Halden phase-II SSRT tests.

Material	Heat ID	Dose (dpa)	Yield Stress (MPa)	UTS (MPa)	Fracture Stress (MPa)	Uniform Elong. (%)	Total Elong. (%)
304 SSs	333	2.44	711	711	621	4.06	5.34
	GB304	1.96	750	750	581	5.80	8.22
304L SSs	304L	1.96	677	677	282	2.18	4.65
	GB304L	1.96	747	747	581	1.11	2.22
	GB304L*	-	231 (0.2%)	532	454	32.20	36.10
316 SS	GB316	1.96	640 (0.2%)	664	378	4.44	6.80
690 alloys	690	1.96	837 (0.2%)	868	743	5.94	7.29
	GB690	1.96	677 (0.2%)	801	704	22.80	27.60

* Nonirradiated specimen tested in BWR-like water environment.

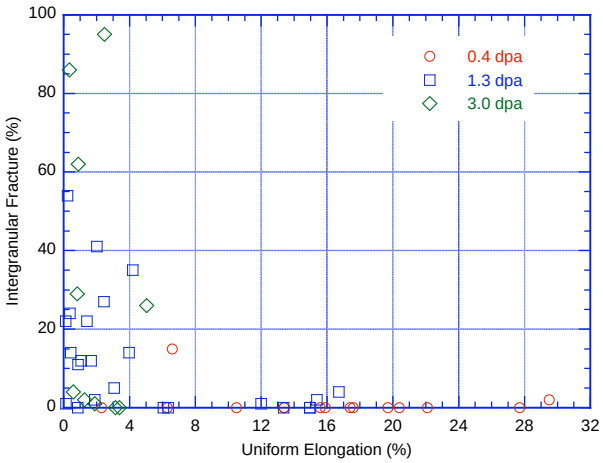

Figure 7.
Uniform elongation and IG fraction for Halden phase-I SSRT tests.

Influence of Grain-boundary Engineering

Grain-boundary engineering is a thermomechanical treatment that increases the population of low Σ number CSL boundaries. One objective of the Halden phase-II study is to illustrate the effect of GBE treatment on the IASCC susceptibility. By the end of this reporting period fracture surface analyses had not been performed; therefore, the IASCC susceptibility of the materials has not been assessed yet. However, the SSRT test result from the Halden phase-I study showed a general trend of a decrease in IG fraction with an increase in uniform elongation, as shown in Fig. 7. The IG fracture behavior is obviously more complicated for the region of uniform elongation less than 7~8%, and a large scatter does exist in the IG fraction measurement for this region. Above 7~8% uniform elongation, the intergranular fraction is significantly less. On the basis of these results, it is safe to conclude that the IASCC behavior will be dissimilar if the uniform elongation is drastically different in SSs.

The current Halden phase-II results show that the GBE treatment does not alter, significantly, the SSRT behavior of austenitic SSs in high-DO water at 289°C (552°F). While the GBE process slightly increased the uniform elongation of Type 304 SS, it had the opposite effect on Type 304L SS. For the present dose range, because the differences in uniform elongations are very small, the effect of the GBE process on the IASCC behavior of irradiated Types 304 and 304L SS in the BWR environment cannot be determined accurately. For Alloy 690, uniform elongation was considerably larger for the material with the GBE treatment than without it (e.g., 22.80% vs. 5.94%). Despite the possible difference in materials, the tensile results indicate a strong difference in deformation behavior of Alloy 690 with and without GBE treatment.

Influence of Alloy Elements

The Halden phase-I study indicated that a minimum C content and a low S content in austenitic SSs are helpful in impeding IASCC. The influence of other impurity elements (such as Si and P) on IASCC behavior is not clear.[61] On the basis of the Halden phase-II SSRT test results, the influences of S, C, Si, and P content on uniform elongation of Types 304, 304L, and 316 SS are plotted in Fig. 8. The open symbols in the plots represent low-C austenitic SSs; these materials typically have relatively small uniform elongation. These results are consistent with the finding that a minimum C content (≥0.04 wt.%) is required for IASCC resistance. However, a beneficial effect of low S on IASCC resistance as concluded in Halden phase-I study is not obvious from the uniform elongations of the Halden phase-II SSRT tests. Similarly, no clear dependence was observed between the Si and P content and uniform elongations in the Halden phase-II SSRT tests.

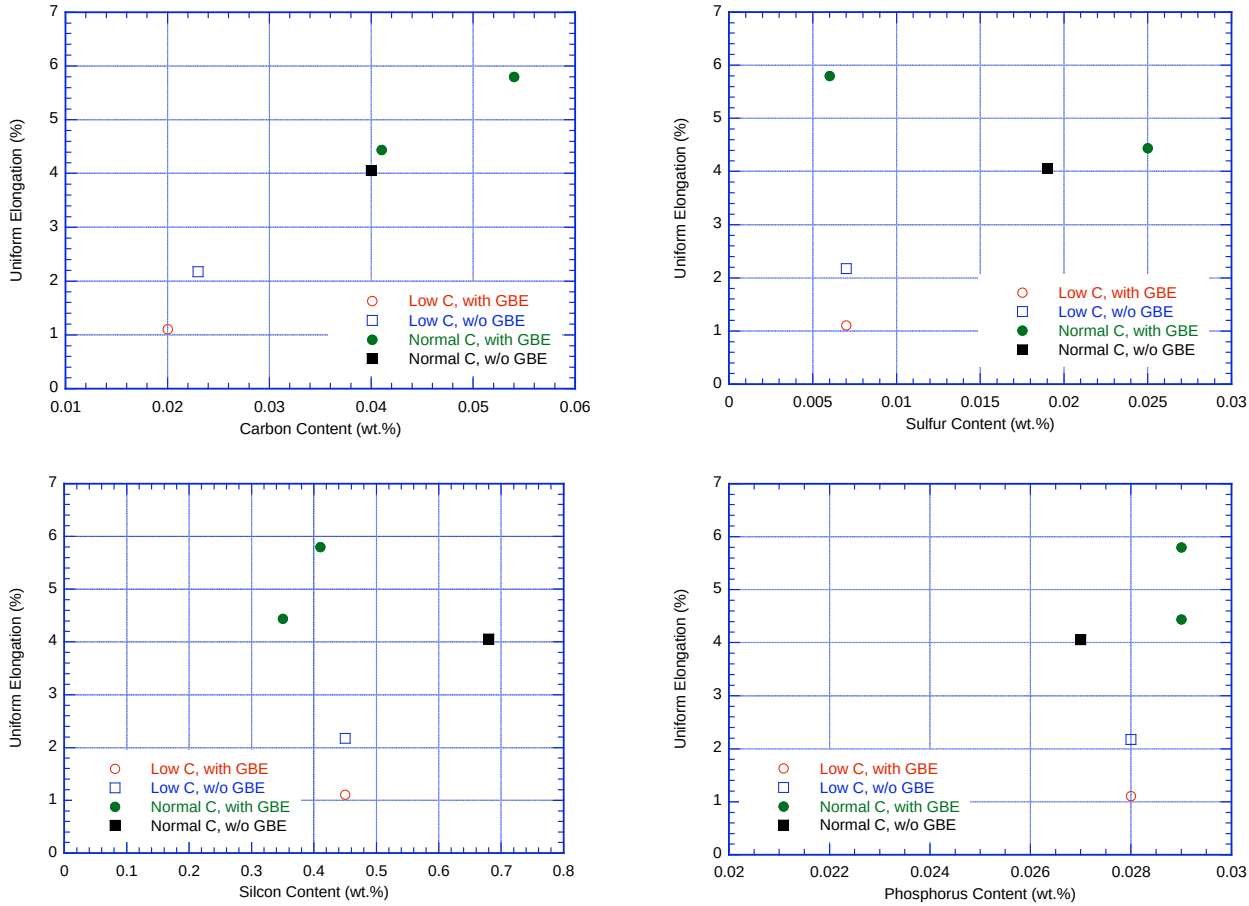

Figure 8. Influence of alloy elements on uniform elongation in Halden phase-II SSRT tests in high-DO water at 289°C.

3.2 Crack Growth Rate Test of Austenitic Stainless Steels Irradiated in the Halden Reactor (E. E. Gruber and O. K. Chopra)

3.2.1 Introduction

Austenitic SSs are used extensively as structural alloys in reactor pressure vessel internal components because of their high strength, ductility, and fracture toughness. However, exposure to neutron irradiation for extended periods changes the microstructure and degrades the fracture properties of these steels. Irradiation leads to a significant increase in yield strength and reduction in ductility and fracture resistance of austenitic SSs.[67-70] Radiation can exacerbate the corrosion fatigue and stress corrosion cracking (SCC) of SSs[58,67,71] by affecting the material microchemistry (e.g., radiation-induced segregation); material microstructure (e.g., radiation hardening); and water chemistry (e.g., radiolysis).

The factors that influence SCC susceptibility of materials include neutron fluence, cold work, corrosion potential, water purity, temperature, and loading. The effects of neutron fluence on the IASCC of austenitic SSs have been investigated for BWR control blade sheaths[72-74] and BWR-irradiated material;[58,75-77] the extent of intergranular SCC was found to increase with fluence. Although a

threshold fluence level of 5 x 10^{20} n/cm^2 (E >1 MeV)* (≈0.75 dpa) has been proposed for austenitic SSs in BWR environments based on early experimental results, intergranular cracking has been seen at fluences as low as ≈2 x 10^{20} n/cm^2 (≈0.3 dpa).[58,78] The results also show the beneficial effect of reducing the corrosion potential of the environment,[71,79] which suggests that the threshold fluence for IASCC is higher under low potential conditions such as BWR hydrogen water chemistry (HWC) or PWR primary water chemistry. However, low corrosion potential does not provide immunity to IASCC if the fluence is high enough; for example, intergranular SCC has been observed in cold-worked, irradiated SS baffle bolts in PWRs.

A program is being conducted at ANL on irradiated SSs to support the regulatory request to better understand the safety issues attendant to the cracking of BWR internals such as core shrouds. The susceptibility of austenitic SSs to IASCC is being evaluated as a function of the fluence level, material composition, and water chemistry. Experimental data are being obtained on fracture toughness, corrosion fatigue, and SCC of Types 304 and 316 SS base metal and weld heat-affected zone (HAZ). These materials are irradiated to fluence levels up to 2.0 x 10^{21} n/cm^2 (3.0 dpa) at 288-300°C (550-572°F). The fracture toughness J-R curve tests are conducted in air at 289°C (552°F), and the CGR tests are conducted in normal water chemistry (NWC) and HWC BWR environments at ≈289°C (≈552°F).

In earlier studies, fracture toughness tests were completed in an air environment on Types 304 and 316L SS (Heats C19 and C16, respectively) irradiated up to 2.0 x 10^{21} n/cm^2 (E > 1 MeV) (3.0 dpa).[80] Neutron irradiation at ≈288°C (≈550°F) to 3.0 dpa decreased the fracture toughness of both the steels. For Heat C19 of Type 304 SS irradiated to 0.3, 0.9, and 2.0 x 10^{21} n/cm^2 (0.45, 1.35, and 3.0 dpa), the J_{Ic} values were 507, 313, and 188 kJ/m^2, respectively. The fracture toughness data fell within the scatter band for the results obtained from fast reactor irradiations at higher temperatures. To determine the possible effects of test environment and crack morphology on the fracture toughness of these steels, fracture toughness tests are being conducted in NWC BWR environments at ≈289°C (≈552°F).

In earlier studies, CGR tests were completed on Types 304L and 316L SS (Heats C3 and C16, respectively) irradiated to a fluence level of 0.3, 0.9, and 2.0 x 10^{21} n/cm^2 (0.45, 1.35, and 3.0 dpa) and on Types 304 and 304L weld HAZ irradiated to 0.5 x 10^{21} n/cm^2 (0.75 dpa). The results indicated significant enhancement of CGRs for irradiated steels in the NWC BWR environment.[80,81] The CGRs of Type 304L SS irradiated to 1.35 and 3.0 dpa and Type 316L SS irradiated to 3.0 dpa were comparable and a factor of ≈5 higher than the disposition curve proposed in NUREG-0313[82] for sensitized austenitic SSs in water with 8 ppm DO. Type 304L SS irradiated to 0.45 dpa showed very little increase of CGRs in high-DO water. Also, for these irradiation levels, the CGRs under constant load were below the NUREG-0313 disposition curve for sensitized SSs.

The results for weld HAZ materials indicated that irradiation to 5 x 10^{20} n/cm^2 (E > 1 MeV) (≈0.75 dpa) has little or no effect on the cyclic CGRs of these materials. However, SCC growth rates for SS weld HAZ materials irradiated to 0.75 dpa were a factor of 2-5 higher than the NUREG-0313 disposition curve for sensitized SSs in high-DO water. Limited data suggest that the SCC growth rates of nonirradiated weld HAZ materials may also be higher than the NUREG-0313 disposition curve.

The results also indicated that in low-DO BWR environments, the CGRs of the irradiated steels decrease by an order of magnitude in some tests (e.g., Type 304L SS irradiated to 1.35 dpa and Type 316L SS irradiated to 3.0 dpa). As noted previously, the benefit of low DO appears to decrease with increasing fluence. The beneficial effect of decreased DO was not observed in a test on Type 304L SS

* All references to fluence levels are calculated for E ≥1 MeV.

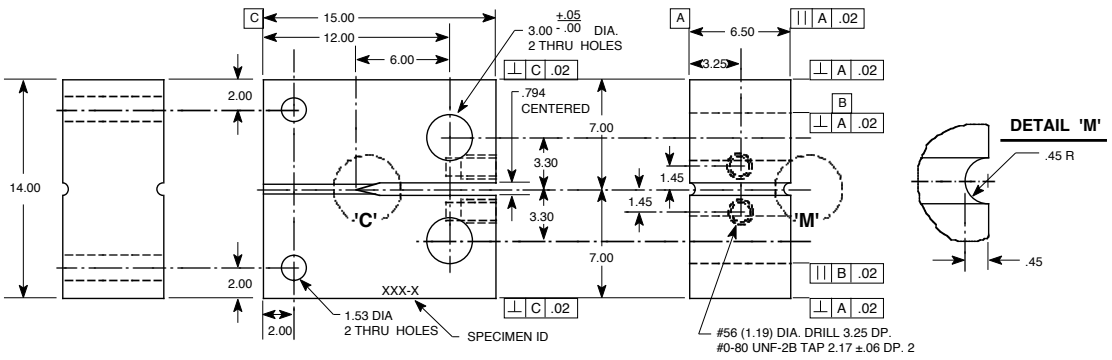

Figure 9. Configuration of compact-tension specimen for this study (dimensions in mm).

Heat C3 irradiated to 3.0 dpa, although this different behavior may be associated with the loss of constraint in the specimen due to the high applied load.

This annual report presents experimental CGR data in BWR environments at 289°C (552°F) for Type 316 SS irradiated to 0.3, 0.9, and 2.0 x 10^{21} n/cm^2 (0.45, 1.35, and 3.0 dpa) at 288±2°C (550±4°F), and CGR and fracture toughness data on sensitized Type 304 SS and SS weld HAZ material irradiated to 1.44 x 10^{21} n/cm^2 (2.16 dpa) at 297±7°C (567±12°F). The weld HAZ specimens were obtained from an SMA weld prepared from a 30-mm (1.18-in.) plate of Type 304 SS (Heat 10285).

3.2.2 Experimental

The CGR tests were performed at ≈289°C (≈552°F) on 1/4-T CT specimens in simulated BWR environments in accordance with American Society for Testing and Materials (ASTM) E-647, "Standard Test Method for Measurement of Fatigue Crack Growth Rates," and ASTM E-1681, "Standard Test Method for Determining a Threshold Stress Intensity Factor for Environment-Assisted Cracking of Metallic Materials under Constant Load." The tests were conducted in the load-control mode using a triangular or sawtooth waveform with load ratio R of 0.2-0.7. The configuration of the specimens is shown in Fig. 9. Crack extensions were determined by DC potential measurements. The compositions of the SSs that are being investigated in the ANL study are presented in Table 8.

The SMA weld was prepared in the laboratory by welding two 70 x 178 mm (2.75 x 7.0 in.) pieces of 30-mm (1.18-in.) thick plate. The specimens were machined from 9.5-mm (0.37 in.) thick slices of the weld; before machining, some slices were thermally treated for 24 h at 500°C (932°F) to simulate long-term aging during service. For all specimens, the machined notch was located in the HAZ of the weld. Each slice was etched, and the specimen orientation and notch location relative to the weld were clearly identified. Details regarding the facility and procedure for conducting the tests and material characterization were presented earlier.[83]

The tensile yield and ultimate stress for the various SSs irradiated to the three fluence levels and in the nonirradiated condition[84] are given in Table 9. The tensile properties of Heat 10285, in the mill-annealed condition and after sensitization at 600°C (1112°F) for 10.5 h, are listed in Table 10.[81] For the irradiated materials, the yield stress was estimated from the correlation developed by Odette and Lucas[85]; the increase in yield stress (MPa) is expressed in terms of the fluence (dpa) by the relationship

$$\Delta\sigma_y = 670\,[1 - \exp(-\mathrm{dpa}/2)]^{0.5}. \qquad (21)$$

Table 8. Composition (wt.%) of Types 304 and 316 stainless steel investigated.

Steel Type	Heat ID	Analysis	Ni	Si	P	S	Mn	C	N	Cr	Mo	O
304L	C3	Vendor	8.91	0.46	0.019	0.004	1.81	0.016	0.083	18.55	-	-
		ANL	9.10	0.45	0.020	0.003	1.86	0.024	0.074	18.93	0.12	0.014
304	C19	Vendor	8.08	0.45	0.031	0.003	0.99	0.060	0.070	18.21	-	-
		ANL	8.13	0.51	0.028	0.008	1.00	0.060	0.068	18.05	0.09	0.020
316L	C16	Vendor	12.90	0.38	0.014	0.002	1.66	0.020	0.011	16.92	-	-
		ANL	12.32	0.42	0.026	0.003	1.65	0.029	0.011	16.91	2.18	0.016
316	C21	Vendor	10.24	0.51	0.034	0.001	1.19	0.060	0.020	16.28	2.08	-
		ANL	10.45	0.61	0.035	0.002	1.23	0.060	0.016	16.27	2.10	0.014
304	10285	Vendor	8.40	0.51	0.032	0.006	1.64	0.058	-	18.25	0.41	-
		ANL	8.45	0.60	0.015	0.007	1.90	0.070	0.084	18.56	0.51	0.013

The ultimate stresses for the irradiated steels were estimated from the data in Ref. 84. The tensile yield and ultimate stresses for the irradiated SSs are also given in Table 10. The tensile properties of the sensitized material were used to determine the K/size criterion for nonirradiated and irradiated HAZ specimens, both in the as-welded and as-welded plus thermally-treated conditions.

Table 9. Tensile properties[a] at 289°C of austenitic stainless steels from Halden phase-I irradiations.

			Fluence (E >1 MeV)					
	Nonirradiated		0.3×10^{21} n/cm^2 (0.45 dpa)		0.9×10^{21} n/cm^2 (1.35 dpa)		2.0×10^{21} n/cm^2 (3.00 dpa)	
Steel Type (Heat)	Yield (MPa)	Ultimate (MPa)	Yield (MPa)	Ultimate (MPa)	Yield (MPa)	Ultimate (MPa)	Yield (MPa)	Ultimate (MPa)
304L SS (C3)	(154)	(433)	338	491	632	668	796	826
304 SS (C19)	178	501	554	682	750	769	787	801
316L SS (C16)	(189)	(483)	370	527	562	618	766	803
316 SS (C21)	277	455	480	620	643	716	893	924

[a]Estimated values within parentheses.

Table 10. Tensile properties[a] at 289°C of austenitic stainless steels from Halden phase-II irradiations.

		Fluence (E >1 MeV)					
		Nonirradiated		0.5×10^{21} n/cm^2 (0.75 dpa)		1.44×10^{21} n/cm^2 (2.16 dpa)	
Steel Type (Heat)	Material Condition	Yield (MPa)	Ultimate (MPa)	Yield (MPa)	Ultimate (MPa)	Yield (MPa)	Ultimate (MPa)
304 SS (10285)	Mill annealed	196	508	-	-		
	MA + 10.5 h at 600°C	156	501	(531)	(680)	(670)	(780)

[a]Estimated values within parentheses.

The CT specimens were fatigue precracked in the test environment at load ratio R = 0.2 or 0.3, triangular waveform, frequency of 1 or 2 Hz, and maximum stress intensity factor (K_{max}) of 13-16 MPa m$^{1/2}$ (11.8-14.5 ksi in.$^{1/2}$). After ≈0.15-mm (0.06 in.) extension, R was increased incrementally to 0.5 or 0.7, and the loading waveform was changed to a slow/fast sawtooth with rise times of 30-1000 s and unload time of 12 s. Finally, the specimen was tested under constant load (with or without periodic partial unloading) to ensure crack extension under SCC conditions. During individual test periods, K_{max} was maintained approximately constant by periodic load shedding (less than 2% decrease in load at any given time); K_{max} at the end of the test period is reported in the results.

Under cyclic loading, the CGR (m/s) can be expressed as the superposition of the rate in air (i.e., mechanical fatigue) and the rates due to corrosion fatigue and SCC, given as

$$\dot{a}_{env} = \dot{a}_{air} + \dot{a}_{cf} + \dot{a}_{SCC}\,. \quad (22)$$

The CGR in air, $\dot{a}_{air}$ (m/s), was determined from the correlations developed by James and Jones[86]; it is expressed as

$$\dot{a}_{air} = C_{SS}\, S(R)\, \Delta K^{3.3}/T_R\,, \quad (23)$$

where R is the load ratio (K_{min}/K_{max}), ΔK is K_{max} - K_{min} in MPa $m^{1/2}$, T_R is the rise time (s) of the loading waveform, and the function S(R) is expressed in terms of the load ratio R as follows:

$$\begin{aligned} S(R) &= 1.0 && R < 0 \\ S(R) &= 1.0 + 1.8R && 0 < R < 0.79 \\ S(R) &= -43.35 + 57.97R && 0.79 < R < 1.0. \end{aligned} \quad (24)$$

The function C_{SS} is given by a third-order polynomial of temperature T (°C), expressed as

$$C_{SS} = 1.9142 \times 10^{-12} + 6.7911 \times 10^{-15}\, T - 1.6638 \times 10^{-17}\, T^2 + 3.9616 \times 10^{-20}\, T^3. \quad (25)$$

The effects of the environment on fatigue crack growth of nonirradiated austenitic SSs have been investigated by Shack and Kassner.[87] In the absence of any significant contribution of SCC to growth rate, the CGRs in water with ≈0.3 ppm DO are best represented by the expression

$$\dot{a}_{env} = \dot{a}_{air} + 4.5 \times 10^{-5}\, (\dot{a}_{air})^{0.5}, \quad (26)$$

and in water with ≈8 ppm DO by the expression,

$$\dot{a}_{env} = \dot{a}_{air} + 1.5 \times 10^{-4}\, (\dot{a}_{air})^{0.5}. \quad (27)$$

The CGR (m/s) under SCC conditions is represented by the correlation given in the U.S. NRC report NUREG-0313, Rev. 2:[82]

$$\dot{a}_{SCC} = A\, (K)^{2.161}, \quad (28)$$

where K is the stress intensity factor (MPa $m^{1/2}$), and the magnitude of constant A depends on the water chemistry and composition and structure of the steel. A value of 2.1×10^{-13} for constant A has been proposed in NUREG-0313 for sensitized SS in water chemistries with 8 ppm DO. The magnitude of constant A will be smaller in low-DO environments, such as HWC BWR or PWR environments.

All tests were started in high-purity water that contained 250-500 ppb DO (i.e., NWC BWR environment). The electrochemical potential (ECP) of a Pt electrode and a SS sample located at the exit of the autoclave was monitored continuously during the test; the water DO level and conductivity were determined periodically. After data were obtained for high-DO water, the DO level was decreased to <30 ppb by sparging the feedwater with a gas mixture of N_2 + 5% H_2. Because of the very low water flow rates, it took several days for the environmental conditions to stabilize for the in-cell tests. In general, the changes in ECP of the SS sample were slower than in the ECP of the Pt electrode.

In the present study crack length "a" was calculated from the following correlation, which was developed from the best fit of the experimental data for normalized crack length and normalized DC potential:

$$\frac{a}{W} = \left[0.28887 \left(\frac{U}{U_0} - 0.5 \right) \right]^{-0.34775}, \tag{29}$$

where W is the specimen width, and U and U_0 are the current and initial potentials, respectively. Equation 29 is comparable to the ASTM E 1737 correlation for a CT specimen with current inputs at the W/4 position and DC potential lead connections at the W/3 position. Also, the stress intensity factor range ΔK was calculated from the correlations for a CT specimen as follows:

$$\Delta K = \frac{\Delta P}{\left(B B_N W \right)^{1/2}} \frac{\left(2 + \frac{a}{W} \right)}{\left(1 - \frac{a}{W} \right)^{3/2}} f\left(\frac{a}{W} \right), \tag{30}$$

$$\Delta P = \Delta P_{max} - \Delta P_{min} \qquad \text{for } R > 0, \tag{31}$$

$$f\left(\frac{a}{W} \right) = 0.886 + 4.64 \left(\frac{a}{W} \right) - 13.32 \left(\frac{a}{W} \right)^2 + 14.72 \left(\frac{a}{W} \right)^3 - 5.60 \left(\frac{a}{W} \right)^4, \tag{32}$$

where P_{max} and P_{min} are the maximum and minimum applied load, respectively; B is the specimen thickness; B_N is the net specimen thickness (or distance between the roots of the side grooves); and W is the specimen width.

In the present test facility, the Bal-seal™ between the pull rod and the autoclave cover plate exerts a frictional load on the pull rod. Typically, the frictional load varied in the range of ±22-44 N (±5-10 lb). However, for the tests being performed on Halden phase-II specimens, the frictional load is in the range of ±111-133 N (±25-30 lb). Therefore, the measured values of P_{max} and P_{min} are first corrected for the frictional load before calculating ΔK for the various test periods. The most significant effect of this correction is on the waveform for the cyclic tests; although the tests were intended to be conducted with either triangular or sawtooth waveforms, the actual loading waveforms for the test specimen are trapezoidal because the load did not change during the initial 40-50% of the loading or unloading cycles.

After the CGR test, the DC potential measuring system was reinitialized to the new crack length, and a J-R test was performed on the specimen at 289°C (552°F) in the high-DO water. The test was conducted at a constant extension rate of ≈0.43 μm/s (0.017 mil/s) in accordance with ASTM specification E-1737 for "J-Integral Characterization of Fracture Toughness." The test was interrupted periodically (by holding the specimen at constant extension) to measure the crack length. For most steels, load relaxation occurs during the hold period, which may influence the DC potential readings. Consequently, before measurement of the DC potential drop, the specimen was held for ≈30 min to allow relaxation.

Specimen extension was monitored and controlled outside the high-temperature zone. The actual displacement of load points was determined by subtracting the extension of the load train from the measured extension. The load train displacement was determined as a function of applied load using a very stiff specimen. The J-integral was calculated from the load-vs.-load-line displacement curves according to the correlations for standard CT specimens in ASTM Specification E 1737.

After the test the final crack size was marked by fatigue cycling in air at room temperature. The specimens were then fractured, and the fracture surface of both halves of the specimen was photographed with a telephoto lens through the hot cell window. The final crack length of each half of the fractured specimen was determined from the optical photograph by the 9/8 averaging technique. Nine measurements were taken across the width of the specimen at equal intervals, the two near-surface measurements were averaged, and the resultant value was averaged with the remaining seven measurements. The crack extensions determined from the DC potential drop method were proportionately scaled to match the final optically measured crack length.

The CGR during each test period was determined from the slope of the corrected crack length vs. time plots; for cyclic loading, only the rise time was used to determine growth rate. The crack extension during each test period was at least 10 times the resolution of the DC potential drop method [typically, 5 μm (≈0.2 mil)]. Thus, crack extensions were at least 50 μm (2 mil); for test periods with very low CGRs (e.g., less than 1×10^{-11} m/s) smaller crack extensions were used to reduce testing time.

The CGR test results were validated in accordance with the specimen size criteria of ASTM E 1681 and E 647. These criteria require that the plastic zone at the tip of a fatigue crack be small relative to the specimen geometry. The ASTM specifications for specimen K/size criteria are intended to ensure applicability and transferability of the cracking behavior of a component or specimen of a given thickness under a specific loading condition to a crack associated with a different geometry, thickness, and loading condition. For constant load tests, ASTM E 1681 requires that

$$B_{eff} \text{ and } (W - a) \geq 2.5 (K/\sigma_{ys})^2, \tag{33}$$

And for cyclic loading ASTM 647 requires that

$$B_{eff} \text{ and } (W - a) \geq (4/\pi) (K/\sigma_{ys})^2, \tag{34}$$

where K is the applied stress intensity factor, σ_{ys} is the yield stress of the material, a is crack length, W is the specimen width, and the specimen effective thickness B_{eff} is defined in terms of the specimen thickness B and net thickness B_N expressed as $(B\ B_N)^{0.5}$. For high strain-hardening materials [ultimate-to-yield stress ratio $(\sigma_{ult}/\sigma_{ys}) \geq 1.3$], both criteria allow the use of the flow stress defined as $\sigma_f = (\sigma_{ult} + \sigma_{ys})/2$ rather than the yield stress.

The K/size criteria were developed for materials that show work hardening and, therefore, may not be applicable for materials irradiated to fluence levels where, on a local level, they do not strain harden. This lack of strain hardening, termed strain softening, is most dramatic when dislocation channeling occurs but may also occur at lower fluences. For moderate to highly irradiated material, an effective yield stress, defined as the average of the nonirradiated and irradiated yield stresses, has been suggested[88]; this discounts the irradiation-induced increase in yield stress by a factor of 2. In the present study, because the ultimate-to-yield stress ratio was generally less than 1.3, the effective yield stress was used to determine the allowed K_{max} for the irradiated specimens. The only exception was Heat C21 irradiated to ≈0.45 dpa; the effective flow stress was used to determine allowed K_{max} for this specimen.

The experimental results from the J-R curve test were analyzed in accordance with ASTM E-1737 to obtain the fracture toughness J-R curve. Although a slope of two times the flow stress is specified for the blunting line in ASTM E-1737, a slope of four times the flow stress is found to better represent the experimental data for high-strain-hardening materials such as austenitic SSs. Thus, in the present study, a slope of $4\sigma_f$ was used to define the offset and exclusion lines. The DC potential data were corrected to account for the effects of plasticity on the measured potential; large crack-tip plasticity can increase measured potentials due to resistivity increases without crack extension. As per ASTM E-1737, the change in potential prior to the attainment of crack initiation was ignored, and the remainder of the potential change was used to establish the J-R curve. The normalized potential varies linearly with load-line displacement until the onset of crack extension. For all data prior to the loss in linearity (Δa_B crack extension), crack extension was expressed as $a_o + \Delta a_B$, where a_o is the initial crack length and crack extension at Δa_B, which is calculated from the blunting line relationship $\Delta a = J/(4\sigma_f)$. For all data after this point, crack length was calculated from Eq. 29, in which U_0 is considered to be the potential at the onset of crack extension in the potential vs. load-line displacement plot (i.e., at Δa_B crack extension). To account for the possible strain softening that may occur in irradiated materials, the effective flow stress was used in the J-R curve data analysis.

3.2.3 Crack Growth Tests on Irradiated Stainless Steels in BWR Environments

Crack growth tests have been completed in BWR environments at 289°C (552°F) on 1/4-T CT specimens of Type 316 SS irradiated to 0.3, 0.9, and 2.0 x 10^{21} n/cm^2 (≈0.45, 1.35, and 3.00 dpa), and CGR and fracture toughness tests have been completed on sensitized Type 304 SS and SMA weld HAZ irradiated to 1.44 x 10^{21} n/cm^2 (≈2.16 dpa). The significant results for the various tests are summarized below.

3.2.3.1 Specimen C21-A of Type 316 SS, Test CGRI-25

The test on Specimen C21-A of Type 316 SS irradiated to 0.45 dpa was started in high-purity water with ≈350 ppb DO and flow rate of ≈20 mL/min. The ECPs of a Pt and SS electrode located downstream from the autoclave were monitored continuously, and the effluent water conductivity and DO level were measured periodically. The system was operated for a few days to stabilize the environmental conditions. The specimen was fatigue precracked at R = 0.35, K_{max} = 15.5 MPa m$^{1/2}$ (14.1 ksi in.$^{1/2}$), triangular waveform, and frequency of 1 Hz. After ≈0.2-mm (≈7.9-mil) crack advance, R was increased incrementally to 0.7, and the waveform was changed to a slow/fast sawtooth with rise times of 30-1000 s. Finally, the specimen was subjected to a constant load with and without periodic partial unloading. At ≈162 h the test was interrupted because of a power bump that tripped the autoclave temperature control unit and the water pump. The stoppage of water flow caused the ECP-cell unit to overheat and damage to the reference electrode. The test was restarted with the ECP cell bypassed; ECP measurements were not obtained for the remainder of the test. There was no chloride intrusion during the interruption, and test conditions prior to the interruption were restored.

After the test the final crack size was marked by fatigue cycling in air at room temperature. The specimen was then fractured, and the fracture surfaces of both halves of the specimen were photographed with a telephoto lens through the hot cell window. A photograph of the fracture surfaces is shown in Fig. 10. The final crack length of each half of the specimen was measured from the photograph by the 9/8 averaging technique. The actual crack length was ≈23% greater than the value determined from the DC potential measurements. The experimental crack extensions were scaled proportionately. The environmental and loading conditions, corrected CGRs, and the allowed K_{max} based on the K/size

criterion are given in Table 11; the changes in crack length and K_{max} with time during the various test periods are plotted in Fig. 11.

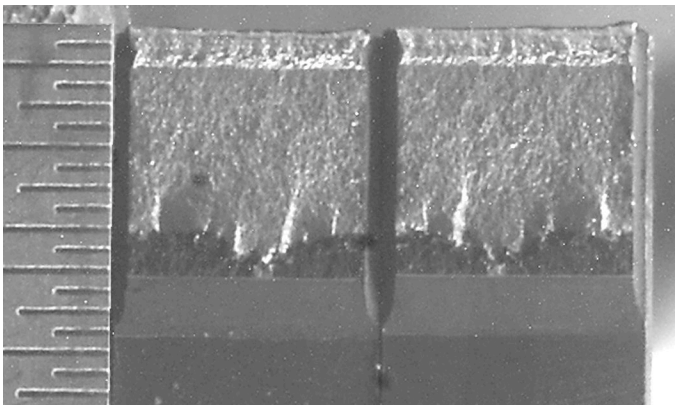

Figure 10.
Photograph of the fracture surfaces of the two halves of Specimen C21-A.

Table 11. Crack growth data for Specimen C21-A[a] of Type 316 SS in BWR water at 289°C.

Test Period	Test Time, h	ECP[b] mV (SHE) Pt	ECP[b] mV (SHE) Steel	O_2 Conc.,[b] ppb	R Load Ratio	Rise Time, s	Return Time, s	Hold Time, s	K_{max}, MPa $m^{1/2}$	ΔK, MPa·$m^{1/2}$	Growth Rate, m/s	Allowed K_{max},[c] MPa $m^{1/2}$	Crack Length,[d] mm
Pre a	95	-	-	350	0.35	0.5	0.5	0	15.5	10.1	1.10E-08	22.2	6.138
Pre b	112	249	103	350	0.34	5	5	0	15.7	10.3	5.69E-09	22.0	6.244
1	157	246	116	350	0.51	30	4	0	16.0	7.9	1.33E-09	21.7	6.410
2	232	e	e	350	0.53	300	12	0	16.1	7.6	3.82E-10	21.5	6.497
3	331	e	e	350	0.69	300	12	0	16.2	5.0	1.10E-10	21.4	6.544
4	474	e	e	350	0.70	1,000	12	0	16.3	4.9	5.84E-11	21.3	6.571
5	570	e	e	350	0.70	12	12	3600	16.5	5.0	1.51E-10	21.2	6.622
6	695	e	e	350	0.70	12	12	3600	21.8	6.5	2.46E-10	21.0	6.748
7	835	e	e	350	1.00	-	-	-	22.7	-	2.56E-10	20.7	6.883

[a]Type 316 SS Heat C21, irradiated to 0.3 x 10^{21} n/cm^2 (0.45 dpa).
[b]Represents values in the effluent. Conductivity and DO were ≈0.07 µS/cm and 500 ppb, respectively, in the feedwater.
[c]Based on effective flow stress, defined as the average of irradiated and nonirradiated flow stresses.
[d]Actual crack extension was 23% greater than the value determined from the DC potential drop measurements.
[e]ECP not measured, the ECP cell was damaged due to a power bump at 162 h. The test was restarted and experimental conditions were restored; there was no chloride intrusion during the interruption.

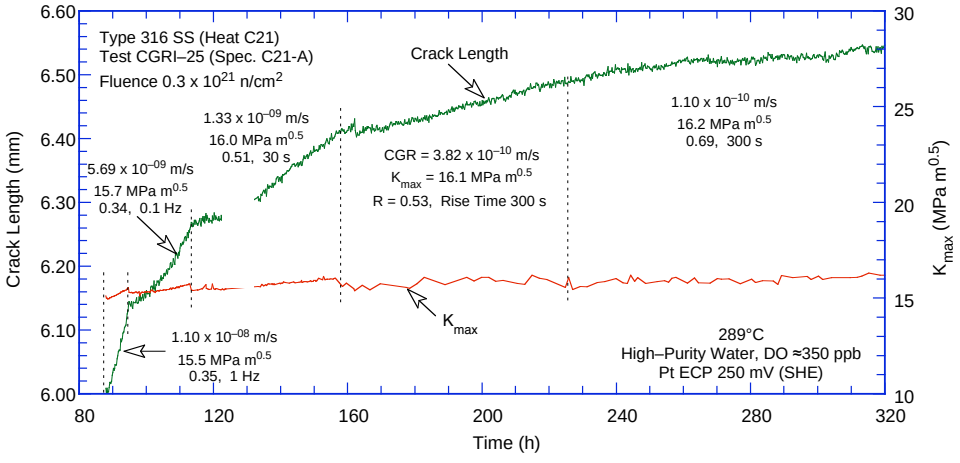

(a)

Figure 11. Crack-length-vs.-time plot for Type 316 SS in BWR water at 288°C during test periods (a) precracking-3, (b) 4-5, and (c) 6-7.

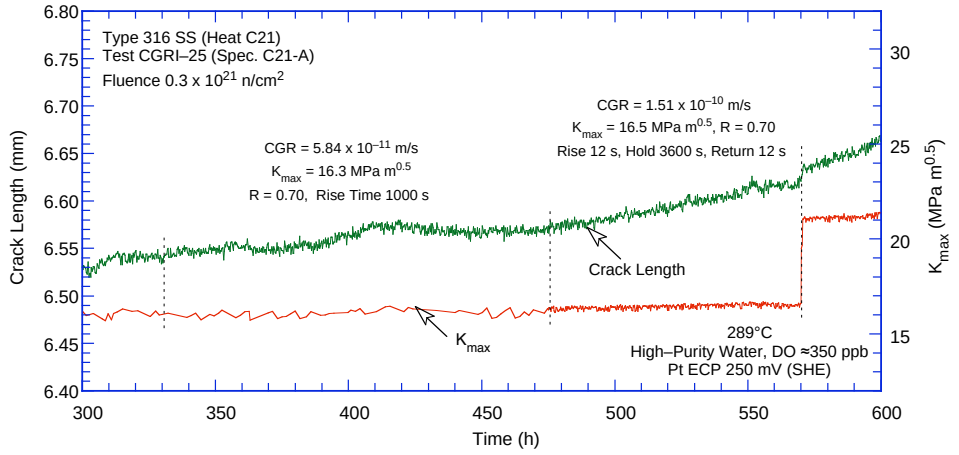

(b)

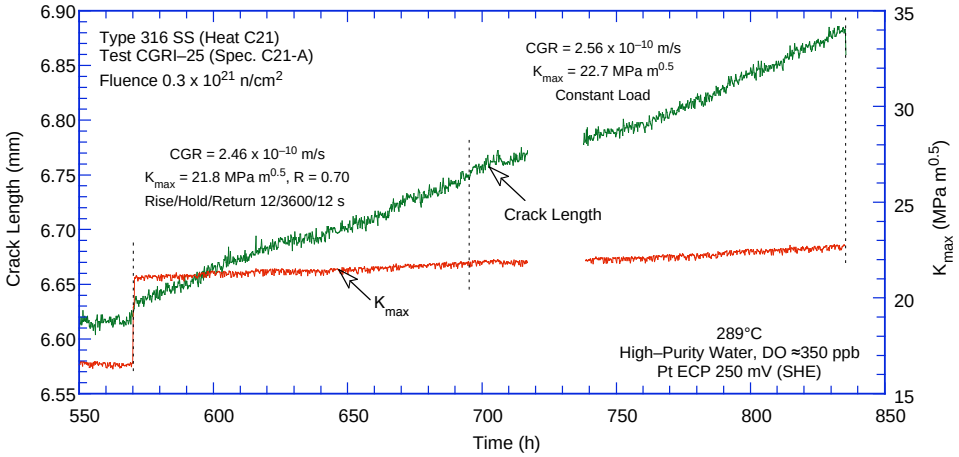

(c)

Figure 11. (Contd.)

3.2.3.2 Specimen C21-B of Type 316 SS, Test CGRI-24

The test on Specimen C21-B of Type 316 SS irradiated to 1.35 dpa was started in high-purity water with ≈350 ppb DO and flow rate of ≈34 mL/min. The ECPs of a Pt and SS electrode located downstream from the autoclave were monitored continuously, and the effluent water conductivity and DO level were measured periodically. The system was operated for a few days to stabilize the environmental conditions. The specimen was precracked at R = 0.33, K_{max} = 15.9 MPa $m^{1/2}$ (14.5 ksi $in.^{1/2}$), triangular waveform, and frequency of 1 Hz. After ≈0.4-mm (15.7-mil) crack advance, R was increased incrementally to 0.7, and the waveform changed to a slow/fast sawtooth with rise times of 300 or 1000 s. The experimental data for the test are given in Table 12; for about 30 h crack length data were lost because of a malfunction in the DC potential drop system.

After ≈245 h the DO level in the feedwater was decreased from ≈350 ppb to <30 ppb by purging the feedwater tank with a mixture of N_2 + 5% H_2. The change in crack length and ECP of Pt and SS electrodes during the transient period is shown in Fig. 12. The ECP of the Pt electrode decreased to below -450 mV (SHE) within 3-4 h, while the ECP of the SS electrode took nearly 20 h to decrease to -200 mV (SHE), although it eventually decreased to <400 mV. Crack growth rates dropped significantly in the low DO environment. The test was terminated after 557 h. The changes in crack length and K_{max} with time during the various test periods are shown in Fig. 13.

Table 12. Test conditions and results for Specimen C21-B[a] of Type 316 SS in BWR water at 289°C.

Test Period	Test Time, h	ECP[b] mV (SHE) Pt	ECP[b] mV (SHE) Steel	O_2 Conc.,[b] ppb	R Load Ratio	Rise Time, s	Return Time, s	Hold Time, s	K_{max}, MPa $m^{1/2}$	ΔK, MPa $m^{1/2}$	Growth Rate, m/s	Allowed K_{max},[c] MPa $m^{1/2}$	Crack Length,[d] mm
Pre	7	-	-	350	0.33	0.5	0.5	0	15.9	10.6	2.63E-08	21.94	6.312
1[e]	24	268	151	350	0.52	300	12	0	-	-	-	-	-
2a[e]	30	267	166	350	0.50	12	2	0	-	-	-	-	-
2b	77	231	185	350	0.50	300	12	0	16.0	8.0	5.85E-10	21.66	6.458
3	124	221	191	350	0.71	300	12	0	16.3	4.7	5.40E-10	21.48	6.551
4	196	204	204	350	0.70	1000	12	0	16.2	4.9	4.91E-10	21.24	6.670
5	255	221	211	350	1.00	-	-	0	16.2	-	9.67E-10	20.83	6.872
6	395	-485	-452	<30	1.00	-	-	0	16.3	-	3.32E-11	20.80	6.889
7	557	-512	-551	<30	1.00	-	-	0	19.6	-	1.24E-11	20.75	6.914

[a]Type 316 SS Heat C21, irradiated to 0.9 x 10^{21} n/cm^2 (1.35 dpa).
[b]Represents values in the effluent. Conductivity was ≈0.07 µS/cm in the feedwater.
[c]Based on effective yield stress, defined as the average of irradiated and nonirradiated yield stresses.
[d]The difference between the measured crack extension and that determined from the DC potential drop measurements was <5%.
[e]Crack length could not be determined because of a malfunction in the DC potential system.

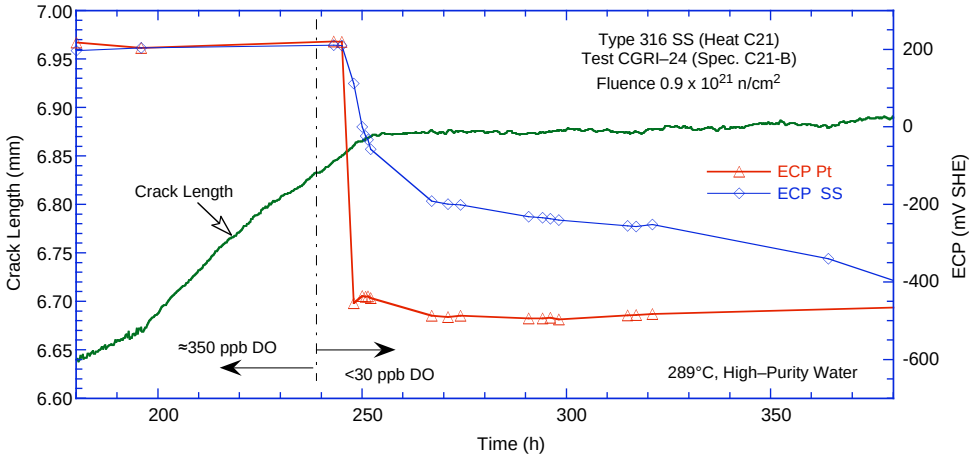

Figure 12. Change in crack length and ECP of Pt and SS electrodes during test periods 5-6 and the intermediate transition period.

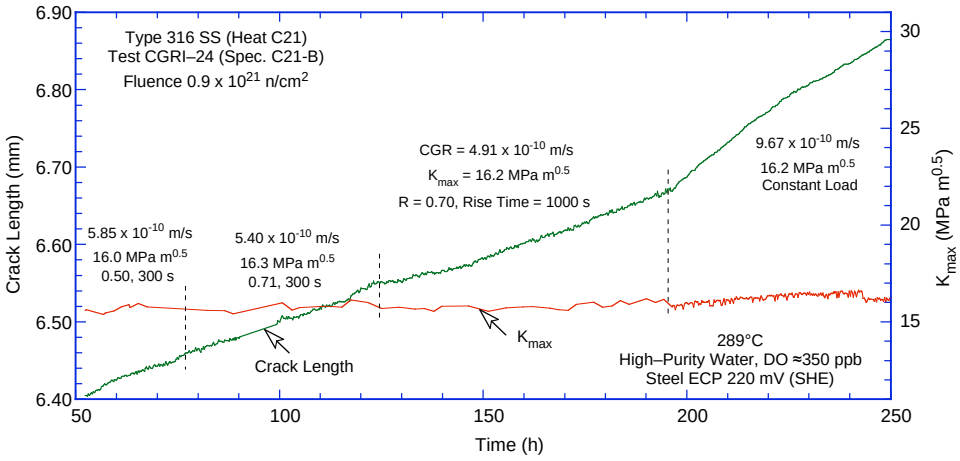

(a)

Figure 13. Crack-length-vs.-time plot for Type 316 SS in BWR water at 288°C during test periods (a) 2-5 and (b) 6-7.

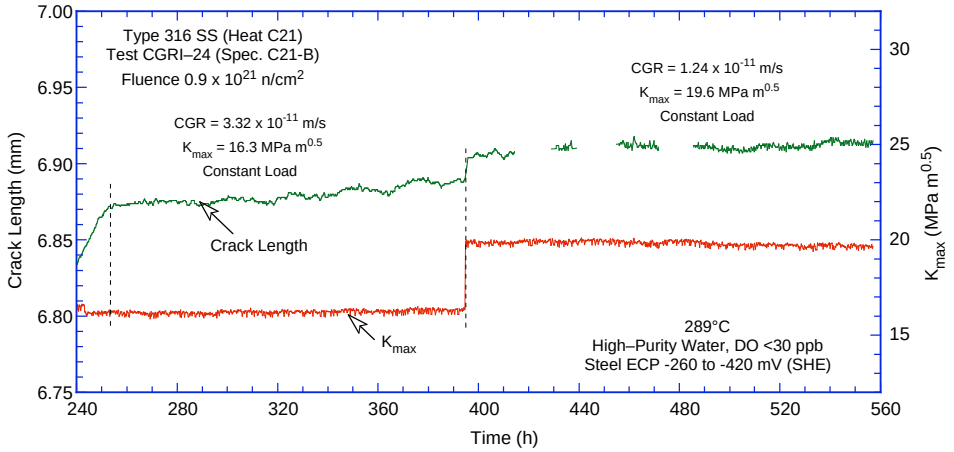

(b)

Figure 13. (Contd.)

After the CGR test, the final crack front was marked by fatigue cycling at room temperature in air. The specimen was then fractured, and the fracture surface of both halves of the specimen was photographed with a telephoto lens through the cell window. See Fig. 14. The final crack length was measured from the photograph by the 9/8 averaging technique; the difference in measured and estimated crack lengths was <5%. For this specimen, the K/size criterion was satisfied for all loading conditions.

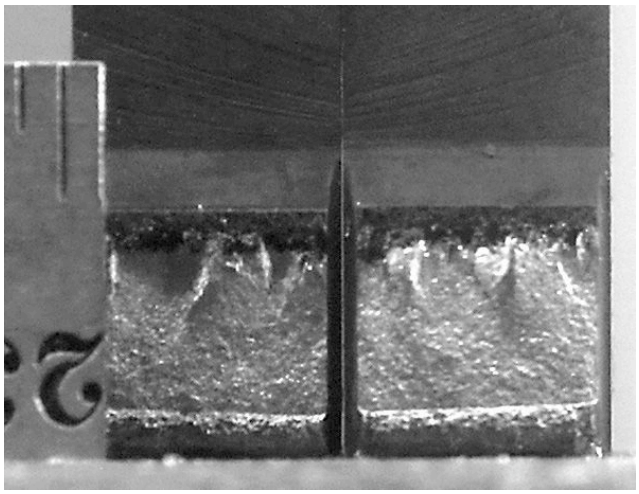

Figure 14.
Photomicrographs of the fracture surface of Specimen C21-B.

3.2.3.3 Specimen C21-C of Type 316 SS, Test CGRI-26

The test on Specimen C21-C of Type 316 SS irradiated to 3.0 dpa was started in high-purity water with ≈500 ppb DO and flow rate of 27 mL/min. The ECPs of a Pt and SS electrode located downstream from the autoclave were monitored continuously, and the effluent water conductivity and DO level were measured periodically. The system was operated for a few days to stabilize environmental conditions. The specimen was precracked at R = 0.33, K_{max} = 15.5 MPa $m^{1/2}$ (14.1 ksi $in.^{1/2}$), triangular waveform, and frequency of 1 Hz. After ≈0.4-mm (15.7-mil) crack advance, R was increased incrementally to 0.7, and the waveform changed to a slow/fast sawtooth with rise times of 30-1000 s. Finally, the specimen was subjected to a constant load. At 450 h [during test period 9c at constant load (K_{max} ≈22 MPa $m^{1/2}$ or ≈20.0 ksi $in.^{1/2}$)], the CGR increased abruptly by a factor of ≈6; the test was terminated at 510 h.

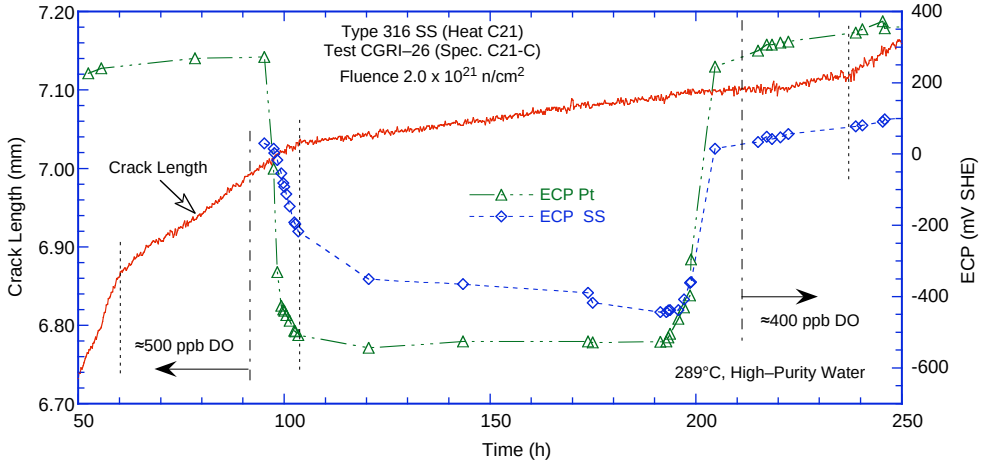

(a)

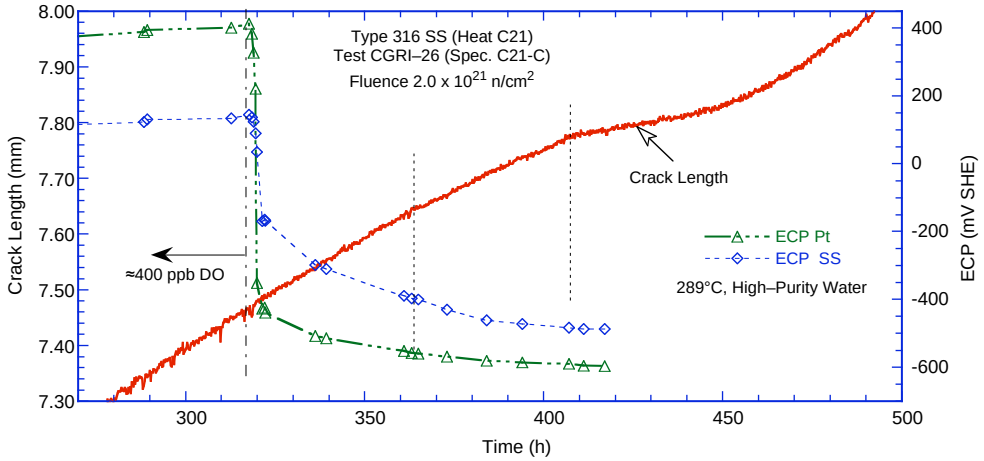

(b)

Figure 15. Change in crack length and ECP of Pt and SS electrodes during test periods (a) 3-5 and (b) 7-9.

The DO level in the effluent was decreased after 96 h from ≈500 ppb to <20 ppb, then at 192 h it was increased to ≈450 ppb, and finally at 318 h the DO was decreased below 20 ppb. The change in crack length and ECP of the Pt and SS electrodes during the transient periods are shown in Fig. 15. During the first change, the ECP of the Pt electrode decreased to below -450 mV (SHE) rather rapidly while the ECP of the SS electrode took nearly a day to decrease below -200 mV (SHE); it eventually decreased to about -400 mV. The CGR decreased significantly in the low-DO water (Fig. 15a); the change in CGR is abrupt and appears to have occurred when the ECP of the SS electrode decreased to about -200 mV. Similarly, when the DO content was increased from <20 ppb to ≈400 ppb, although the ECP of Pt and SS electrodes increased rapidly at ≈200 h, the CGR increased abruptly when the ECP of the SS electrode increased above ≈100 mV (Fig. 15a).

The crack growth behavior during the second decrease in the DO level at 318 h differed from that during the first DO decrease. The CGR did not decrease for nearly 100 h, even after the SS ECP had decreased below -400 mV (SHE) (Fig. 15b). The reason for the different behavior during the second decrease in the DO level is not clear. The applied K_{max} during the change in DO (from ≈270-360 h) was 23.5-25.0 MPa $m^{1/2}$ (21.4-22.7 ksi $in.^{1/2}$), which is equal to or marginally above the value allowed by the K/size criterion based on effective flow stress. To ensure compliance with the K/size criterion, K_{max} was

gradually decreased from ≈25.0 to 20.0 MPa $m^{1/2}$ (22.7-18.2 ksi $in.^{1/2}$). The CGR decreased for a about a day (Fig. 15b) and then increased back to approximately the growth rate prior to the decrease in K_{max}.

After the test the final crack size was marked by fatigue cycling in air at room temperature. The specimen was then fractured and the fracture surfaces of both halves of the specimen were photographed with a telephoto lens through the hot cell window. A photograph of the fracture surfaces is shown in Fig. 16. The final crack length of each half of the specimen was measured from the photograph by the 9/8 averaging technique. The actual crack length was ≈69% greater than the value determined from the DC potential measurements. The experimental crack extensions were scaled proportionately. The environmental and loading conditions, corrected CGRs, and allowed K_{max} based on the the K/size criterion are given in Table 13; the changes in crack length and K_{max} with time during the various test periods are plotted in Fig. 17.

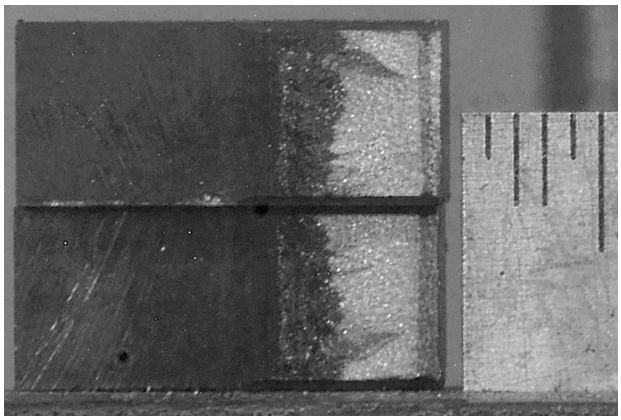

Figure 16.
Photograph of the fracture surfaces of the two halves of Specimen C21-C.

Table 13. Crack growth data for Specimen C21-C[a] of Type 316 SS in BWR water at 289°C.

Test Period	Test Time, h	ECP[b] mV (SHE) Pt	ECP[b] mV (SHE) Steel	O_2 Conc.,[b] ppb	R Load Ratio	Rise Time, s	Return Time, s	Hold Time, s	K_{max}, MPa $m^{1/2}$	ΔK, MPa $m^{1/2}$	Growth Rate, m/s	Allowed K_{max},.[c] MPa $m^{1/2}$	Crack Length,[d] mm
Pre	7	e	e	500	0.33	0.5	0.5	0	15.5	10.4	4.87E-08	27.7	6.404
1	29	249	e	500	0.52	30	5	0	15.7	7.5	3.12E-09	27.4	6.528
2	48	227	e	500	0.51	300	4	0	16.5	8.1	2.84E-09	26.9	6.708
3	56	241	e	500	0.71	1000	12	0	17.0	4.9	3.22E-09	26.7	6.797
4	103	241	e	500	1.00	-	-	-	17.6	-	1.06E-09	26.1	7.025
5	237	-507	-216	<30	1.00	-	-	-	17.9	-	1.77E-10	25.9	7.116
6	266	379	114	450	1.00	-	-	-	18.1	-	9.18E-10	25.6	7.212
7	321	328	124	450	1.00	-	-	-	23.6	-	1.21E-09	24.9	7.480
8	360	-551	-389	<30	1.00	-	-	-	24.9	-	1.06E-09	24.5	7.631
9a	409	-590	-483	<30	1.00	-	-	-	23.3[f]	-	7.85E-10	24.1	7.774
9b	442	-596	-487	<30	1.00	-	-	-	20.8[f]	-	3.12E-10	23.9	7.814
9c	506	-	-	<30	1.00	-	-	-	22.1	-	1.80E-09	23.1	8.097

[a]Type 316 SS Heat C21, irradiated to 2.0 x 10^{21} n/cm^2 (3.0 dpa).
[b]Represents values in the effluent. Conductivity and DO were ≈0.07 μS/cm and 600 ppb, respectively, in the feedwater.
[c]Based on effective yield stress, defined as the average of irradiated and nonirradiated yield stresses.
[d]Actual crack extension was 69% greater than the value determined from the DC potential drop measurements.
[e]Not measured.
[f]K_{max} was decreased during the test period; the listed value represents the average value for the period.

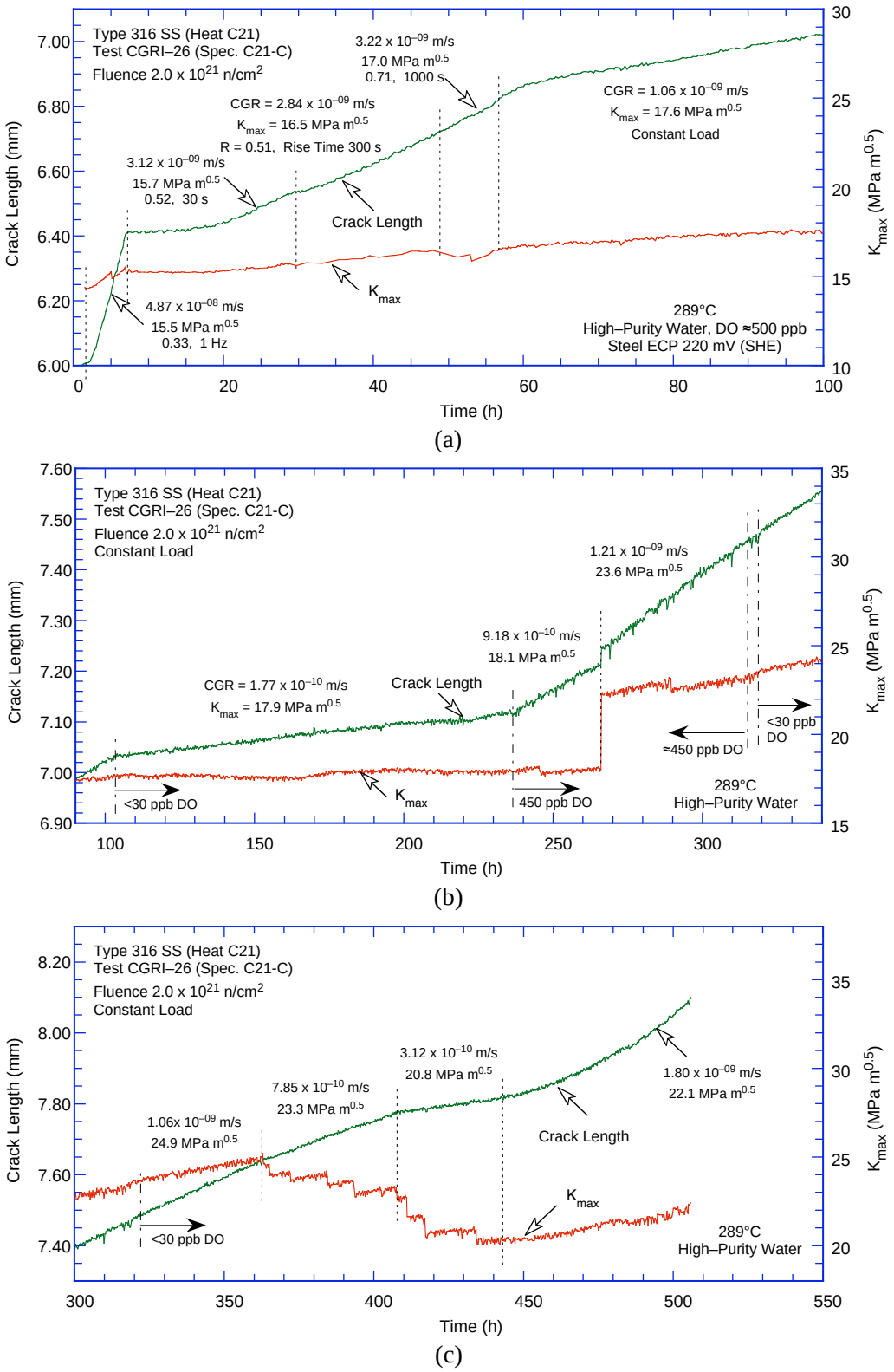

Figure 17. Crack-length-vs.-time plot for Type 316 SS in BWR water at 288°C during test periods (a) precracking-3, (b) 4-7, and (c) 8-9.

3.2.3.4 Specimen 85-3TT of Sensitized Type 304 SS, Test CGRIJR-31

The test on Specimen 85-3TT of sensitized Type 304 SS (Heat 10285) irradiated to 1.44 x 10^{21} n/cm^2 (2.16 dpa) was started in high-purity water at a flow rate of 22 mL/min. The system was operated for a few days to stabilize environmental conditions. The conductivity and DO in the feed water were 0.07 µS/cm and ≈300 ppb, respectively, and the DO content in the effluent was 300-350 ppb. The ECP of a companion SS sample located at the exit of the autoclave was ≈220 mV (vs. SHE) during the test. The frictional load was measured to be ±156 N (±35 lb); the results presented here have been corrected to account for this frictional load. The applied K_{max} and load ratio for each test period were determined by subtracting 156-N frictional load from the measured maximum load and adding 156 N to the measured minimum load. Fatigue precracking was carried out at R ≈ 0.42, K_{max} ≈ 14.9 MPa m$^{1/2}$ (13.5 ksi in.$^{1/2}$), triangular waveform, and frequency of 1 Hz. After ≈0.1-mm (3.9-mil) crack extension, to transition the transgranular (TG) fatigue crack to an IG crack, the loading waveform was changed to a sawtooth, and the load ratio was increased to ≈0.75 with rise time of ≈14 or 142 s and return times of 2 or 6 s. Finally, the specimen was subjected to a constant load (K_{max} = 15.7 MPa m$^{1/2}$ or 14.3 ksi in.$^{1/2}$) to obtain the SCC growth rate.

After fatigue precracking and transition of the transgranular TG fatigue crack to an IG crack, the DC potential measuring system was reinitialized, and a J-R test was performed on the specimen at 289°C (552°F) in high-DO (≈350 ppb) water. The test was conducted at a constant extension rate of ≈0.43 µm/s (0.017 mil/s). The test was interrupted periodically to measure the crack length by the DC potential drop measurements. The measured load vs. extension and the load-vs.-load-line displacement curves for Specimen 85-3TT are shown in Fig 18.

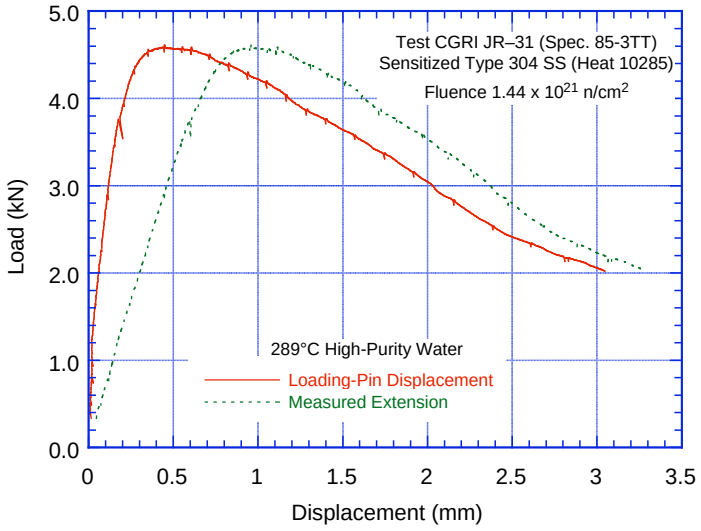

Figure 18.
Load vs. load-line displacement curve for Specimen 85-3TT tested in high-purity water at 289°C.

The final crack size was marked by fatigue cycling at room temperature. The specimen was then fractured, and the final crack length of both halves of the specimen was measured from a photograph of the fracture surface (Fig. 19). The actual crack extension was ≈28% greater than the value determined from the DC potential measurements. Crack extensions estimated from the DC potential method were adjusted accordingly. The results for the CGR test, including the allowed K_{max} from the K/size criterion, are given in Table 14; the changes in crack length and K_{max} with time are given in Fig. 20.

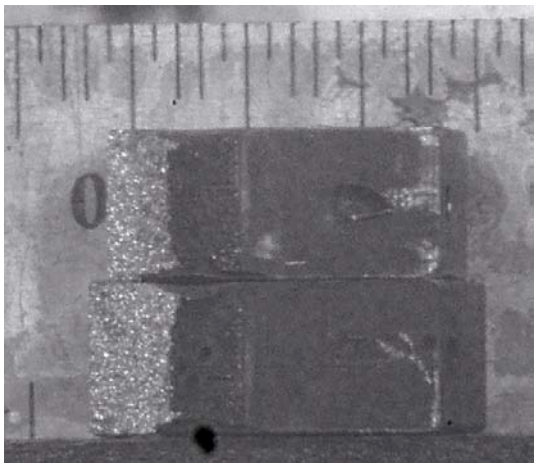

Figure 19.
Photograph of the fracture surface of Specimen 85-3TT tested in high-purity water at 289°C.

Table 14. CGR data for Specimen 85-3TT of sensitized Type 304 SS in high-purity water[a] at 289°C.

Test Period	Test Time, h	ECP[b] mV (SHE) Pt	ECP[b] mV (SHE) Steel	O_2 Conc.,[b] ppb	R Load Ratio	Rise Time, s	Return Time, s	Hold Time, s	K_{max}, MPa $m^{1/2}$	ΔK, MPa $m^{1/2}$	Growth Rate, m/s	Allowed K_{max},[c] MPa $m^{1/2}$	Crack Length,[d] mm
Pre	29	-	-	500	0.42	0.33	0.33	0.17/0.17	14.9	8.7	1.64E-08	20.4	5.911
1	93	200	218	500	0.74	142	5.7	158/6.3	15.3	4.0	1.02E-09	20.3	5.986
2	102	196	e	500	0.75	13.7	1.8	16.3/2.2	15.4	3.8	3.16E-09	20.2	6.027
3	195	e	e	500	0.95	140	1.7	860/10.3	15.7	0.7	2.22E-10	20.1	6.098
4	285	e	e	500	1.00	-	-	-	15.7	-	1.97E-10	20.0	6.161

[a]Type 304 SS Heat 10285, sensitized 10.5 h at 600°C, irradiated to 1.44 x 10^{21} n/cm^2 (2.16 dpa).
[b]Represents values in the effluent. Conductivity was ≈0.07 and 0.3 µS/cm in feedwater and effluent, respectively.
[c]Based on effective yield stress, defined as the average of irradiated and nonirradiated yield stresses.
[d]Actual crack extension was 28% greater than the value determined from the DC potential drop measurements.
[e]Not measured.

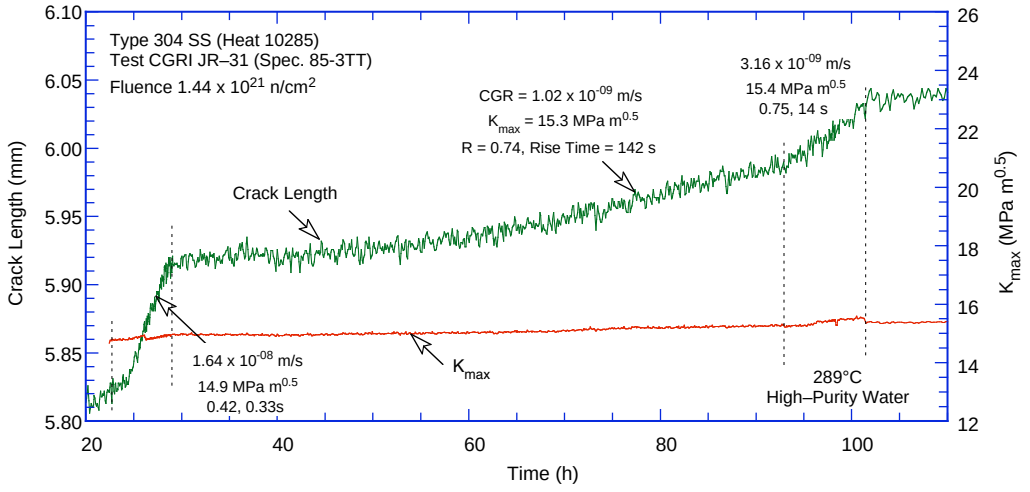

(a)

Figure 20. Crack-length-vs.-time plots for sensitized and irradiated Type 304 SS (Specimen 85-3TT) in high-purity water at 289°C during test periods (a) precracking-2 and (b) 3-4.

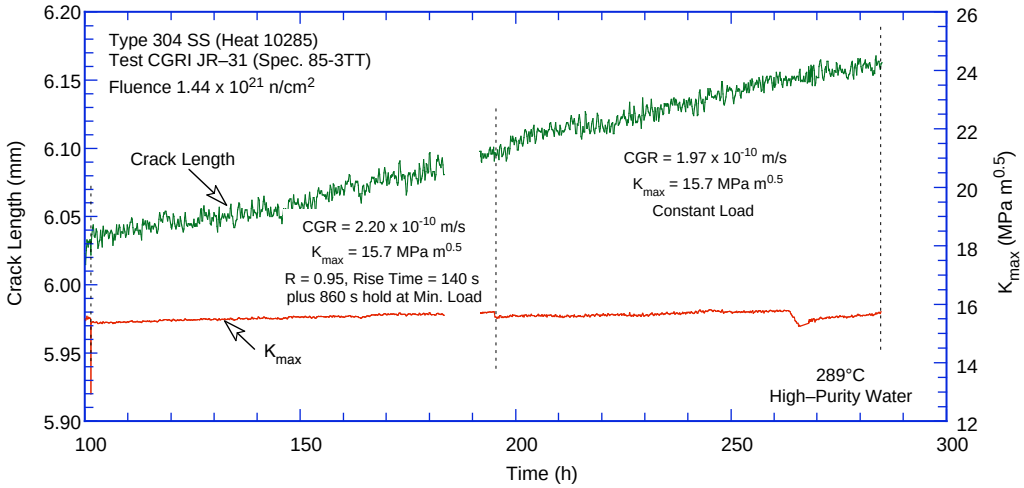

(b)

Figure 20. (Contd.)

The DC potential data during the J-R curve test were also corrected to account for the effects of plasticity on the measured potential. The fracture toughness J-R curve for Specimen 85-3TT in high-DO water is shown in Fig. 21. The results yield a J_{Ic} value of 176 kJ/m^2.

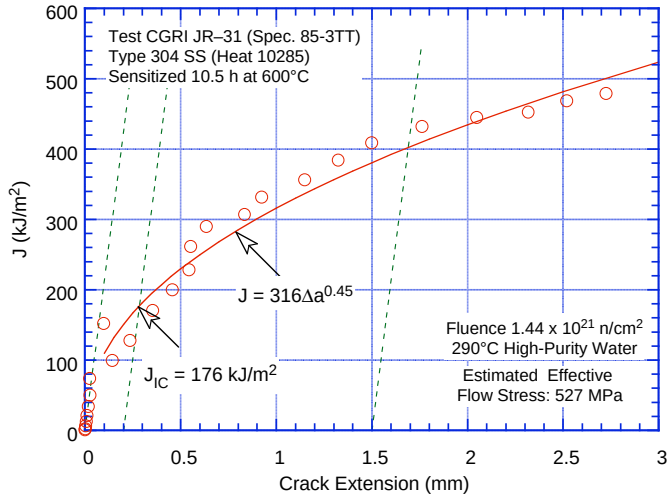

Figure 21.
Fracture toughness J-R curve for sensitized Type 304 SS irradiated to 1.44 x 10^{21} n/cm^2 (2.16 dpa) in high-DO water at 289°C.

3.2.3.5 Specimen 85-XA of Type 304 SS SMA Weld HAZ, Test CGRIJR-32

The test on Specimen 85-XA of Type 304 SS (Heat 10285) SMA weld HAZ irradiated to 1.44 x 10^{21} n/cm^2 (2.16 dpa) was started in high-purity water at a flow rate of 21 mL/min. The system was operated for a few days to stabilize environmental conditions. The conductivity and DO in the feed water were 0.06 µS/cm and ≈500 ppb, respectively, and the DO content in the effluent was ≈400 ppb. The ECP of a companion SS sample located at the exit of the autoclave was ≈220 mV (SHE) during the test. The frictional load was measured to be ±156 N (±35 lb); the results presented here have been corrected to account for this frictional load. The applied K_{max} and load ratio for each test period were determined by subtracting 156-N frictional load from the measured maximum load and adding 156 N to the measured minimum load.

Fatigue precracking was carried out at R = 0.42, K_{max} = 13.3 MPa $m^{1/2}$ (12.1 ksi $in.^{1/2}$), triangular waveform, and frequency of 2 Hz. After ≈0.12-mm (4.7-mil) crack extension, to transition the TG fatigue crack to an IG crack, the load ratio R was increased to ≈0.73, and the waveform changed from triangular to sawtooth with rise time of 26 or 433 s and unload time of 5.2 s. Finally, the specimen was subjected to a constant load (K_{max} ≈14.0 MPa $m^{1/2}$ or 12.7 ksi $in.^{1/2}$) to obtain the SCC growth rate.

After fatigue precracking and transition of the TG fatigue crack to an IG crack, the DC potential measuring system was reinitialized, and a J-R test was performed on the specimen at 289°C (552°F) in high-DO water (≈400 ppb DO). The test was conducted at a constant extension rate of ≈0.43 µm/s (0.017 mil/s). The test was interrupted periodically to measure crack length by the DC potential drop measurements. The measured load vs. extension and the load-vs.-load-line displacement curves for Specimen 85-XA are shown in Fig. 22.

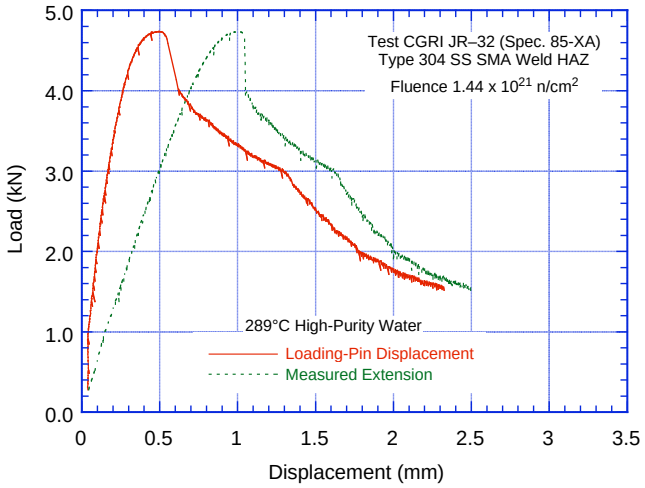

Figure 22.
Load vs. load-line displacement curve for Specimen 85-XA tested in high-purity water at 289°C.

The final crack size was marked by fatigue cycling at room temperature. The specimen was then fractured, and the final crack length of both halves of the fractured specimen was measured from the photograph of the fracture surface of Specimen 85-XA (Fig. 23). The actual crack extension was ≈16% greater than the value determined from the DC potential measurements. Crack extensions estimated from the DC potential method were adjusted accordingly. The results for the CGR test, including the allowed K_{max} from the K/size criterion, are given in Table 15; the changes in crack length and K_{max} with time are given in Fig. 24.

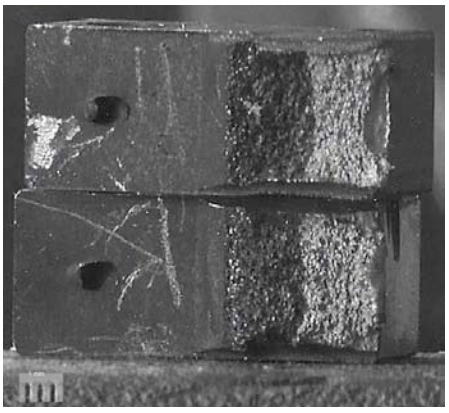

Figure 23.
Photograph of the fracture surface of Specimen 85-XA tested in high-purity water at 289°C.

Table 15. CGR data for Specimen 85-XA of Type 304 SMA weld HAZ in high-purity water[a] at 289°C.

Test Period	Test Time, h	ECP[b] mV (SHE) Pt	ECP[b] mV (SHE) Steel	O_2 Conc.,[b] ppb	R Load Ratio	Rise Time, s	Return Time, s	Hold Time, s	K_{max}, MPa $m^{1/2}$	ΔK, MPa $m^{1/2}$	Growth Rate, m/s	Allowed K_{max},[c] MPa $m^{1/2}$	Crack Length,[d] mm
Pre	51	e	205	500	0.42	0.16	0.16	0.09/0.09	13.3	7.7	1.86E-08	20.3	5.920
1	93	e	240	500	0.74	26	5.2	34/6.8	13.9	3.6	2.21E-09	20.2	6.006
2	140	e	236	500	0.72	433	5.2	567/6.8	13.0	3.6	7.07E-10	20.1	6.061
3	190	e	235	500	1.00	-	-	-	13.9	-	1.98E-10	20.0	6.132
4	331	e	210	500	1.00	-	-	-	14.0	-	2.61E-10	19.8	6.263

[a]Type 304 SS Heat 10285, shielded metal arc weld with HAZ irradiated to 1.44 x 10^{21} n/cm^2 (2.16 dpa).
[b]Represents values in the effluent. Conductivity was ≈0.07 and 0.3 µS/cm in feedwater and effluent, respectively.
[c]Based on effective yield stress, defined as the average of irradiated and nonirradiated yield stresses.
[d]Actual crack extension was 16% greater than the value determined from the DC potential drop measurements.
[e]Not measured.

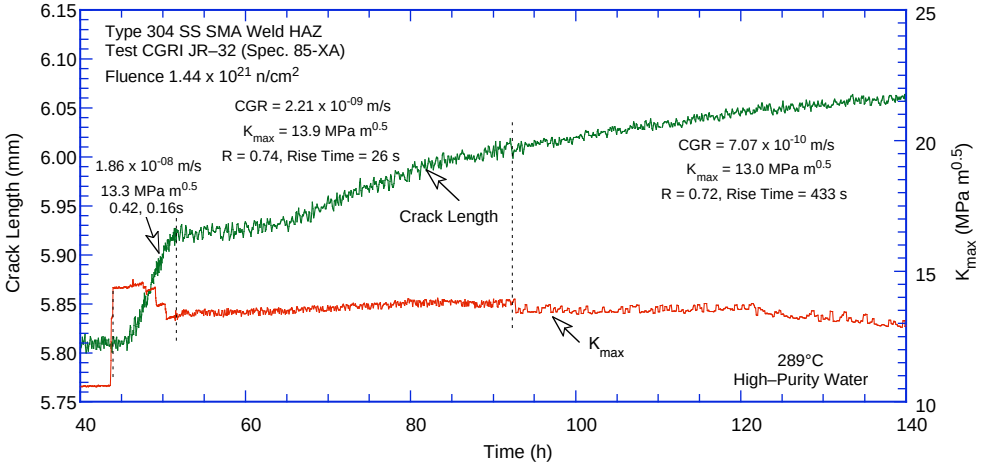

(a)

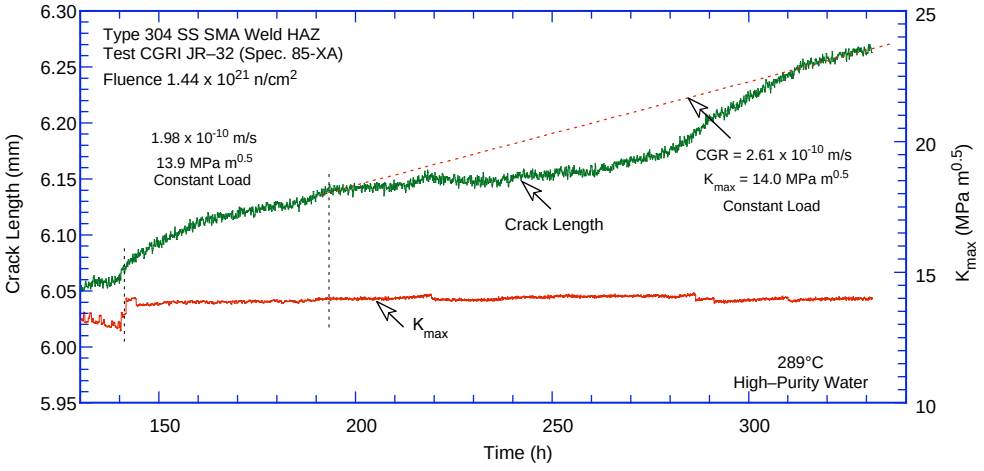

(b)

Figure 24. Crack-length-vs.-time plots for irradiated Type 304 SS SMA weld HAZ (Specimen 85-XA) in high-purity water at 289°C during test periods (a) precracking-2 and (b) 3-4.

The DC potential data during the J-R curve test were also corrected to account for the effects of plasticity on the measured potential. The fracture toughness J-R curve for Specimen 85-XA in high-DO water is shown in Fig. 25. The results yield a J_{Ic} value of 128 kJ/m^2.

The results indicate that the fracture toughness of the SMA weld HAZ material is significantly lower than that of the sensitized material from the same heat of Type 304 SS (e.g., J-R curve for Specimen 85-3TT in Fig. 21). However, examination through the hot cell window by telescope indicated that the fracture surface might not have been in the specimen HAZ. The fracture plane might have moved away from the HAZ region and into the weld metal, as indicated by Fig. 26. The sharp drop in load (Fig. 22) most likely is associated with this change in the fracture plane.

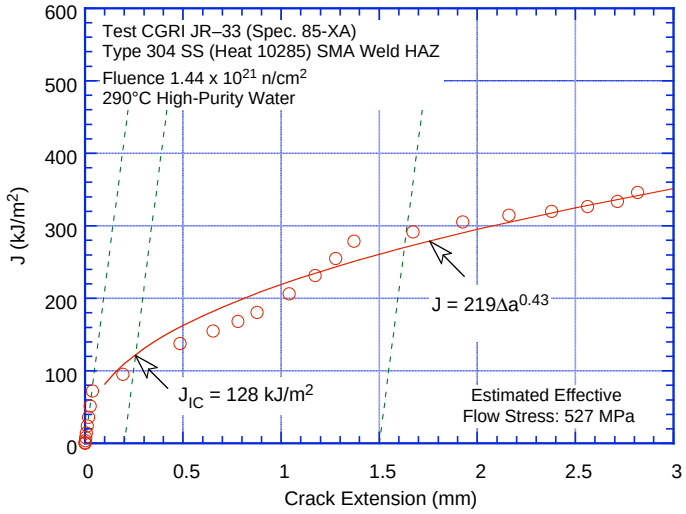

Figure 25.
Fracture toughness J-R curve for Type 304 SS SMA weld irradiated to 2.16 dpa in high-DO water at 289°C.

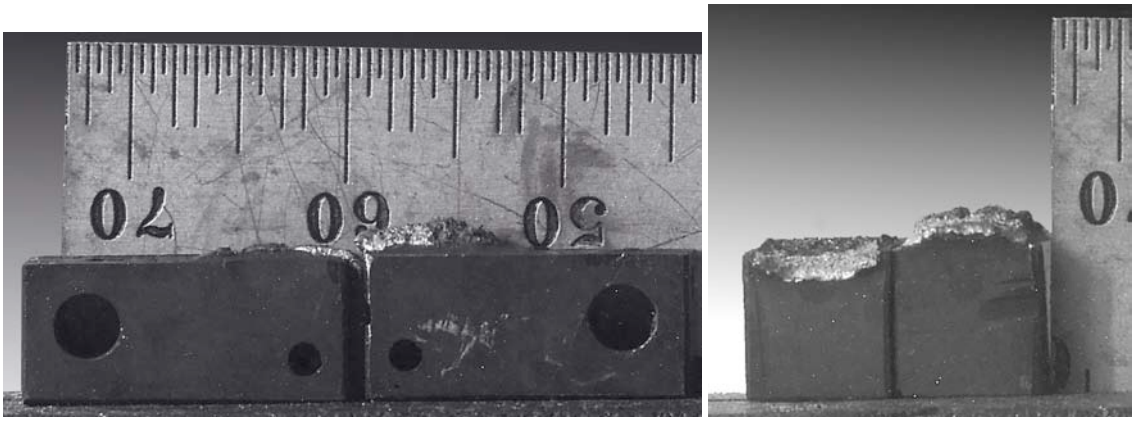

Figure 26. Fracture pieces of 85-XA test specimen: (a) side view and (b) end view.

3.2.4 CGRs of Austenitic SS under Constant Load with or without Periodic Unloading

3.2.4.1 Solution Annealed Materials

For crack growth tests under constant load with or without periodic unloading, the experimental CGRs for solution-annealed Types 304L, 316L, and 316 SS specimens in high- and low-DO environments (corresponding to NWC and HWC BWR environments, respectively) are shown in Fig. 27; data obtained earlier[80] are also included in the figure. Symbols shown with a "+" represent loading conditions that did not satisfy the specimen K/size criterion of Eq. 33. In the NWC BWR environment (Fig. 27a), the CGRs for austenitic SSs irradiated to ≈0.3 x 10^{21} n/cm^2 (≈0.45 dpa) are either comparable to or slightly below the disposition curve for sensitized SSs in water with 8 ppm DO given in NUREG-0313 (i.e., Eq. 28). For austenitic SSs irradiated to either 0.9 or 2.0 x 10^{21} n/cm^2 (≈1.35 or

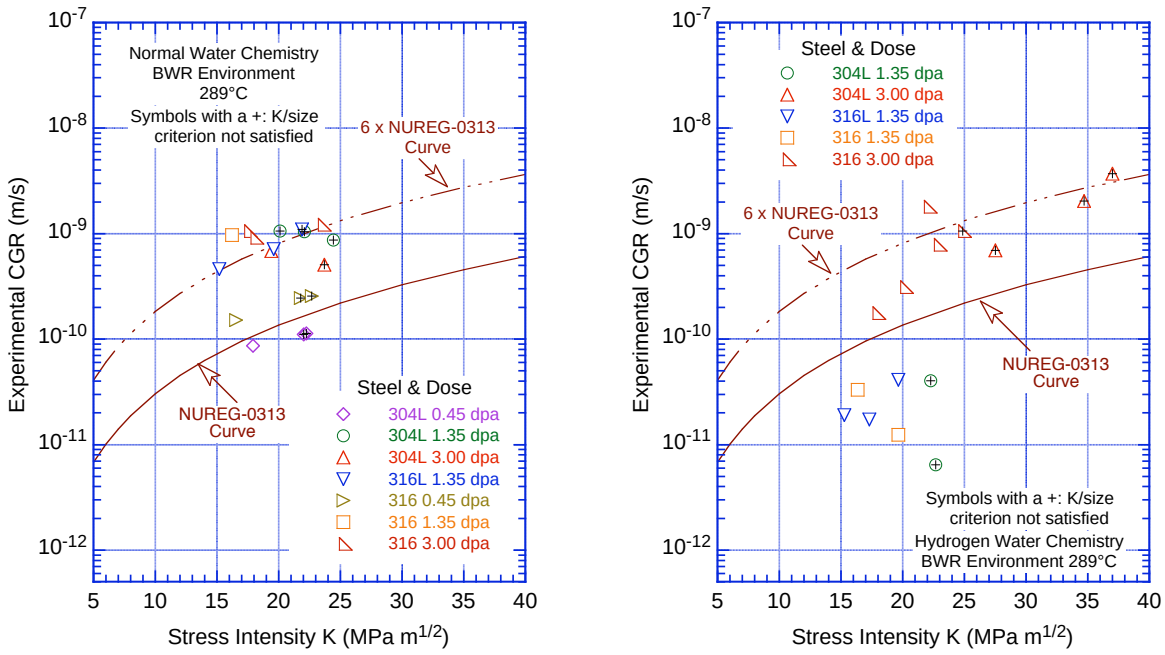

Figure 27. CGR data under constant load with periodic partial unloads for irradiated austenitic SSs in (a) normal water chemistry and (b) hydrogen water chemistry BWR water at 289°C.

3.0 dpa), the CGRs in the NWC BWR environment are comparable and a factor of ≈6 higher than the disposition curve for sensitized SSs in water with 8 ppm DO given in NUREG-0313.[82]

The results also indicate a benefit from a low-DO environment. In general, for the materials and irradiation conditions investigated in the present study, the constant load (or K) CGRs decreased more than an order of magnitude when the DO level was decreased from ≈300 to <30 ppb, i.e., from NWC to HWC BWR environment (Fig. 27b). A few specimens showed different behavior. For example, no benefit of the low-DO environment was observed for Heat C3 of Type 304L SS irradiated to 3.0 dpa (compare triangles in Fig. 27). For this specimen, the experimental CGR at ≈23.7 MPa $m^{1/2}$ (≈21.5 ksi $in.^{1/2}$) K_{max} remained at ≈5 x 10^{-10} m/s when the DO level was decreased from ≈300 to <20 ppb. The benefit of the low-DO environment was also not observed for Heat C21 during the second decrease in DO level at K_{max} ≈23.6 MPa $m^{1/2}$ (Table 13 and the right-angle triangles in Fig. 27). Although the CGR decreased by an order of magnitude when the DO level was decreased at K_{max} ≈17.6 MPa $m^{1/2}$ (16.0 ksi $in.^{1/2}$), it did not change when the DO level was decreased at 23.6 MPa $m^{1/2}$. At present, the reason for this behavior is not clear. For Heat C3, it may be caused by loss of specimen constraint because the applied K_{max} was 44% greater than the value allowed by the K/size criterion (Eq. 33) based on the effective yield stress (defined as the average of the irradiated and nonirradiated yield stresses). Experimental CGRs obtained under loading conditions that exceeded the K/size criterion are shown in Fig. 28; the numbers next to the data points represent the percentage by which the applied K_{max} exceeded the allowed value.

Loading conditions that exceed the K/size criterion should also influence the fracture mode. For example, if the thickness criterion is exceeded, the crack plane will be out-of-normal near the edges of the specimen, and if the specimen ligament criterion is exceeded, the crack would grow away from the normal plane. A detailed metallographic examination of the specimen of Heat C3 suggests that, although the proposed specimen size criterion was not met at the time when the DO level was decreased from ≈400

to 20 ppb, there is no fractographic indication of a loss in constraint in the specimen.[89] The fracture morphology was completely IG, and the fracture plane was relatively straight and normal to the stress axis. Additional data on Types 304 and 316 SS irradiated to 3-5 dpa are needed to better establish the effect of decreased DO level on the CGRs of irradiated austenitic SSs.

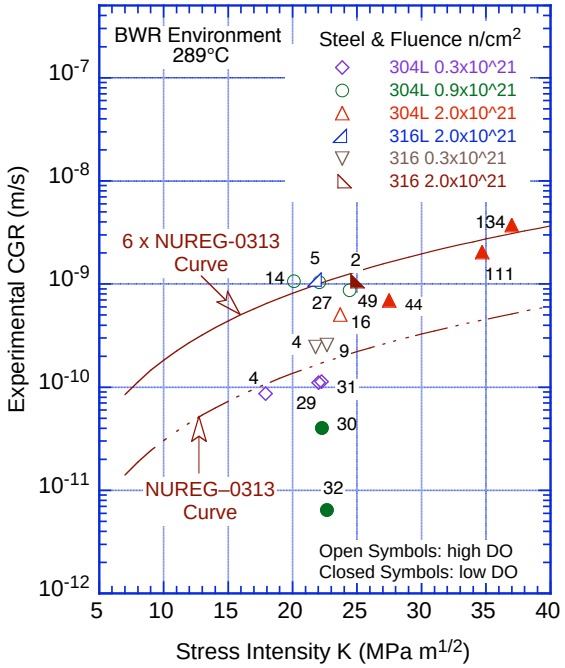

Figure 28.
Experimental CGRs for irradiated austenitic stainless steels obtained in high- and low-DO BWR environments under loading conditions that exceed the K/size criterion. The numbers next to the data points represent the difference (in %) between the applied and allowed K_{max}.

3.2.4.2 Stainless Steel Weld HAZ Materials

For crack growth tests under constant load with or without periodic unloading, the experimental CGRs for nonirradiated and irradiated Types 304L and 304 SS SA or SMA weld HAZ specimens in high- and low-DO environments are shown in Fig. 29; data obtained earlier[81] are also included in the figure. Because of the relatively low flow stress of the nonirradiated materials, the applied K_{max} for most of the test periods did not satisfy the K/size criterion of ASTM E-1681. In addition, for the Type 304 SS SMA weld HAZ specimen (data shown as right angle triangles in Fig. 29a), the fracture plane was not normal to the stress axis but at an angle of 45°; therefore, the CGR for this specimen is not included in Fig. 29a.

For nonirradiated Type 304L weld HAZ from the Grand Gulf (GG) BWR, although some of the data did not meet the K/size criterion of ASTM E-1681, the as-welded (triangles in Fig. 29a) and as-welded plus thermally-treated (squares in Fig. 29a) materials have comparable CGRs. For both conditions, the CGRs are a factor of ≈2 lower than the NUREG-0313 curve for sensitized SSs in water with 8 ppm DO. These results are in good agreement with the CGR of 1×10^{-10} m/s obtained by Andresen et al.[90] for the GG Type 304L weld HAZ in high-DO water (2000 ppb DO) at 288°C (550°F) and K_{max} = 27.4 MPa $m^{1/2}$ (24.9 ksi $in.^{1/2}$).

Irradiation to 5.0×10^{20} n/cm^2 (≈0.75 dpa) increased the growth rates of all SS weld HAZ materials. The CGRs of irradiated HAZ specimens are a factor of 2-5 higher than those predicted by the NUREG-0313 disposition curve for sensitized SSs in high-DO water. A beneficial effect of reducing the corrosion potential of the environment was observed for all materials that were tested in the BWR

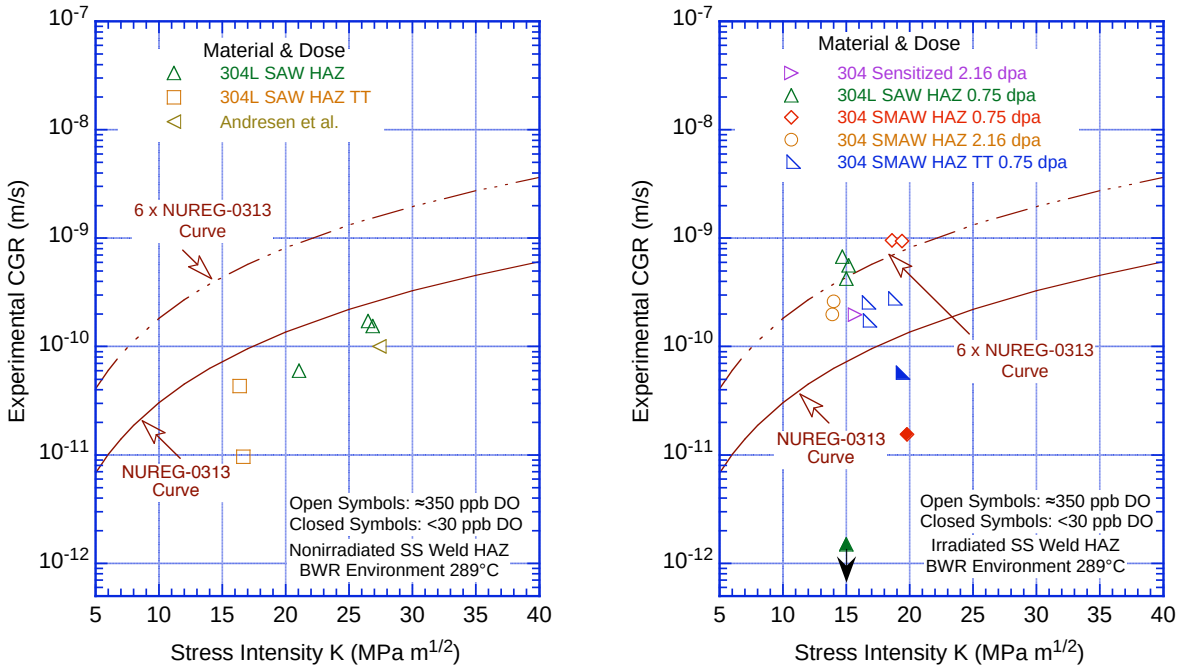

Figure 29. CGR under constant load with periodic partial unloads for (a) nonirradiated and (b) irradiated SS weld HAZ specimens in high-purity water at 289°C.

environment. The growth rates of irradiated or nonirradiated Type 304 weld HAZ decreased by an order of magnitude or more when the DO was decreased from ≈300 ppb to <30 ppb.

The fracture morphology for irradiated Type 304 weld HAZ is similar to that of the nonirradiated material. It is IG under environmentally enhanced (or SCC conditions), and TG under mechanical fatigue (or conditions that show little or no environmental enhancement). However, the fracture morphology of the Type 304L and Type 304 SS weld HAZ materials was different; for example, it was TG for the Type 304L SA weld HAZ and IG for the Type 304 SMA weld HAZ. A TG morphology is unusual in SS weld HAZ because the presence of residual strain in the material typically promotes IG crack growth even in nonsensitized SS. [90-92] An IG fracture is always observed in cold-worked SSs.

3.2.5 CGRs of Austenitic SS under Continuous Cycling

3.2.5.1 Solution Annealed Materials

Under continuous cyclic loading, the experimental CGRs and those predicted in air for the same loading conditions for solution-annealed Types 304 and 316 SSs irradiated up to 3 dpa and tested in high- and low-DO environments are plotted in Fig. 30. The curves in the figures are based on the superposition model (Eq. 22). The corrosion fatigue contribution to growth rates was determined from the Shack/Kassner models for nonirradiated austenitic SSs in high-purity water with either 8 or 0.2 ppm DO (Eqs. 26 and 27, respectively), and the SCC contribution was determined from Eq. 28. As discussed in Section 3.2.4.1, CGRs for SSs irradiated to >0.75 dpa are a factor of 6 higher than those predicted by Eq. 28. Also, for cyclic loading, an equivalent K_{max} was computed to determine SCC growth rates; the average values used in the superposition curves are given in Fig. 30. The CGRs in air were determined from Eq. 23 developed by James and Jones.[86]

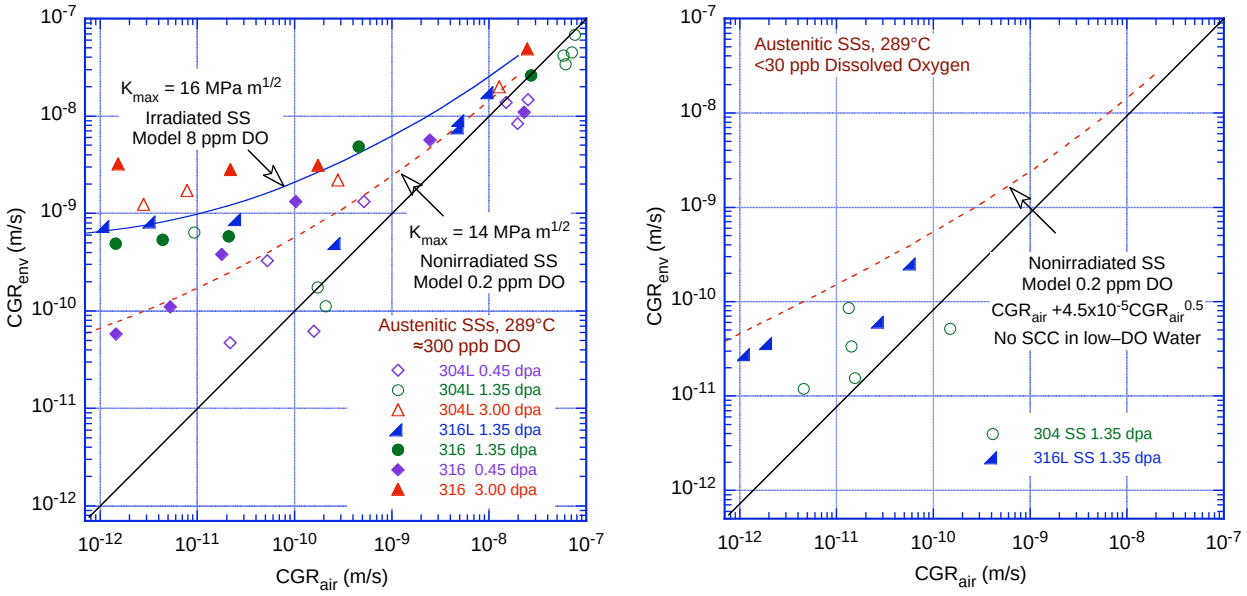

(a) (b)

Figure 30. CGR for irradiated specimens of austenitic SSs under continuous cycling at 289°C in high-purity water with (a) ≈300 ppb and (b) <30 ppb dissolved oxygen.

In these figures, the data points that lie along the diagonal represent predominantly mechanical fatigue, and those that lie close to the model curve indicate environmentally enhanced crack growth. The austenitic SS irradiated to 0.3 x 10^{21} n/cm^2 (0.45 dpa) shows very little environmental enhancement of the cyclic CGRs in high-DO water (open diamonds in Fig. 30a). Using Eqs. 22-28, the CGRs in water with ≈ 300 ppb DO may be represented by the NUREG-0313 curve and the Shack/Kassner model for nonirradiated austenitic SSs in high-purity water with 0.2 ppm DO.

The results for SSs irradiated to 0.9 or 2.0 x 10^{21} n/cm^2 (1.35 or 3.0 dpa) indicate significant enhancement of the CGRs in high-DO water under cyclic loading with long rise times. For these irradiation conditions, the CGRs in water with ≈ 300 ppb DO may be represented by the $\dot{a}_{SCC}$ curve for irradiated SSs (i.e., 6 x NUREG-0313 curve) and the Shack/Kassner model for nonirradiated austenitic SSs in high-purity water with 8 ppm DO.

For continuous cyclic loading, decreasing the DO level has a beneficial effect on CGRs. Decreasing the DO from ≈300 ppb DO to <30 ppb DO results in a factor of 25 decrease in the CGR. The growth rates are lower for the irradiated steels in water with <30 ppb DO than for nonirradiated austenitic SSs in high-purity water with 0.2 ppm DO (Fig. 30b).

3.2.5.2 Stainless Steel Weld HAZ Materials

The experimental CGRs for irradiated Type 304 SMA weld HAZ specimens in high-DO water and those predicted in air for the same loading conditions are plotted in Fig. 31. Results from tests performed on nonirradiated material are also included in the figures.[81] As before, the curves in the figure are based on the superposition model. In Fig. 31, the loading conditions for the data points shown with a "+" did not satisfy the K/size criterion of ASTM E-647.

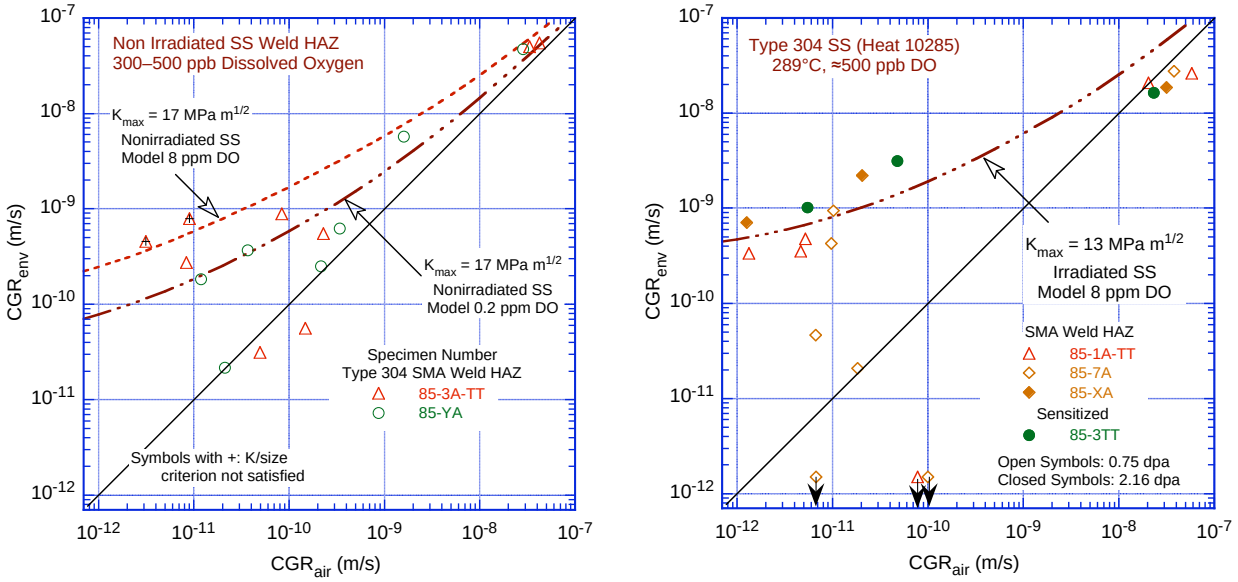

(a) (b)

Figure 31. CGR for (a) nonirradiated and (b) irradiated specimens of laboratory-prepared Type 304 SS SMA weld HAZ under continuous cycling in high-purity water at 289°C.

The results indicate significant environmental enhancement of CGRs for both nonirradiated and irradiated weld HAZ materials. However, for the nonirradiated specimens, the CGR did not increase readily when the load ratio and rise time were increased. For example, a large number of data points lie along the diagonal in Fig. 31a. The applied K_{max} had to be increased for enhanced growth rates. The growth rates of the nonirradiated HAZ materials in water with 300-500 ppb DO may be represented by superposition of the NUREG-0313 curve and the Shack/Kassner model for nonirradiated austenitic SSs in high-purity water with 0.2 ppm DO. For irradiated HAZ materials, the CGRs may be represented by superposition of the $\dot{a}_{SCC}$ curve for irradiated SSs and the Shack/Kassner model for corrosion fatigue of nonirradiated austenitic SSs in high-purity water with 8 ppm DO. For both irradiated and nonirradiated HAZ materials, thermal treatment of the material for 24 h at 500°C (932°F) has little or no effect on growth rates.

3.2.6 Fracture Toughness of Irradiated Austenitic SS Weld HAZ in High-Purity Water at 288°C

The fracture toughness J_{IC} from the tests performed in the present study and those obtained from an earlier study at ANL[80] are compared with similar data from other studies on BWR irradiated materials in Fig. 32. The scatter band for the data from fast reactor irradiations is also plotted in the figure. The results from tests in water show the same general trend in embrittlement, but are lower than those from tests in air.

A water environment could influence fracture toughness in two ways. First, an IG starter crack compared to a TG fatigue crack used in nearly all the fracture toughness tests may decrease the J_{IC} value for the material. Secondly, the effect of the corrosion/oxidation reaction during crack extension may decrease the tearing modulus. For example, hydrogen generated from the oxidation reaction can diffuse into the material and change its deformation behavior ahead of the crack tip by changing the stacking fault energy. However, the effect of test environment on fracture toughness cannot be accurately established from these results. Fracture toughness tests were not conducted on the same material in both

air and water environments. Controlled companion tests in air are in progress to determine the effect of water environment on fracture toughness.

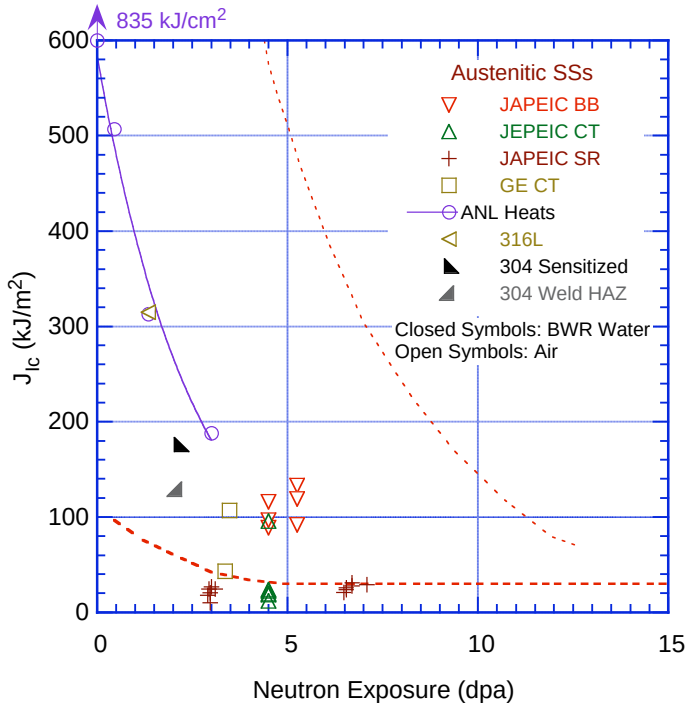

Figure 32.
Change in fracture toughness J_{Ic} as a function of neutron exposure for irradiated austenitic SSs. Dashed lines represent the scatter band for the fast reactor data on austenitic SSs irradiated at 350-450°C.

GE = General Electric Nuclear Energy, JAPEIC = Japan Power Engineering and Inspection Corporation, CT = compact tension, BB = bend bar, and SR = short rod.

4 Causes and Mechanisms of Irradiation-Assisted Cracking of Austenitic Stainless Steel in PWRs

4.1 Introduction

Irradiation-assisted stress corrosion cracking (IASCC) has been found in various core internal components in commercial and test PWRs. Failures of fuel cladding, control rod cladding, and core baffle bolts in PWRs reveal a similar IG fracture as observed in BWRs.[93,94] Thanks to the low corrosion potential of hydrogen water chemistry, the typical neutron dose threshold for IASCC is about one order of magnitude higher in PWRs (i.e., >10 dpa) than in BWRs with normal water chemistry (i.e., ~0.7 dpa). Chromium depletion at grain boundaries is considered not as critical for IASCC sensitivity in PWRs as that in BWRs.[95-97] At present, the database for PWR core internals is limited, and the key metallurgical variables for IASCC under the PWR environment still need to be identified. A better mechanistic understanding of IASCC behavior in the PWR environment is crucial not only for devising possible countermeasures to mitigate IASCC but also for developing predictive and regulatory methodology.

Because of the higher dose threshold, irradiation damage is believed to play a more important role in the IASCC of PWR core internals. Whether or not irradiation embrittlement alone is sufficient to explain the IG cracking in PWRs needs to be further studied. Unlike BWRs, control rods are not used as a primary means to regulate life-cycle reactivity in PWRs. Soluble B is added to the PWR coolant, and its concentration is adjusted throughout a fuel cycle to control the reactivity. As a result of this difference, the thermal-to-fast flux ratio varies with time in PWRs, and the fast neutron flux is about 20-30% higher in PWRs than in BWRs.[94] The damage rate of core internals is thus somewhat higher in PWRs. Combined with a higher operation temperature [≈320°C (608°F)] in the PWR primary loop, the kinetics of radiation damage in PWR core internals can be different from that in BWR core internals. The contribution of radiation-induced microstructure and microchemistry to IASCC behavior at PWR relevant dose and temperature is being evaluated in the current study.

Void swelling is another issue associated with the high dose level at the end of life (EOL) in PWRs. Previously, the volumetric instability caused by swelling was mainly a concern in fast breeder reactors and fusion systems. The peak temperature of void swelling was found to be around 550-600°C (1022-1112°F) for austenitic SSs.[98,99] The void swelling at the temperature relevant to LWRs is insignificant and was not considered as a problem for either PWRs or BWRs within their service life. More recently, Garner and Toloczko pointed out that the predicted void swelling based on the fast breeder reactor data may not properly represent the situation in LWRs.[100] The lower damage rate (~10^{-7} dpa/s) in LWRs may reduce the incubation limit and shift the peak swelling temperature towards the low temperature region. Combined with the fear that elevated temperature [up to 450°C (842°F)] might occur due to γ radiation heating in the thick section of components, the concern of void swelling is realistic for the EOL dose level of PWRs. This concern triggered a recent literature survey of void swelling under the PWR relevant conditions.[101] With very limited data on decommissioned components from PWRs, the study confirmed the previous conclusion that the void swelling is relatively small under PWR condition. However, to ensure the volumetric stability of components at the EOL of PWRs, this task will examine the void swelling behavior of austenitic SSs under PWR relevant dose and temperature.

The objectives in this task are to evaluate the susceptibility of austenitic SS core internals to IASCC in PWRs as a function of the fluence, water chemistry, material chemistry, and cold-work. Both SSRT tests and microstructure examination will be performed on specimens irradiated at PWR relevant dose and temperature. The program will mainly focus on: (a) evaluation of the effects of PWR-like high fluence on the susceptibility to IASCC; (b) neutron irradiation embrittlement as reflected in loss of ductility and

fracture toughness; (c) void swelling behavior in austenitic SSs at PWR-relevant dose and temperature; (d) effect of cold-work and solution anneal; (e) fracture toughness and SCC behavior of cast duplex SSs at high fluence; and (f) effectiveness of mitigating measures, such as grain-boundary engineering and minimization of S concentration. Tests will be conducted on SS specimens irradiated in the BOR-60 reactor in Russia.

4.2 Irradiation of Austenitic Stainless Steels in the BOR-60 Reactor (Y. Chen, W. K. Soppet, and O. K. Chopra)

Irradiation experiments for this task are conducted in the BOR-60 reactor, a sodium-cooled fast breeder reactor located in the Research Institute of Atomic Reactor (RIAR), Dimitrovgrad, Russia. Various austenitic SSs and Alloy 690 are included in the irradiation. Table 16 provides the chemical compositions of the materials. Two types of specimens, flat tensile specimens (Fig. 33) and transmission electron microscope (TEM) disks [3 mm (0.118 in.) in diameter], are irradiated at target doses of 5, 10, 20, and 40 dpa in two irradiation cycles, Boris 6 and Boris 7. By the end of this reporting period, Boris 6 irradiation, which includes 5, 10, and 20 dpa specimens, had been completed, and Boris 7 irradiation was in progress. The tensile specimens were separated in bundles (four specimens in each bundle) and were in contact with the sodium coolant during irradiation. The TEM disks were contained in four weeper capsules and one He-tight capsule, as shown in Fig. 34.

The Boris 6 irradiation was from June 2001 to March 2003 and included eight irradiation sub-cycles and several shut-down periods for reactor maintenance. The irradiation was conducted in the fifth row of the core of the BOR-60 reactor. Neutron fluence was monitored by five dosimeters loaded in the central channel of the irradiation rig and in baskets with the specimens. The analyses of dosimeters were carried out in RIAR after irradiation, and the accuracy of the calculated neutron fluence was reportedly better than 7%.[102] Irradiation temperature was controlled by monitoring the inlet and outlet sodium temperatures, which were kept at ≈315 and 325°C (≈599 and 617°F), respectively; Mg-Zn eutectic thermal monitors were also placed among specimens in several baskets to ensure that the irradiation temperature was below 343°C (649°F).

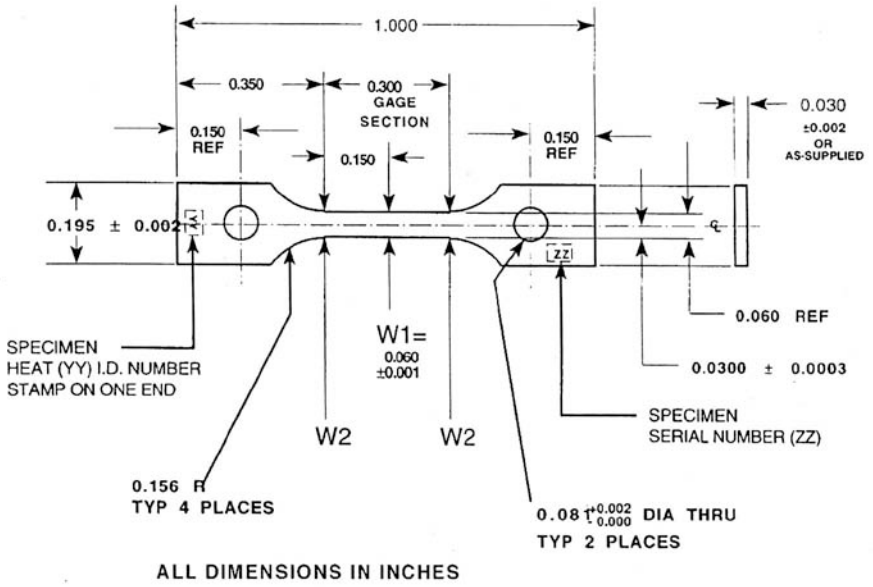

Figure 33. Schematic of BOR-60 flat SSRT specimen.

Table 16. Materials irradiated in BOR-60 reactor (wt.%).

Material Type[a]	Heat ID	Mater. Code	Composition (wt.%)								
			Ni	Si	P	S	Mn	C	N	Cr	Other Elements [b]
347 SA	316642	D1	10.81	0.29	0.023	0.014	1.56	0.030	0.021	18.06	Nb 0.60, Mo 0.29, Cu 0.09
347 CW	316642CW	D2	10.81	0.29	0.023	0.014	1.56	0.030	0.021	18.06	Nb 0.60, Mo 0.29, Cu 0.09
304 SA	2333	B1	8.5	0.65	0.031	0.029	1.38	0.035	0.068	18.30	Mo 0.37
304 CW	2333CW	B2	8.5	0.65	0.031	0.029	1.38	0.035	0.068	18.30	Mo 0.37
316 LN SA	623	B3	12.20	0.70	0.007	0.002	0.97	0.019	0.103	17.23	Mo 2.38, Cu 0.21
316 LN-Ti SA	625	B4	12.30	0.72	0.007	0.002	0.92	0.012	0.064	17.25	Mo 2.39, Ti 0.027, Cu 0.21
316 SA	C21	B5	10.24	0.51	0.034	0.001	1.19	0.060	0.020	16.28	Mo 2.08, B<0.001
316 CW	C21 CW	B6	10.24	0.51	0.034	0.001	1.19	0.060	0.020	16.28	Mo 2.08, B<0.001
316 WW	C21 WW	B7	10.24	0.51	0.034	0.001	1.19	0.060	0.020	16.28	Mo 2.08, B<0.001
CF-3 cast SS	52	C1	9.40	0.92	0.012	0.005	0.57	0.009	0.052	19.49	Mo 0.35, δ13.5%
CF-8 cast SS	59	C2	9.34	1.08	0.008	0.007	0.60	0.062	0.045	20.33	Mo 0.32, δ13.5%
304 SA	C1	A1	8.12	0.50	0.038	0.002	1.00	0.060	0.060	18.11	B 0.001
304 SA	C9	A2	8.75	0.39	0.013	0.013	1.72	0.062	0.065	18.48	B <0.001
304 SA	C12	A3	8.23	0.47	0.018	0.002	1.00	0.060	0.070	18.43	B <0.001
304 CW	C1 CW	A1	8.12	0.50	0.038	0.002	1.00	0.060	0.060	18.11	B 0.001
304 CW	C12 CW	A5	8.23	0.47	0.018	0.002	1.00	0.060	0.070	18.43	B <0.001
304 GBE	304 GBE	A6	8.43	0.46	0.014	0.003	1.54	0.065	0.088	18.38	Mo 0.51, Co 0.22
316 GBE	316 GBE	B8	11.12	0.57	0.011	0.022	1.85	0.070	0.056	16.57	Mo 2.27, Co 0.10
690 GBE	690 GBE	E1	59.40	0.30	-	0.003	0.42	0.010	-	29.10	Fe 10.26
304 BASE	304 BASE	A7	8.46	0.41	0.013	0.014	1.56	0.065	0.086	18.32	Mo 0.36, Co 0.12
316 BASE	316 BASE	B9	10.30	0.43	0.013	0.020	1.53	0.055	0.054	16.42	Mo 2.19, Co 0.10
690 BASE	690 BASE	E2	61.49	0.05	-	<0.01	0.15	0.030	-	29.24	Fe 9.02
HP 304L SA	945	A8	9.03	0.03	<0.005	0.005	1.11	0.005	0.003	19.21	O 0.047, Mo <0.005
HP 304L SA	1327	A9	9.54	0.01	0.001	0.002	1.12	0.006	<0.001	19.71	O 0.008, Mo 0.02
304L SA	C3	A10	8.91	0.46	0.019	0.004	1.81	0.016	0.083	18.55	B< 0.001
304L CW	C3 CW	A11	8.91	0.46	0.019	0.004	1.81	0.016	0.083	18.55	B< 0.001
304-like alloy	L5	A12	9.66	0.90	0.113	0.028	0.47	0.006	0.033	21.00	B<0.001

[a] SA = solution annealed; CW = cold worked; WW = warm worked at 400°C; SS = stainless steels; GBE = grain boundary engineered; BASE = base heat for GBE modification; HP = high purity.
[b] δ = ferrite content.

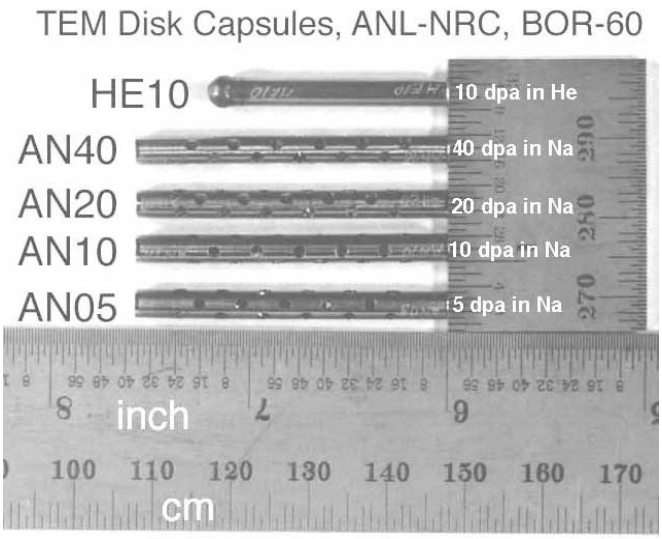

Figure 34.
TEM capsules irradiated in the BOR-60 reactor.

The Boris 6 irradiation specimens were discharged at different times between 2001 and 2003 according to specified doses. All specimens were first cleaned of residual sodium and then transferred to ANL via Studsvik and Westinghouse in 2005. In total, 48 tensile specimens and 166 TEM disks were irradiated during the Boris 6 cycle, as listed in Table 17. The actual doses received by individual specimens are given in Table 18.

Table 17. Available specimens from Boris 6 irradiation.

Material Type[a]	Heat ID	Material Code	SSRT Specimens [b]		TEM Disks [b]			
			5 dpa	10 dpa	AN05 5 dpa	AN10 10 dpa	HE10 10 dpa (He capsule)	AN20 20 dpa
347 SA	316642	D1	1	2	2	1	1	1
347 CW	316642CW	D2	2	2	2	1	1	2
ABB 304 SA	2333	B1	-	2	2	1	1	2
ABB 304 CW	2333 CW	B2	-	2	2	1	1	2
316LN SA	623	B3	1	2	2	1	1	2
316LN-Ti SA	625	B4	1	2	2	1	1	2
316 SA	C21	B5	1	3	2	1	1	2
316 CW	C21 CW	B6	2	3	2	1	1	1
316 WW	C21 WW	B7	-	2	2	2	-	2
CF-3 cast	52	C1	-	2	2	1	1	2
CF-8 cast	59	C2	-	2	2	2	-	2
CF-3 cast	69	C3	-	-	2	1	-	1
CF-8 cast	68	C4	-	-	2	2	-	2
304 SA	C1	A1	1	-	2	1	1	2
304 SA	C9	A2	1	-	2	1	1	2
304 SA	C12	A3	1	-	2	1	1	2
304 CW	C1 CW	A4	1	-	2	1	1	2
304 CW	C12 CW	A5	1	-	2	1	1	2
304 GBE	304 GBE	A6	1	-	2	1	1	2
316 GBE	316 GBE	B8	1	-	2	1	1	2
690 GBE	690 GBE	E1	1	-	2	1	1	2
304 BASE	304 BASE	A7	1	-	2	1	1	2
316 BASE	316 BASE	B9	1	-	2	2	-	2
690 BASE	690 BASE	E2	1	-	2	2	-	2
HP 304L SA	945	A8	1	-	2	1	1	2
HP 304L SA	1327	A9	1	-	2	2	2	2
304L SA	C3	A10	1	-	-	-	-	-
304L CW	C3 CW	A11	1	-	2	1	1	2
304-like alloy	L5	A12	1	-	2	1	1	2
Total			24	24	56	34	23	53

[a] SA = solution annealed; CW = cold worked at room temperature; WW = warm worked at 400°C; GBE = grain boundary engineered; BASE = base heat for GBE modification; HP = high purity.
[b] Doses are target dose; the actual doses are given in Table 18.

4.3 Experiment Preparations

4.3.1 SSRT Test

The SSRT tests on BOR-60 specimens will be conducted in the test facility described in Section 3.1.3.1. The water loop of the test facility will be reconditioned to circulate simulated PWR water at 320°C (608°F) and at a system pressure of ≈12.4 MPa (≈1800 psig). Because of the small size of the BOR-60 tensile specimens, installing the irradiated specimen by remote means requires extreme caution. To avoid bending or twisting of the specimens, a sample grip system has been designed for installing the specimens (Fig. 35). Two guiding rods maintain alignment between the top and bottom grip, and the

Table 18. Displacement damage dose for specimens irradiated in Boris 6 irradiation cycle.

Specimen Type	Capsule ID / Bundle ID	Specimen IDs	Dose (dpa)
TEM	AN 05	-	5.5
	AN 10	-	10.2
	AN 20	-	24.5
	HE 10	-	11.8
Tensile	D1-1/B3-1	D1-1, D2-1, D2-2, B3-1	5.5
	A5-1/E1-1	A5-1, A6-1, B8-1, E1-1	5.5
	B4-1/B6-2	B4-1, B5-1, B6-1, B6-2	5.5
	A7-1/A8-1	A7-1, B9-1, E2-1, A8-1	4.8
	A1-1/A4-1	A1-1, A2-1, A3-1, A4-1	4.8
	A9-1/A12-1	A9-1, A10-1, A11-1, A12-1	4.8
	D1-2/D2-4	D1-2, D1-3, D2-3, D2-4	10.2
	B1-1/B2-2	B1-1, B1-2, B2-1, B2-2	10.2
	B3-2/B4-3	B3-2, B3-3, B4-2, B4-3	11.8
	B5-2/B6-3	B5-2, B5-3, B5-4, B6-3	11.8
	B6-4/B7-2	B6-4, B6-5, B7-1, B7-2	10.4
	C1-1/C2-2	C1-1, C1-2, C2-1, C2-2	10.4

specimen is centered between two loading pins. After two cover clips are tightened, the specimen can only be loaded in tension and is protected from bending or twisting.

Another issue associated with the small size of the BOR-60 SSRT specimens is the high load generated by the system pressure. For the system pressure required for the PWR environment, the pull rods [6.35-mm (0.25-in.) dia] that are currently being used for the Halden specimens would result in a tensile stress in excess of the yield stress of the material. To avoid the premature loading of the specimen during heating and pressurization, smaller pull rods [3.175-mm (0.125-in.) dia] have to be used. The smaller pull rods, matching flanges, and seals have been made and tested at the PWR temperature and pressure conditions.

4.3.2 TEM Installation and Sample Preparation

A transmission electron microscope (JEOL 100CX) has been designated for the microstructural work on irradiated materials (Fig. 36). The electron microscope has been relocated in a controlled-area laboratory equipped to handle radioactive materials and has been set up to proper working condition. Nonirradiated specimens have been examined with this electron microscope, and regular maintenance and calibration have been completed after reinstallation.

Preparation of TEM samples from irradiated materials imposes another challenge for the microstructural work in this task. The radioactive exposure of the BOR-60 TEM disks is ≈200 mR/hr on contact, and loose contamination will be inevitable during sample preparation. To minimize the radiation exposure and to contain the loose contamination, a proper procedure for TEM sample preparation has to be developed. Mock-up polishing on nonirradiated TEM disks has been conducted with a single-jet polisher (shown in Fig. 37) with perchloric acid solution. The polishing conditions of -20°C (-4°F), 100 V, and 30 mA were found to yield the best results for SSs specimens. The same condition is expected to be appropriate for irradiated specimens.

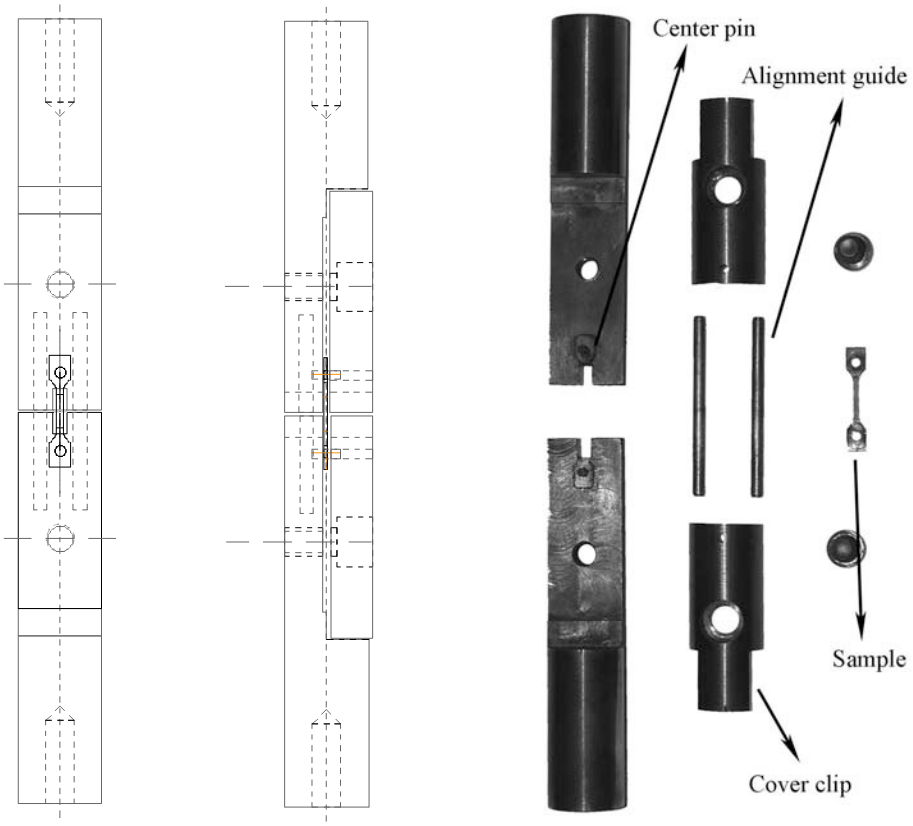

Figure 35. SSRT sample grips for BOR-60 tensile specimen.

Figure 36.
Reinstalled TEM designated for microstructure work on irradiated materials.

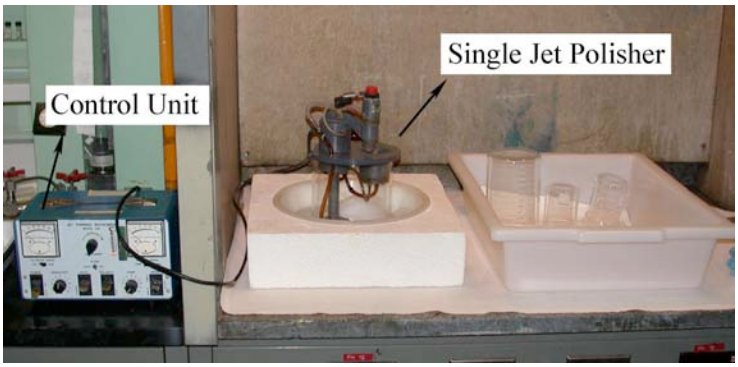

Figure 37. Single-jet polisher used for TEM sample preparation.

4.4 Ball Punch Test (Y. Chen and W. K. Soppet)

To explore the possibility of using 3-mm (0.118 in.) TEM disk samples from the BOR-60 irradiations to generate mechanical property data, various small-specimen-testing techniques were reviewed. Special attention was given to the possibility of extracting fracture toughness information from miniature disk samples. The selected test method will be used to investigate neutron irradiation embrittlement of core internal materials at PWR-relevant dose and temperature.

4.4.1 Available Miniature Test Methods for Disk Specimens

Mechanical testing on miniature specimens has been an active area in nuclear materials research. The space limitation in irradiation facilities and the potential reduction in sample radioactivity are the main reasons behind the development of miniature testing techniques. Several "punch" tests and instrumented micro-indentation tests have been developed by various entities for the purpose of extracting mechanical properties from miniature disk or coupon specimens. The basic procedure of punch tests is to drive a small indenter into a flat sample mounted on a die, while load-displacement is recorded for the process. In these tests, specimens are bent or locally sheared under the punch head, and the load-displacement curve can be used to analyze the strength or ductility of the material. Unlike the punch test, only the surface of the specimen is plastically deformed in a micro-indentation test. The penetration of the indenter is used to analyze the flow behavior of the specimen in a micro-indentation test.

4.4.1.1 Small Punch Tests

Based on punch head geometry, small punch tests can be classified into two groups. One is called "shear punch test," which uses a flat punch head; another is called the "ball punch test," which uses a ball or hemispherical punch head.

(1) Shear Punch Test

In the shear punch test, a disk specimen is sheared by driving a flat-head pin into the specimen while it is clamped between upper and lower dies.[103-105] The clearance between the punch pin and receiving die is small, so the deformation of specimen is confined in a very narrow annular region around the cylindrical punch pin. It is reasonable to assume that only shear stress is developed in the specimen during this test. An "effective" shear stress can, therefore, be related to load (P) on the punch pin as:

$$\tau = \frac{P}{2\pi rt} \tag{35}$$

where t is the specimen thickness, and r is the average of the punch pin and receiving die radii.[106,107]

Because the deformation state in the shear region is highly complex, it is difficult to analytically correlate a shear-punch load-displacement curve with uniaxial tensile properties. However, the effective shear stress where the load-displacement curve starts to deviate from its initial linearity has been linearly correlated to the uniaxial tensile yield strength for various materials.[107] In addition, the maximum effective stress and the total displacement in a shear punch curve have also been linearly related to the ultimate tensile strength and total ductility in uniaxial tensile tests, respectively.[108] Using the effective shear stress to compute the strain-hardening exponent (n_τ), a linear correlation has also been found between n_τ and the uniform elongation obtained from the tensile test.[106]

(2) Ball Punch Test

A spherical or hemispherical punch head is used in ball punch tests. Depending on how the disk sample is mounted on the receiving die, two types of ball punch tests have been developed. One test is commonly referred to as the "disk bend" test, in which the sample is simply supported on the shoulder of the receiving die. The rim of the sample can move freely when the punch head is driven into the receiving die.[109,110] The other test is referred to as the "bulge" test, in which the sample is clamped between upper and lower dies.[111,112] The bulge test will be our focus of discussion below.

The deformation in a bulge test is a combination of bending and membrane stretching. The stress state at the center of the bulge is approximately balanced, biaxial tension. The load-displacement curve of a bulge ball-punch test can be roughly divided into three overlapped stages, which are dominated by the following deformation processes: (1) initial elastic plus local plastic deformation, (2) plastic bending, and (3) membrane stretching.[112] The maximum load is associated with the local thinning or the onset of plastic instability in the disk sample. Empirical correlations can be found between the plastic bending load and the uniaxial yield stress, and between the maximum load and the uniaxial tensile strength.

4.4.1.2 Instrumented Micro-indentation Test

The instrumented micro-indentation test, also known as the automated-ball-indentation (ABI) test, is similar to a micro-hardness test using a spherical indenter. Because it is a relatively simple and standard technique, the ABI testing device is commercially available. The ABI test is often used on bulk samples, but in principle, it can be used on disk-like specimens, as long as the sample thickness exceeds the minimum requirement imposed by the standard micro-hardness test.

The load and penetration depth are measured simultaneously during an ABI test. An unloading process is needed to obtain the pure plastic deformation. The indentation parameters are related to the true stress and strain through the following semi-empirical equations:[113,114]

$$\sigma_{true} = \frac{P_{mean}}{\delta}, \tag{36a}$$

$$P_{mean} = \frac{4P}{\pi d_t^{\,2}}, \tag{36b}$$

$$\delta = 1.12 \qquad \phi \le 1$$
$$\delta = 1.12 + 0.53\ln(\phi) \qquad 1 < \phi \le 27$$
$$\delta = 2.80 \qquad \phi > 27, \tag{36c}$$

$$\phi = \frac{\varepsilon_{plastic} E}{0.43\sigma_{true}}, \tag{36d}$$

$$d_t = 2\sqrt{Dh_t - h_t^2}, \tag{36e}$$

$$d_p = 2\sqrt{Dh_p - h_p^2}, \tag{36f}$$

$$\varepsilon_{plastic} = 0.2\frac{d_p}{D}, \tag{36g}$$

where P is the load; E is the Young's modulus; D is the indenter diameter; d_t and d_p are the indentation diameters with and without load, respectively; h_t and h_p are the measured penetration depths with and without load, respectively; and δ is a parameter related to the constraint effect for plastic deformation. By cyclically penetrating the sample over a certain load interval, a series of points can be generated to complete a stress-strain curve similar to the uniaxial tensile curve.[115]

4.4.1.3 Determination of Fracture Properties from Punch and Micro-indentation Tests

Among the three miniature test methods discussed above, two of them (ball punch test and instrumented micro-indentation test) have been used to extract fracture toughness information. We could find no literature on using the shear punch test to obtain fracture information, although fairly consistent strength and ductility information can be gathered from this test.

(1) Extracting Fracture Information Based on Ball Punch (Bulge) Test

The biaxial stress state in a bulge test is used for estimating fracture toughness. For ductile materials, Bayoumi et al. proposed a semi-empirical relation between fracture toughness (J_{Ic}) and fracture strain (ε_f) for AISI 1045 steel:[116]

$$J_{Ic} = k\varepsilon_f - J_0, \tag{37}$$

where J_0 and k are determined empirically. A linear correlation was found between the fracture strain measured by the ball punch test beyond a certain bulge ductility and the fracture toughness. Later, Mao et al.[112] demonstrated that this linear correlation exists for a wider range of ductile materials, and that J_0 and k may be material independent parameters. For brittle materials, Mao et al.[117] suggested a correlation between stress intensity factor K_{Ic} and ball punch fracture stress (σ_f):

$$K_{Ic} = C\sigma_f^{2/3}, \tag{38}$$

where *C* is a constant. Their proposed relation is supported by some ball punch tests on ceramic materials.

More recently, Foulds et al.[118] suggested another method to extract fracture toughness from ball punch (bulge) tests using the continuum toughness concept. The basic idea of this method is illustrated by a flow chart (Fig. 38) originally from Ref. 118. The main advantage of this method is its analytic approach to computing fracture toughness. Empiricism is only needed for interpreting the punch test for a fracture criterion. In Foulds et al.,[118] the estimated K_{Ic} and the value measured by the ASTM standard method differ by less than 25%.[119]

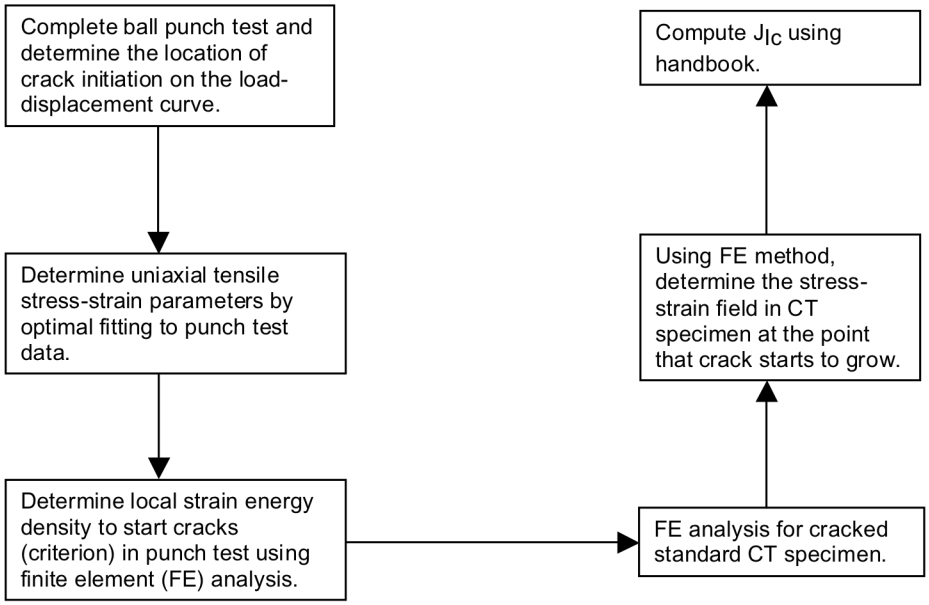

Figure 38. Flow chart for the method proposed by Foulds et al. [Ref. 118].

(2) Extracting Fracture Information Based on Micro-indentation Test

Since no cracking is introduced in a tested sample under compression, the use of the micro-indentation test to obtain fracture toughness information heavily relies on the following assumption: an "imaginary fracture" occurs during an indentation test when the maximum indentation pressure is equal to the critical cleavage fracture stress. This assumption is based on the fact that material at the center of the contact surface underneath the indenter experiences a degree of constraint similar to that experienced by materials in front of the crack tip.[113] So, the energy absorbed per unit area (compressive force) up to the critical fracture stress can be used to represent the fracture energy. The indentation energy to fracture (IEF) is given as:

$$\mathrm{IEF} = \frac{S}{\pi} \ln\left[\frac{D}{D - h_f}\right], \tag{39}$$

where S is the slope of the load-displacement curve, and h_f is the indentation depth at which the stress exceeds the critical fracture stress (σ_f). From knowledge of the energy to fracture the sample, the crack size (a) can be calculated by the Griffth theory:

$$\sigma_f = \left(2EW_f / \pi a\right)^{1/2}, \tag{40}$$

where W_f is the fracture energy. So, the static fracture toughness can be computed by:

$$K_{Ic} = \sigma_f \left(\pi a\right)^{1/2}. \tag{41}$$

4.4.1.4 Conclusion on Test Method Selection

(1) Shear Punch

The shear punch test can provide both ductility and strength information of disk samples. The correlations between shear punch results and uniaxial tensile properties are well established. It is likely that the testing results with this method will be more consistent than the other methods. Meanwhile, since the whole volume of material inside the clearance of the punch head and die is sampled in the test, neither sample size effect nor microstructure inhomogeneities are a problem.

The main disadvantage of the shear punch is its complex stress state. It is very difficult to establish any correlation between the shear punch result and other mechanical property in an analytical way which is useful for any fundamental study. Another disadvantage of shear punch test is that no correlation has been found between the shear punch result and fracture toughness.

(2) Ball Punch (bulge)

Similar to the shear punch test, a large amount of material is examined during a ball punch test; therefore, it is not sensitive to any microstructure inhomogeneity either. Further, the stress state in a bulge test is not as complex as that in a shear punch test, making some degree of analytical description possible. The most attractive aspect of the ball punch test is its potential to derive fracture toughness information. In fact, most of published researches that attempted to extract fracture information from miniature disk specimens involved this test.

The problem with the ball punch test is the sample size and thickness effects. As a result, the load-displacement curve of a ball punch test may not be as consistent as that in a shear punch test. In addition, if a ductile material is tested, a large friction load is expected because of the larger contact surface area between the punch ball and sample surface. Clamping the sample prior to the punch test may also cause sample preloading and, therefore, affect the measurement accuracy.

(3) Instrumented Micro-indentation

The most often cited advantage of the micro-indentation test is its simplicity. A semi-empirical correlation is available to describe the load-displacement behavior in this test. The method to extract tensile properties from this test is standard and easily available. It is also possible to obtain fracture toughness information, although it relies on a somewhat questionable assumption.

The main problem for using the micro-indentation test on TEM disks is its restriction on penetration depth, which, in turn, imposes limitations on sample thickness and indenter size. Shinohara et al.[120] suggested that the thickness of the TEM disk should not be less than 0.5 mm (0.02 in.). The indenter size should also be very small for the 3-mm (0.118-in.) TEM disk. Based on the same restriction in penetration depth, the measurable plastic strain by this method is also limited.

In summary, among the three methods discussed above, the instrumented micro-indentation test is the easiest one to implement because of its commercial availability, but the ball punch (bulge) test holds the most promise of providing meaningful information on fracture toughness, in addition to tensile properties.

4.4.2. Ball Punch Test Description and Preliminary Results

On the basis of the literature review, the ball punch test was selected for extracting mechanical property data from the 3-mm (0.118-in.) TEM disks irradiated in the BOR-60 reactor. A tabletop screw-driven test frame, which is small enough to fit inside a glove box for testing irradiated specimen, is used for this test. The test system includes a computer driven stepmotor, a 4.45 kN (1000 lb) load cell, and two linear variable displacement transducers (LVDTs). Figure 39 shows the design of the ball punch test fixture. A 1-mm (0.039-in.) tungsten carbide ball is used to punch the disk sample, and the load and displacement are recorded during the test.

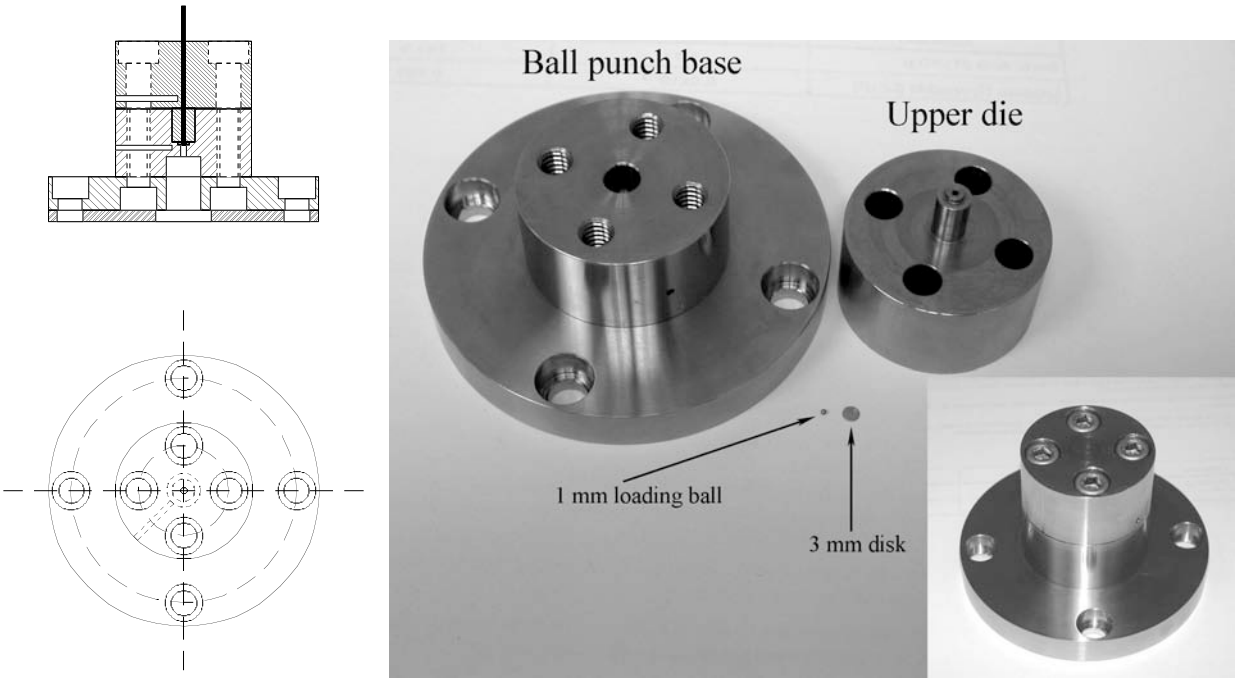

Figure 39. Ball punch test fixture for 3-mm TEM disk samples.

The ball punch system has been tested with nonirradiated specimens. Austenitic SS disks with a uniform thickness of 0.25 mm (9.8 mil) were tested with a constant cross-head speed of 0.46 mm/min (0.018 in./min). The load-displacement curve was recorded for each test, and the specimen was unloaded after a significant load drop had occurred. The reproducibility of the current ball punch system is satisfactory, as shown in Fig. 40. The unloaded disks were examined by SEM, and circumferential cracks, shown in Fig. 41, were observed in all tested samples.

To detect the early development of cracking, interruption ball punch tests were conducted. The disk sample was unloaded after a small load increment, then the deformed disk surface was examined by SEM. After SEM observation, the deformed disk was reloaded, and the ball punch test was continued. Figure 42 shows an interruption ball punch test on a 0.25-mm (9.8-mil) thick SS disk. The whole test was interrupted five times before the final load drop. The observed load-displacement segments were

reconstructed and compared with the results from an uninterrupted test on an identical disk (dashed line). The results for the interrupted ball punch test show good agreement with those for the continuous test. Small cracks were detected after the fourth unloading.

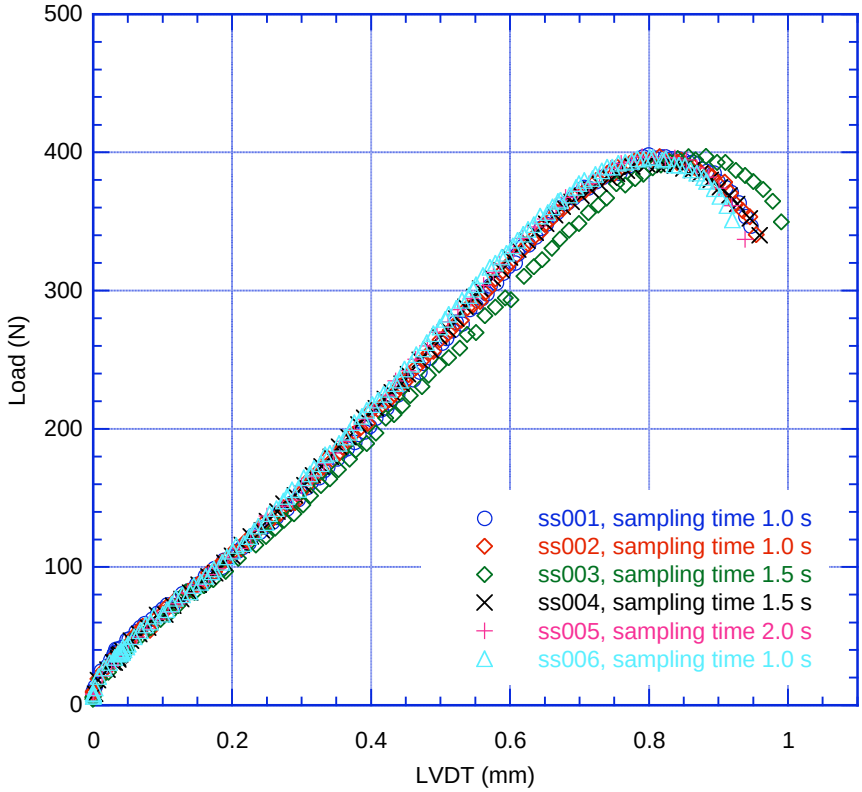

Figure 40. Ball punch tests on 0.25-mm-thick austenitic stainless steel disks.

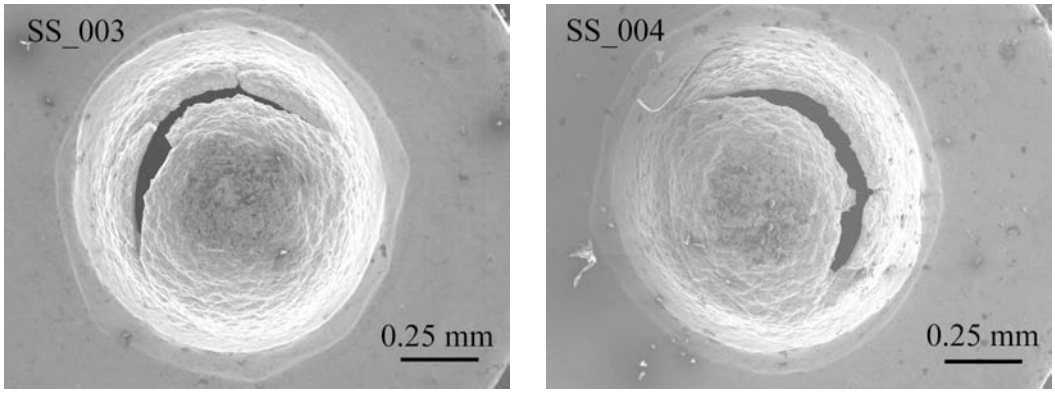

Figure 41. Circumferential cracks developed at the end of ball punch tests.

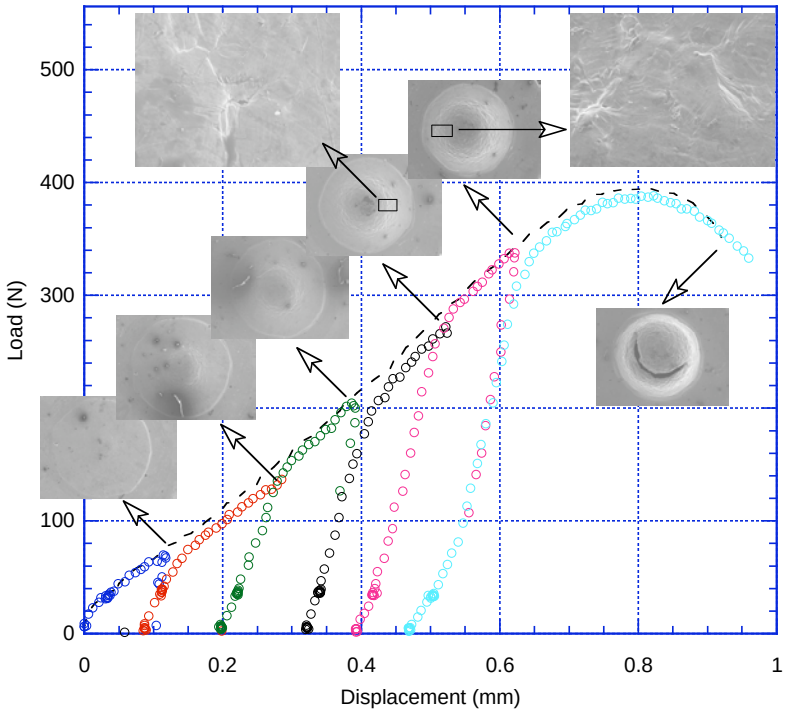

Figure 42. Interruption ball punch test on a 0.25-mm-thick stainless steel disk.

4.5 Influence of Neutron Flux on IASCC Behavior (Y. Chen and W. K. Soppet)

Irradiation-assisted stress corrosion cracking is not only a function of neutron fluence but also flux. The damage rate and helium production, which contribute to the IASCC susceptibility, can differ with different neutron fluxes. Because of this potential flux effect, we are comparing SSRT results of common materials from both Halden and BOR-60 irradiations at similar doses. To isolate the flux effect, the comparison should be made with SSRT tests in a similar environment. By considering the availability of irradiated specimens in both Halden and BOR-60 irradiations, SSRT tests are planned in either high DO water or PWR water environments. Table 19 shows the heats that are common in both Halden and BOR-60 irradiations, and the SSRT tests planned to study the flux effect.

Table 19. Common heats in both Halden (phase I and II) and BOR-60 irradiations and planned SSRT tests (tentative).

Heat ID	Description	Dose for Halden Specimen (dpa)	Dose for BOR-60 Specimen (dpa)	Planned Test Env. (tentative)
C1	304 SS, SA, low S	3.0	4.8	PWR
C3	304 SS, SA	3.0	4.8	PWR
C9	304 SS, SA, high S	3.0	4.8	PWR
C12	304 SS, SA, low S	3.0	4.8	PWR
C21	316 SS, SA	3.0	5.5	PWR
623	316 LN, SA	2.44	5.5	High-DO
625	316 LN, SA, Ti-doped	2.44	5.5	High-DO
327	High purity 304L, SA, low O	2.44	4.8	High-DO
945	High purity 304L, SA, high O	2.44	4.8	High-DO

By the end of 2005, SSRT tests were completed in high-DO water on two high-purity Type 304L SSs, heats 327 and 945. Figure 43 shows these SSRT results, which will be compared with BOR-60 results in the future. Both materials show a significant load drop immediately after yield. It is not clear at present whether or not this load drop is associated with cracking. SEM examination on the fracture surface is in progress to determine the IASCC susceptibility of these materials by measuring their fraction of IG fracture.

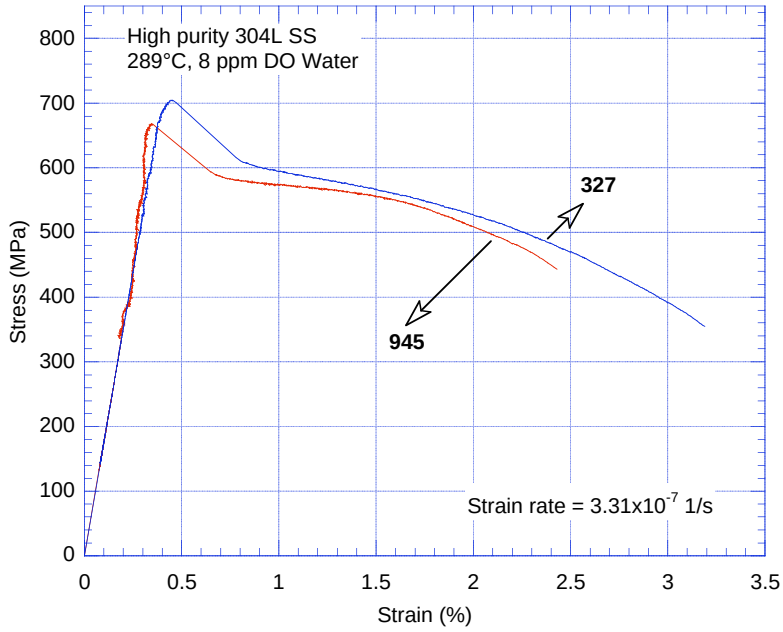

Figure 43. SSRT results on Halden specimens (heats 327 and 945) to be compared with BOR-60 specimens.

4.6 Assessment of Void Swelling in Austenitic Stainless Steel Core Internals (H. M. Chung)

As many PWRs age and life extension of the aged plants is considered, void swelling of austenitic SS core internals has become a subject of increasing attention. Excessive void swelling can lead to dimensional instability of the component and significant degradation of fracture toughness. It can also influence or contribute to the susceptibility of the component to IASCC, stress relaxation, or irradiation embrittlement.

Because of experimental problems largely related to the salvaging and handling of large, highly irradiated reactor components, it is either very difficult or impractical to obtain directly applicable void swelling data from actual PWR internals that have reached an EOL condition. An indirect method commonly used is to extrapolate more abundant data obtained under liquid metal, fast breeder reactor (LMFBR) conditions to PWR EOL or life-extension conditions. Many uncertainties are involved in this extrapolation, and its outcome is often considered either unconvincing or questionable. Even for a given irradiation temperature and given steel, the integral effects of dose and dose rate on void swelling cannot be separated. It is incorrect to extrapolate swelling data on the basis of "progressive compounded multiplication" of separate effects of factors such as dose, dose rate, temperature, and material composition.

Compared to LMFBRs, the neutrons resulting from fission in LWRs are moderated and slowed, or "thermalized," resulting in a higher probability of their capture by surrounding materials. As these thermal neutrons bombard the structural materials that support the fuel and reactor core components, the atoms of the material are displaced, often much more than once, resulting in large numbers of vacancies and interstitials, with important consequences for the strength and the resistance to failure of these materials. Simultaneous with the bombardment and consequent damage, the moderately high temperatures of the core internal materials [≈338°C (≈640°F)] produce an offsetting process that entails annealing and consolidation of the radiation damage into voids, dislocation loops, and other microscopically faulted structures.* In addition, many of the point defects formed through neutron bombardment simply diffuse to sinks of various types, including external surfaces, grain boundaries, or interphase surfaces. If the temperatures are high [≈400 to 560°C ≈752 to 1040°F)] and the irradiation damage extensive (>10^{23} n/cm^2 with E>0.1 MeV), the voids that are formed could conceivably produce dimensional changes, resulting in misfitting of the components, increases in stress, and other unacceptable consequences.

The data from investigations related to LMFBR performance indicate that void swelling is divided into two phases - incubation, followed by void formation. Once voids have started to form, a general rule of thumb is that swelling proceeds at a rate of 1% per dpa accumulated. However, the incubation period is influenced by a number of important variables, including cold work, which tends to extend the period of incubation, and metal chemistry, which can either extend or foreshorten the incubation period. Because cold work extends the onset of swelling, core baffle bolts are frequently fabricated from 20% cold-worked (CW) Type 316 SS.

The available database on void swelling and density change of austenitic SSs has been critically reviewed. Irradiation conditions, test procedures, and microstructural characteristics were carefully examined, and key factors that are important to determine the relevance of the database to PWR conditions were evaluated.

Limited swelling data are available for CW Type 316 SS irradiated to 53 dpa at 376-386°C (709-727°F) and for SA Type 304 SS irradiated to 50 dpa at ≈370°C (≈698°F) in EBR-II reflector positions at dose rates comparable to those of PWR reentrant corners. As such, these data are relevant to the conditions of PWR reentrant corners. Swelling in these materials was less than 1%.

The low degree of void swelling observed in PWR components and in EBR-II steels under PWR-relevant dose rates appears to be associated with irradiation-induced formation of very fine precipitates (such as G phase, carbides, and γ' phase) in high number density. Such irradiation-induced precipitation at low temperatures [<370°C <698°F)] creates an extremely large internal surface (i.e., the interface between the steel matrix and the precipitates). This interface acts as an efficient sink to irradiation-induced vacancies, thereby suppressing the agglomeration of the vacancies. Irradiation-induced precipitation is sensitive to minor alloying and impurity elements, irradiation temperature, and dose rate.

The available void swelling data for PWR core internals[121-126] are plotted in Fig. 44 in terms of irradiation temperature and dose (dpa); a higher level of swelling is denoted with a larger circle and a darker color. Figure 45 shows a plot of void swelling of PWR internals as a function of dose. The maximum observed void swelling was 0.020-0.24% at ≈333-343°C (631-649°F) and 7.5-12.2 dpa for the

* Neutrons can also cause transmutation of some of the lighter elements such as boron, generally found in trace amounts in structural materials. However, the amounts of helium and possibly hydrogen that are produced by transmutation of light elements are not likely to contribute significantly to void formation. Thermal neutron bombardment of nickel can produce a few parts per million of helium during the course of a reactor lifetime, which could contribute to void production.

flux thimble tube and baffle bolts fabricated from CW Type 316 SS. No swelling larger than 0.25% was observed. This level of swelling is insignificant.

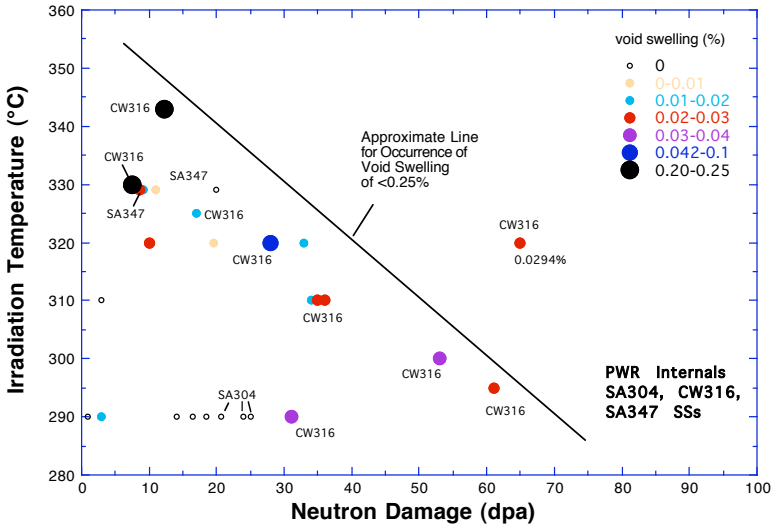

Figure 44. Range of irradiation temperature and dose for which void swelling data (in color code) have been reported for PWR core internals.

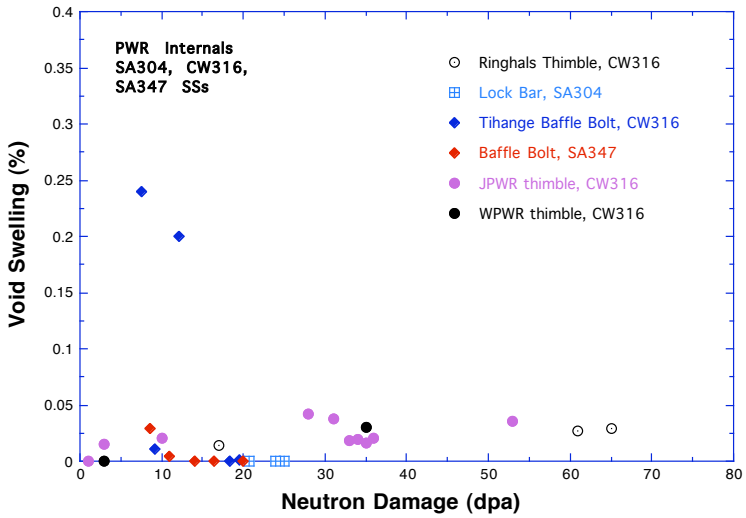

Figure 45. Void swelling of PWR internals plotted as a function of dose (dpa).

In thin-walled flux thimbles and instrument tubes, the effect of gamma heating is insignificant. The currently available database is sufficient to conclude that void swelling in this type of reactor internal, mostly fabricated from CW Type 316 SS, is not an issue.

Most PWR baffle bolts are fabricated from CW Type 316 SS. The data obtained from the industry baffle bolt program show that swelling is insignificant (<0.25%) for dose levels up to ≈20 dpa and irradiation temperatures up to ≈340°C (≈644°F). Data obtained on Experimental Breeder Reactor-II (EBR-II) components irradiated at temperatures <380°C (<716°F) and at comparable dose rates are consistent with the data from the industry bolt program. Microstructural characteristics of the two groups of materials are also consistent. Thus, void swelling in this type of reactor internal will not likely exceed

the threshold level (i.e., ≈4%) that is necessary to enter the regime of the steady-state swelling rate of 1%/dpa.

Most baffle reentrant corners are fabricated from SA Type 304 SS and are most susceptible to high swelling rates, and hence, high swelling at EOL. The maximum irradiation temperature in some regions of the reentrant corners has been estimated to be ≈380-420°C (≈716-788°F). Figure 46 shows the data from steels irradiated in EBR-II at 376-460°C (709-860°F); some data reported by Allen et al.[127] for CW Type 316 SS at 376-386°C (709-727°F) and by Chung et al.[128] for SA Type 304 SS at 370°C (698°F) are also included in the figure. The steel specimens were obtained from fuel subassemblies [1-mm-thick (0.039-in.) hex can] located in the reflector region of the reactor. In that location, the steels are irradiated at lower temperatures, and their dose rates are about one order of magnitude lower than that in the fueled region. As such, the data are more relevant to the behavior of a PWR reentrant corner than the data obtained from steels irradiated at higher temperatures in the core center.

The investigation on SA Type 304 SS showed that void swelling in this material after irradiation in EBR-II to ≈50 dpa at 370°C (698°F) and a dose rate comparable to that of reentrant corners was only 0.54%.[127] The low swelling appears to be related to high-density, irradiation-induced precipitation of very fine carbides. Therefore, it is considered unlikely that void swelling in reentrant corners will exceed the threshold level of ≈4%. As a consequence, the potential impact of void swelling on core flow and the structural functions of the PWR internals is believed to be negligible.

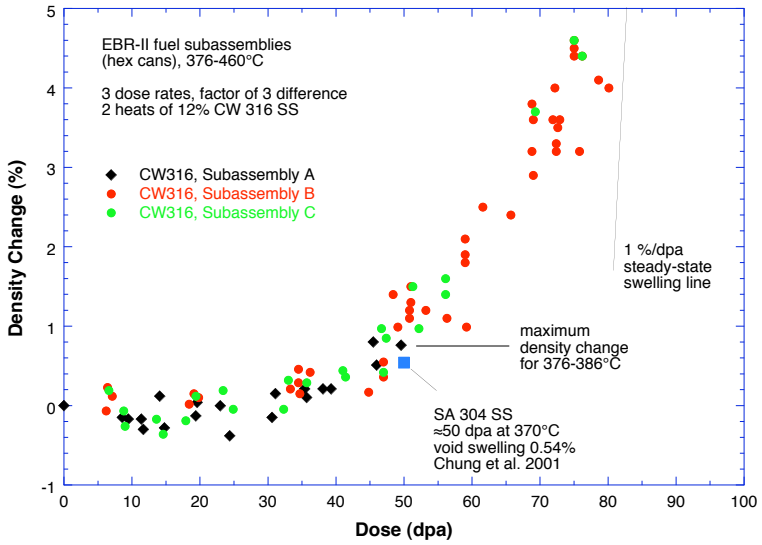

Figure 46. Density change in CW Type 316 SS fuel hex can irradiated in reflector region of EBR-II at 376-460°C to 5-80 dpa.

However, this estimation is only preliminary. More relevant swelling data, including the effects of dose rate and temperature, would be extremely helpful. Analyses to compute more accurate quantification of the maximum temperature at EOL and life-extension situations are needed for SA Type 304 and Type 316 SSs. A better mechanistic understanding of the roles of irradiation-induced microstructural evolution on void swelling is also needed. Several experimental programs to address these issues are underway and are expected to produce useful data in the next few years.

5 Cracking of Nickel Alloys and Welds (B. Alexandreanu, O. K. Chopra, and W. J. Shack)

5.1 Introduction

This part of the study consists primarily of establishing CGRs under constant and cyclic loading and evaluating Ni alloys and weld metals metallographically to develop comprehensive and statistically significant analyses that could be used to determine the dependence of the SCC of these materials on alloy composition, microstructure, water chemistry, temperature, and other factors.

The Ni-base alloys used as construction material in LWRs have experienced SCC. Primary-water SCC of Alloy 600 steam generator tubes in PWRs has been studied intensively.[129-131] Stress corrosion cracking has also occurred in Ni alloys used in applications such as instrument nozzles and heater thermal sleeves in the pressurizer[132] and penetrations for the control-rod drive mechanism (CRDM) in the reactor vessel closure heads.[133] In the fall of 1991, during an over-pressurization test, a leak was discovered in the pressure-vessel head penetration at the Bugey 3 plant in France. Metallurgical evaluations indicated that the leak was caused by primary-water SCC.[134] The main crack had initiated in Alloy 600 base metal and propagated into the Alloy 182 weld metal. Subsequent inspections of CRDM penetrations in domestic and foreign PWRs identified a small number of penetrations (<5% of the penetrations inspected) with axial cracks. None of the cracks was through-wall, and until about six years ago, no more leaks occurred in pressure-vessel head penetrations.

Leaks from axial through-wall cracks were identified at Oconee unit 1 in November 2000 and at Arkansas Nuclear One unit 1 in February 2001.[135] During the next 15 months, inspections at Oconee units 2 and 3 and followup inspection at unit 1 identified both axial and circumferential cracks in reactor-vessel head penetrations.[136] The presence of circumferential cracks, in particular, raised concerns regarding structural integrity.[137,138] Also, in October 2000, significant boron deposits were discovered near the Loop "A" reactor vessel nozzle to the hot-leg reactor coolant pipe weld at the V. C. Summer plant.[139] Ultrasonic inspection of the pipe revealed an axial crack and a short, intersecting circumferential crack in the dissimilar metal weld at the top of the pipe. Earlier in 2000, two shallow axial flaws were found in the outlet nozzle-to-safe-end weld of Ringhals unit 3, and four axial indications were found in the same region of Ringhals unit 4, in Sweden.[140] Cracks have also been found in pressure-vessel head penetrations at North Anna unit 2,[141] the Davis-Besse nuclear power plant,[142] and more recently, in the bottom-mounted instrumentation nozzles at South Texas unit 1.[143,144] Long-term operating experience indicates that, although wrought Ni-base Alloy 600 is susceptible to SCC, until recently, the weld metal Alloys 82 and 182 used with Alloy 600 were perceived to be less susceptible. However, laboratory tests indicate that in PWR coolant environments, the SCC susceptibility of Alloy 182 is greater than that of Alloy 600, and that of Alloy 82 is comparable to that of Alloy 600. The apparent inconsistency between field and laboratory experience is an issue that needs further investigation.

The objective of the experimental program being conducted at ANL is to evaluate the resistance of Ni alloys and their welds to environmentally assisted cracking in simulated LWR coolant environments. The present report is focused on the cracking behavior of laboratory-prepared Alloy 182 welds as a function of loading and sample orientation.

Crack growth tests were conducted on Alloy 182 specimens in a PWR environment. The approach was to precrack the samples in water and continue with loading cycles with increasing load ratios, R, and

increasing rise times to transition the fracture morphology from TG fatigue crack to IG SCC. Finally, the samples were set at constant load to determine SCC CGRs. This approach assured an optimal SCC engagement and a uniform crack front. The ANL approach is different from the commonly used practice in that precracking was conducted in water as opposed to air. An important advantage is that major experimental difficulties, such as incomplete IG fracture mode and finger-like crack growth, were never encountered in our program.

The resulting cyclic CGR in water for Alloy 182 was compared with the CGR in air for Alloy 600 obtained previously to determine the effect of the PWR environment. The effect of key parameters on both cyclic and constant load CGRs was determined earlier.[145-150] Correlations describing the fatigue CGRs of Alloys 600 and 690 as a function of the stress intensity factor range ΔK, load ratio R, and temperature were developed.[150] The results indicated that in air, the CGRs of these materials are relatively insensitive to changes in the test frequency. The CGR (da/dN in m/cycle) of Alloy 600 in air is best expressed as

$$da/dN = C_{A600} (1 - 0.82\ R)^{-2.2} (\Delta K)^{4.1}, \quad (42)$$

where ΔK is in MPa $m^{1/2}$, and the constant C_{A600} is given by a third-order polynomial of temperature T (°C) expressed as

$$C_{A600} = 4.835 \times 10^{-14} + (1.622 \times 10^{-16})T - (1.490 \times 10^{-18})T^2 + (4.355 \times 10^{-21})T^3. \quad (43)$$

In high-DO water, the CGRs of Alloy 600 showed frequency-dependent enhancement under cyclic loading conditions. Nevertheless, in high-DO water, the environmental enhancement of growth rates did not appear to depend strongly on the material condition. In contrast, environmental enhancement of CGRs of Alloy 600 in low-DO water seemed to be strongly dependent on material conditions. In the literature[151-163] such variability has been attributed to thermomechanically controlled parameters such as yield strength and grain boundary coverage of carbides, although the evidence for this dependence is more substantial for steam generator tubing than thicker structural materials.

In the earlier ANL work, correlations were also developed to estimate the enhancement of CGRs in LWR environments ($\dot{a}_{env,A600}$ in m/s) relative to the CGRs in air ($\dot{a}_{air,A600}$ in m/s) under the same loading conditions. The best-fit curve for Alloy 600, either in the SA condition or the SA plus thermally treated condition, in ≈300 ppb DO water is given by the expression[147]

$$\dot{a}_{env,A600} = \dot{a}_{air,A600} + 4.4 \times 10^{-7} (\dot{a}_{air,A600})^{0.33}. \quad (44)$$

Experimental CGR results indicated that some materials show little enhancement in PWR environments, while others show enhancement at 320°C (608°F) comparable to that predicted by Eq. 44. The SCC of Alloy 600 has been reviewed by Chopra et al.[150] and, more recently, by Alexandreanu et al.,[164] and the results indicated that frequency-dependent environmental enhancement is usually associated with susceptibility to SCC under constant loading conditions.

The effect of the stress intensity K on SCC crack growth for Ni-alloy welds in PWR environments has been represented by a modified[165] relationship between crack growth rate, $\dot{a}_{SCC,A182}$ (m/s), and stress intensity factor, K (MPa $m^{1/2}$), originally developed by Scott to describe CGRs in steam generator tubing. However, unlike the CGR relationship for Alloy 600,[166] the relationship for Ni-alloy welds has no threshold value for the stress intensity factor [in Alloy 600 the threshold is 9 MPa $m^{1/2}$ (8.2 ksi $in.^{1/2}$)],

$$\dot{a}_{SCC,A182} = A(K)^{1.6}. \quad (45)$$

The term A depends on the heat of the material and the temperature. The temperature dependence is usually assumed to follow Arrhenius behavior:

$$A = \alpha \exp\left[-\frac{Q}{R}\left(\frac{1}{T} - \frac{1}{T_{ref}}\right)\right], \quad (46)$$

where Q = activation energy for crack growth
= 130 kJ/mol (31.1 kcal/mol) for Ni-alloy welds
R = universal gas constant
= 8.314×10^{-3} kJ/mol·K (1.103×10^{-3} kcal/mol·°R)
T = absolute operating temperature in K (or °R)
T_{ref} = absolute reference temperature used to normalize the CGR data
= 598 K (1076.67°R)
α = 1.5×10^{-12} at 325°C (617°F).

This annual report presents CGR data for deep-groove and double-J Alloy 182 weld alloys in the PWR environment, and an additional Alloy 82 specimen from the V. C. Summer reactor nozzle-to-pipe weld. The results have been compared with the existing CGR data for Ni-alloy welds to determine the relative susceptibility of these materials to environmentally enhanced cracking under a variety of loading conditions.

5.2 Crack Growth Rates of Laboratory-Prepared Alloy 182 Welds in PWR Environment

Crack growth tests were conducted on laboratory-prepared Alloy 182 welds in a PWR environment at 320°C (608°F) under cyclic loading for a sawtooth waveform with rise times of 30-500 s and at constant load. The results are compared with the existing CGR data for Ni-alloy welds to determine the relative susceptibility of the laboratory-prepared Alloy 182 welds to PWSCC. A detailed metallographic examination of the test specimens was also performed to characterize the fracture morphology.

5.2.1 Experimental

5.2.1.1 Material and Specimen Geometry

Crack growth rate tests have been conducted on Alloy 182 weld metal samples in simulated PWR environments at 320°C (608°F) in accordance with ASTM Designation E 647, "Standard Test Method for Measurement of Fatigue Crack Growth Rates." The tests were performed on 1-T compact tension (CT) specimens; the configuration of the CT specimen is shown in Fig. 47. Crack extensions were determined by the reversed-current DC potential drop technique.

The 1-T CT specimens were machined from laboratory-prepared double-J weld (Fig. 48a) and deep-groove filled weld (Fig. 48b). The welds were prepared in accordance with the specifications of Section XI of the ASME Boiler and Pressure Vessel Code. The double-J weld was prepared by joining two 152 x 305 mm (6 x 12 in.) pieces of 38-mm-thick (1.5-in.-thick) plate (Heat NX1310). It was produced by 48 weld passes, where root passes 1-5 involved gas tungsten arc (GTA) welding with Alloy 82 filler/electrode, and the other passes, SMA welding with Alloy 182 filler. A schematic of the weld

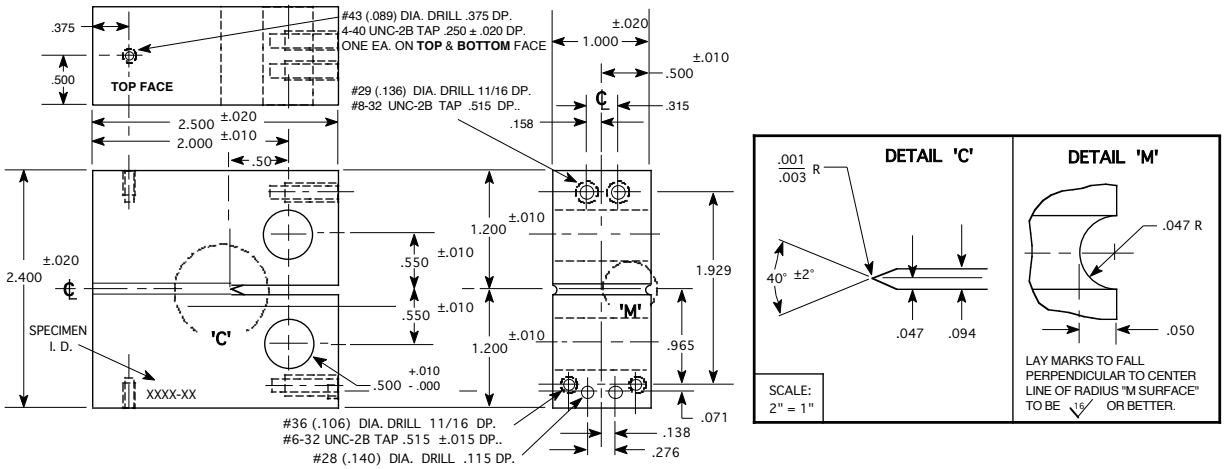

Figure 47. Configuration of compact-tension specimen used for this study (dimensions in inches).

design and various passes is shown in Fig. 48a, and the conditions for each weld pass are listed in Table 20. During welding the maximum inter-pass temperature was ≈120°C (250°F), and the weld surfaces were cleaned by wire brushing and grinding and were rinsed with de-mineralized water or alcohol. The deep-groove filled weld was prepared by using a 51-mm-thick (20-inch-thick) Alloy 600 plate (Heat NX1933) with a deep groove that was filled by several passes of SMA welding with Alloy 182 filler/electrode (size of 1/8 or 5/32 in.) (Fig. 48b). The chemical compositions of the base and weld metals are given in Table 21.

Table 20. Welding process and conditions for various weld passes for the J-groove weld.

Weld Pass	Process	Filler Metal	Filler/Electrode Size (in.)	Current (A)	Voltage (V)	Travel Speed (in./min)
1 - 5	GTA	Alloy 82	3/32	185 - 215	21 - 22	2 - 4
6 - 10	SMA	Alloy 182	3/32	140 - 155	24 - 26	6 - 7
11 -27	SMA	Alloy 182	1/8	155 - 170	25 - 27	6 - 7
28 - 48	SMA	Alloy 182	5/32	170 - 180	26 - 28	6 - 7

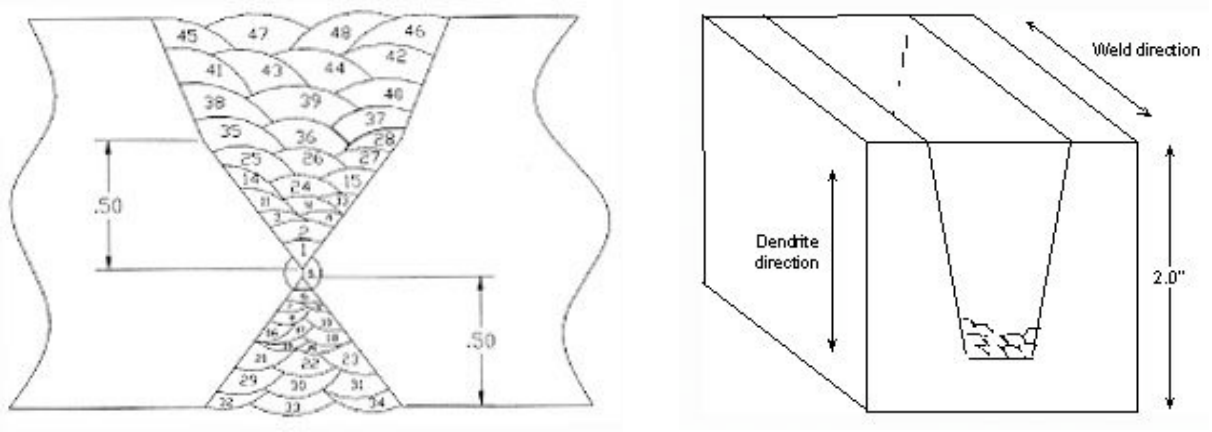

(a) (b)

Figure 48. Schematic of the weld joint design and weld passes for (a) Alloy 182 SMA double-J weld and (b) the deep-groove weld (dimensions are in inches).

Table 21. Chemical composition (wt.%) of Alloy 600 base metal and Inconel 182 and 82 weld metals.

Alloy ID (Heat)	Analysis	C	Mn	Fe	S	P	Si	Cu	Ni	Cr	Ti	Nb	Co
A 600 (NX1310)	Vendor	0.07	0.22	7.39	0.002	0.006	0.12	0.05	76.00	15.55	0.24	0.07	0.058
	ANL	0.07	0.22	7.73	0.001	-	0.18	0.06	75.34	-	-	-	-
A 600 (NX1933)	Vendor	0.08	0.26	9.55	0.003	-	0.15	0.10	73.31	15.90	-	-	-
A 182	Spec.	0.10*	5.0-9.5	6.0-10.0	0.015*	-	1.0*	0.5*	Bal	13.0-17.0	1.0*	1.0-2.5	0.12*
A 182 Double-J	ANL	0.04	6.58	6.48	0.005	0.022	0.33	0.04	70.62	14.34	0.36	1.13	0.03
A 182 Deep Groove	ANL	0.04	7.08	6.82	0.005	0.025	0.35	0.03	70.44	13.81	0.30	1.06	0.02
A 82	Spec.	0.10*	2.5-3.5	3.0*	0.015*	-	0.5*	0.5*	67.00*	18.0-22.0	0.75*	2.0-3.0	0.75*

*Maximum.

Two 1-T CT specimens were cut from the double-J SMA weld in the TS orientation,* as shown schematically in Fig. 49a. Three additional 1-T CT specimens, in TS, TL, and LS orientations, were prepared from a deep-groove Alloy 182 weld (Fig. 49b). All CT specimens were 25.4-mm (1-in.) thick (Fig. 47), except the deep-groove specimen in the LS orientation, which had to be thinned to a thickness of 19.4 mm (0.76 in.) to ensure that the entire crack front would be exclusively in the weld alloy.

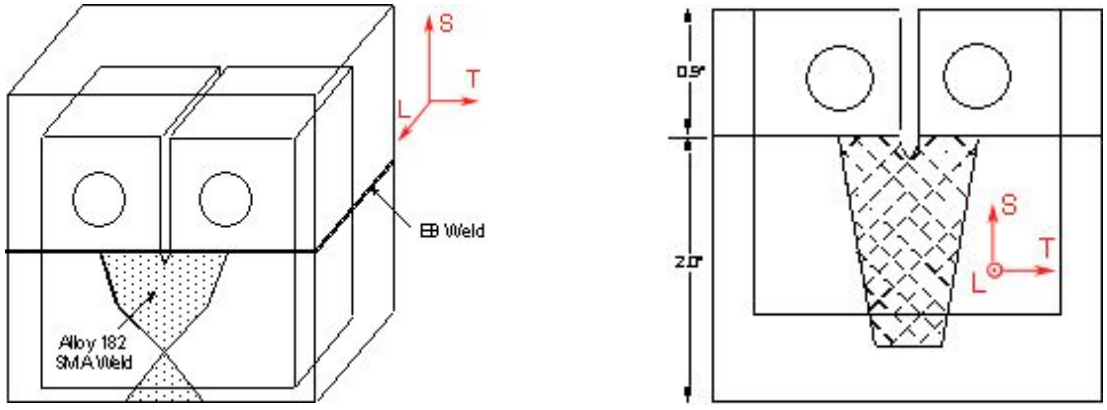

(a) (b)

Figure 49. Orientation of the CT specimens from (a) the Alloy 182 SMA double-J weld and (b) the deep-groove weld.

The metallography of the weld specimens was performed by means of SEM, energy dispersive x-ray spectroscopy (EDS), and orientation imaging microscopy (OIM). A complete description of the results is given in a topical report.[164]

5.2.1.2 Crack Growth Test Facility and Procedure

The facility for conducting the CGR tests consists of a 5.7-L SS autoclave with a recirculating water loop. The load frame, hydraulic actuator, autoclave, and the furnace are mounted on top of a portable wheeled cart. An Instron Model 8500+ control console is used to load the specimen. The PWR water is circulated from a 135-L SS storage tank through a high-pressure pump, regenerative heat exchanger, autoclave preheater, test autoclave, ECP cell and preheater, regenerative heat exchanger, and Mity Mite™ back-pressure regulator. This water is then returned to the storage tank. Water is circulated at flow rates of 15-40 mL/min. Also, water samples are taken periodically to measure pH, resistivity, and DO concentration in the feedwater. This facility is similar to the ANL facility used for in-cell testing of

*The first letter represents the direction normal to the fracture plane, and the second represents the direction of crack advance. The three directions are: T = transverse, L = longitudinal, and S = side.

irradiated materials and is described in detail elsewhere.[164] The PWR water consists of high-purity water containing ≈1000 ppm B, 2 ppm Li, <30 ppb DO, and ≈2 ppm dissolved hydrogen (≈23 cc/kg). The room-temperature pH is ≈6.4.

The CGR tests were performed in accordance with ASTM E-647, "Standard Test Method for Measurement of Fatigue Crack Growth Rates," and ASTM E-1681, "Standard Test Method for Determining a Threshold Stress Intensity Factor for Environment-Assisted Cracking of Metallic Materials under Constant Load."

All specimens were fatigue precracked in PWR water at load ratio R = 0.3, frequency of ≈0.5-2 Hz, and maximum stress intensity factor K_{max} of 19-21 MPa $m^{1/2}$ (17.3-19.3 ksi $in.^{1/2}$). After ≈0.3-mm (0.01-in.) extension, R was increased incrementally to 0.5, and the loading waveform changed to a slow/fast sawtooth with rise times of 30-500 s. Finally, the samples were set at constant load. In all tests, K_{max} was maintained approximately constant by periodic load shedding. After the test, the final crack size was marked by fatigue cycling at room temperature. The specimen was then fractured, and the final crack length was measured from metallographic examination of the fracture surface. The final crack length was measured from the photograph by the 9/8 averaging technique, in which nine measurements were taken across the width of the specimen at equal intervals, the two near-surface measurements were averaged, and the resultant value was averaged with the remaining seven measurements.

The experimental data were consistent with the screening criteria of Ref. 166. All specimens showed 100% engagement (i.e., crack extension occurred over the entire machine notch, and the crack front was relatively straight). Also, under environmentally enhanced conditions, fracture morphology was predominantly intergranular (90% or greater). The CGR during each test period was determined from the slope of the corrected crack-length-vs.-time plots. For cyclic loading, only the rise time was used to determine growth rate. The crack extension during each test period was at least 10 times the resolution of the DC potential drop method (i.e., typically 5 μm). Thus, crack extensions were at least 50 μm; for test conditions with very low CGRs (less than 1×10^{-11} m/s), smaller crack extensions were used to reduce testing time.

To ensure that the experimental data obtained from differing specimen geometry, thickness, and loading conditions can be compared with each other and applied to reactor components, the CGR data were validated in accordance with the specimen size criteria of ASTM E-1681 and E-647, as appropriate. For high-strain-hardening materials with ultimate-to-yield-stress ratio ≥1.3, both requirements allow the use of flow stress defined as $\sigma_f = (\sigma_{ult} + \sigma_{ys})/2$ rather than the yield stress.

5.2.2 Results

5.2.2.1 Crack Growth Rates in PWR Environment

Crack growth tests have been completed on one double-J (CT31-W02 TS) and three deep-groove (CT933-TS, CT933-TL, and CT933-LS) 1-T CT specimens. The test conditions and the resultant experimental CGRs are given in Tables 22-25. Complete test results, including plots of the change in crack length and K_{max} with time during various test periods, are presented in a topical report.[164] Micrographs of the fracture surfaces of the three specimens are shown in Figs. 50-53. The experimental approach used resulted in complete SCC engagement and uniform crack fronts. The actual crack extensions were a factor 1.6-2.6 larger than the values determined from the DC potential drop measurements. This difference was most likely due to the presence of unbroken ligaments on the fracture surface. One exception was specimen CT933-TL, where the correction was relatively small (6.2%), but

in this case the fracture propagated across the dendrites, and the crack extensions were small by comparison with those from the other three specimens. In all cases, the crack extensions estimated from the DC potential method were scaled proportionately; the corrected values of K_{max} and growth rate are given in Tables 22-25.

Table 22. Crack growth data for specimen CT31-W02 TS of Alloy 182 SMA weld in PWR water[a] at 320°C.

Test Period	Test Time (h)	ECP[b] (SHE) (mV)	O_2 Conc.[b] (ppb)	Load Ratio R	Rise Time (s)	Down Time (s)	Hold Time (s)	Kmax (MPa $m^{1/2}$)	ΔK (MPa $m^{1/2}$)	CGR_{env} (m/s)	Estimated CGR_{air} (m/s)	Crack Length (mm)
Pre a	129	-679	<10	0.3	1	1	0	23.7	16.6	1.83E-07	3.37E-08	13.928
Pre b	132	-679	<10	0.3	1	1	0	26.4	18.5	3.10E-07	2.62E-08	16.026
Pre c	136	-679	<10	0.3	1	1	0	29.7	20.8	4.55E-07	4.24E-08	18.356
Pre d	138	-679	<10	0.3	1	1	0	34.9	24.4	6.10E-07	8.24E-08	21.470
Pre e	141	-679	<10	0.3	1	1	0	43.3	30.3	7.48E-07	1.99E-07	25.274
1	339	-681	<10	0.5	12	2	0	28.8	14.4	2.08E-09	1.36E-09	25.872
2	359	-672	<10	0.5	12	2	0	29.9	15.0	6.91E-09	1.58E-09	26.417
3	599	-	<10	1.0	-	-	-	30.5	-	4.22E-10	-	26.708
4	812	-	<10	1.0	-	-	-	36.4	-	3.94E-10	-	27.097
5	1157	-	<10	1.0	-	-	-	49.5	-	7.29E-10	-	28.185

[a]Simulated PWR water with 2 ppm Li, 1100 ppm B, and 2 ppm dissolved hydrogen (≈23 cc/kg).
[b]Represents values in the effluent; ECP values are for Alloy 600 electrode; conductivity was ≈22 μS/cm in the effluent.

Table 23. Crack growth data for specimen CT933-TS of Alloy 182 SMA weld in PWR water[a] at 320°C.

Test Period	Test Time (h)	Conduc-tivity[b] (μS/cm)	O_2 Conc.[b] (ppb)	R Load Ratio	Rise Time (s)	Down Time (s)	Hold Time (s)	Kmax (MPa $m^{1/2}$)	ΔK (MPa $m^{1/2}$)	CGR (m/s)	Estimated CGR_{air} (m/s)	Crack Length (mm)
Pre a	30	25.0	<10	0.3	1	1	0	23.2	16.2	2.07E-09	1.54E-08	12.609
Pre b	40	25.0	<10	0.3	10	10	0	23.3	16.3	5.80E-09	1.58E-09	12.708
1a	70	25.0	<10	0.3	10	10	0	23.9	16.7	1.05E-08	1.74E-09	13.148
1b	90	25.3	<10	0.3	10	10	0	24.6	17.2	1.47E-08	1.96E-09	13.686
2	142	25.3	<10	0.6	10	10	0	25.3	10.1	1.88E-09	5.29E-10	13.889
3	243	25.3	<10	0.7	10	10	0	25.9	7.8	6.97E-10	2.64E-10	14.027
4	506		<10	0.7	100	100	0	25.7	7.7	2.43E-10	2.57E-11	14.234
5	704		<10	0.7	300	12	0	28.5	8.5	1.18E-10	1.30E-11	14.313
6	964		<10	0.7	300	12	3600	28.6	8.6	1.15E-10	1.32E-11	14.428
7	1132		<10	1.0	-	-	-	28.7	0.0	1.05E-10	-	14.491
8	1373		<10	0.5	30	4	0	32.6	16.3	2.66E-09	8.99E-10	16.568
9	1467		<10	0.5	300	4	0	33.3	16.7	1.37E-09	9.85E-11	16.990
10			<10	1.0	-	-	-	36.9	0.0	2.53E-10	-	17.753

[a]Simulated PWR water with 2 ppm Li, 1100 ppm B, and 2 ppm dissolved hydrogen (≈23 cc/kg).
[b]Represents values in the effluent.

Table 24. Crack growth data for specimen CT933-LS of Alloy 82 SMA weld in PWR water[a] at 320°C.

Test Period	Test Time (h)	Cond.[b] (μS/cm)	O_2 Conc.[b] (ppb)	Load Ratio R	Rise Time (s)	Down Time (s)	Hold Time (s)	Kmax (MPa $m^{1/2}$)	ΔK (MPa $m^{1/2}$)	CGR_{env} (m/s)	Estimated CGR_{air} (m/s)	Crack Length (mm)
Pre a	79	26	<10	0.30	0.5	0.5	0	23.7	16.6	1.63E-08	3.42E-08	13.306
Pre b	91	26	<10	0.30	5	5	0	25.9	18.1	7.87E-08	4.87E-09	15.051
Pre c	97	26	<10	0.30	5	5	0	28.5	19.9	1.28E-07	7.22E-09	16.952
1	162	26	<10	0.50	50	2	0	27.7	13.8	3.69E-09	2.77E-10	17.816
2	217	26	<10	0.50	500	12	0	27.9	14.0	7.63E-10	2.88E-11	18.007
3	836	26	<10	1.00	-	-	-	28.7	0.0	1.73E-10	-	18.373
4	1665	26	<10	1.00	-	-	-	44.8	0.0	6.54E-10	-	20.338
5	1690	26	<10	0.5	500	12	0	46.7	23.3	3.69E-09	2.36E-10	21.212

[a]Simulated PWR water with 2 ppm Li, 1100 ppm B, and 2 ppm dissolved hydrogen (≈23 cc/kg).
[b]Represents values in the effluent.

Table 25. Crack growth data for specimen CT933-TL of Alloy 182 SMA weld in PWR water[a] at 320°C.

Test Period	Test Time (h)	Cond.[b] (µS/cm)	O_2 Conc.[b] (ppb)	Load Ratio R	Rise Time (s)	Down Time (s)	Hold Time (s)	Kmax (MPa $m^{1/2}$)	ΔK (MPa $m^{1/2}$)	CGR_{env} (m/s)	Estimated CGR_{air} (m/s)	Crack Length (mm)
Pre a	73	22	<10	0.3	0.5	0.5	0	21.2	14.8	1.12E-08	1.07E-08	12.791
Pre b	96	22	<10	0.3	0.5	0.5	0	21.4	15.0	1.25E-08	2.22E-08	12.945
1	191	22	<10	0.5	300	12	0	21.6	10.8	3.61E-10	1.65E-11	13.110
2	385	22	<10	1	-	-	0	21.6	0.0	2.68E-12	-	13.153
3	500	22	<10	0.5	300	12	0	21.7	10.8	1.08E-10	1.68E-11	13.164
4	598	22	<10	0.5	1000	12	0	21.7	10.9	4.03E-11	5.07E-12	13.181
5	860	22	<10	1	-	-	0	21.8	0.0	4.46E-11	-	13.259
6a	867	22	<10	0.3	1	1	0	23.5	16.5	6.82E-09	1.63E-08	13.309
6b	890	22	<10	0.3	1	1	0	23.7	16.6	1.09E-08	1.69E-08	13.470
6c	913	22	<10	0.3	1	1	0	23.6	16.5	1.62E-08	1.66E-08	13.669
6d	935	22	<10	0.3	1	1	0	24.2	16.9	1.33E-08	3.64E-08	13.822
7	1,002	22	<10	0.5	12	2	0	24.4	12.2	7.14E-10	6.86E-10	14.208
8	1,026	22	<10	0.5	12	2	0	26.5	13.3	1.40E-09	9.60E-10	14.321
9	1,073	22	<10	0.5	1	1	0	28.7	14.3	1.83E-08	1.59E-08	15.823
10	1,102	22	<10	0.5	300	12	0	30.6	15.3	1.05E-09	6.95E-11	15.957
11	1,368	22	<10	1	-	-	0	31.0	0.0	9.04E-11	-	16.046
12a	1,374	22	<10	0.3	1	1	0	32.2	22.6	9.04E-08	5.95E-08	16.875
12b	1,391	22	<10	0.3	1	1	0	32.9	23.0	7.54E-07	6.46E-08	17.324
13	1,398	22	<10	0.5	30	2	0	34.9	17.5	4.29E-08	1.19E-09	18.431
14	1,439	22	<10	0.5	1000	12	0	35.2	17.6	5.98E-11	3.68E-11	18.586
15	1,633	22	<10	1	-	-	0	35.4	0.0	8.10E-11	-	18.740
16	1,638	22	<10	0.3	1	1	0	37.4	26.2	1.98E-07	1.09E-07	19.769
17	1,651	22	<10	0.3	30	1	0	39.5	27.7	2.46E-08	4.57E-09	20.834
18	1,656	22	<10	0.3	1	1	0	46.7	32.7	3.81E-07	2.72E-07	23.860
19	1,663	22	<10	0.5	300	12	0	49.2	24.6	2.15E-08	4.84E-10	24.778
20	2,137	22	<10	1	-	-	0	50.0	0.0	1.57E-10	-	25.048
21	2,141	22	<10	0.5	300	12	0	51.6	25.1	2.52E-08	5.29E-10	25.593

[a]Simulated PWR water with 2 ppm Li, 1100 ppm B, and 2 ppm dissolved hydrogen (≈23 cc/kg).
[b]Represents values in the effluent.

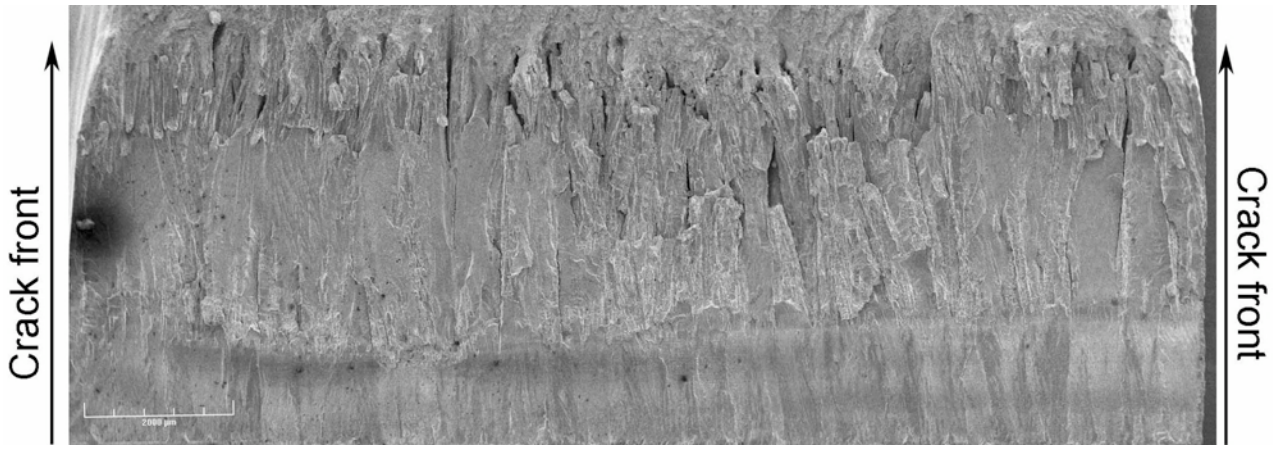

Figure 50. Crack front on fracture surface of sample CT933-TS. Crack advance from bottom to top.

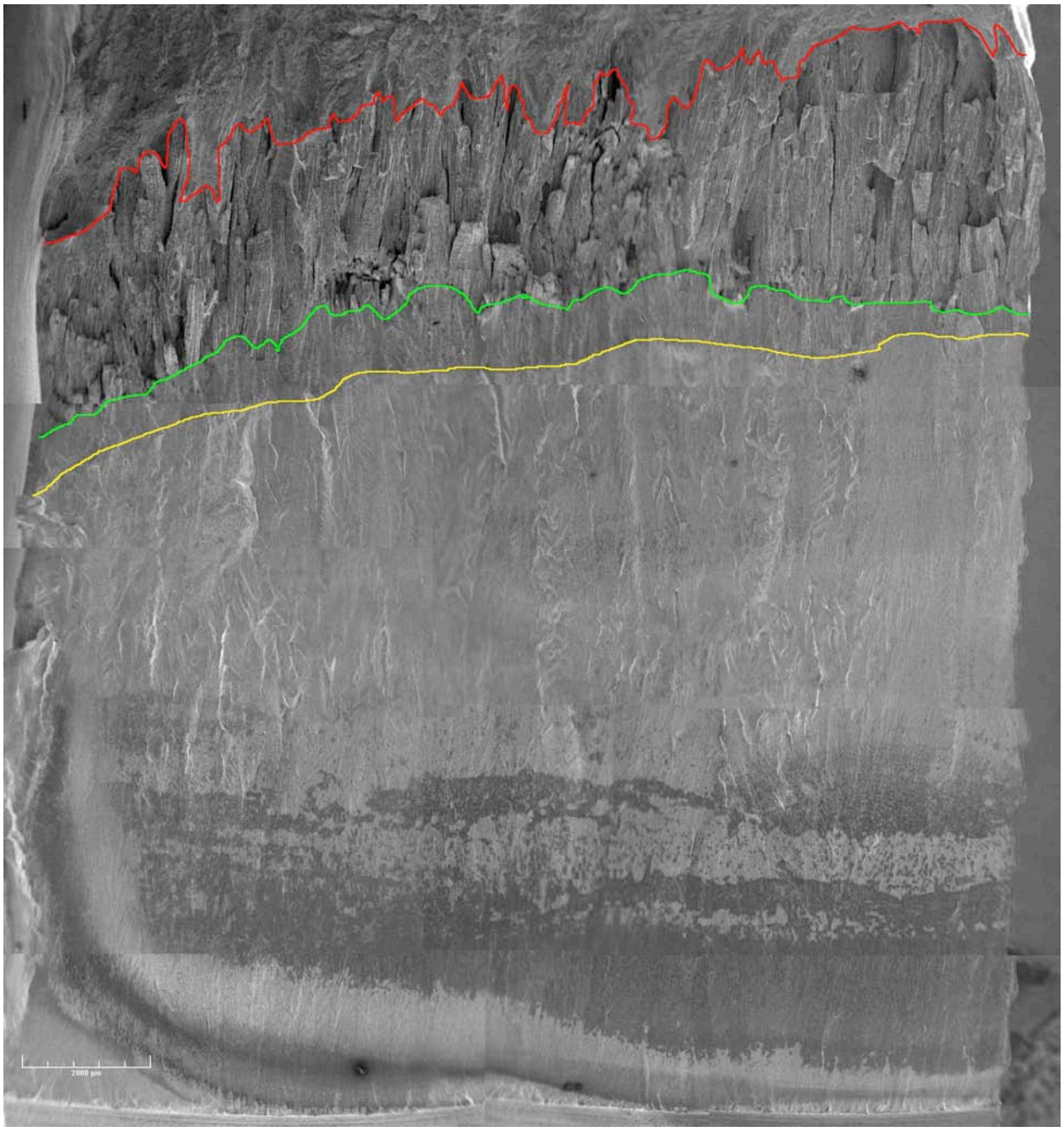

Figure 51. Fracture surface of specimen CT31-W02 TS. Crack extension from bottom to top of the figure.

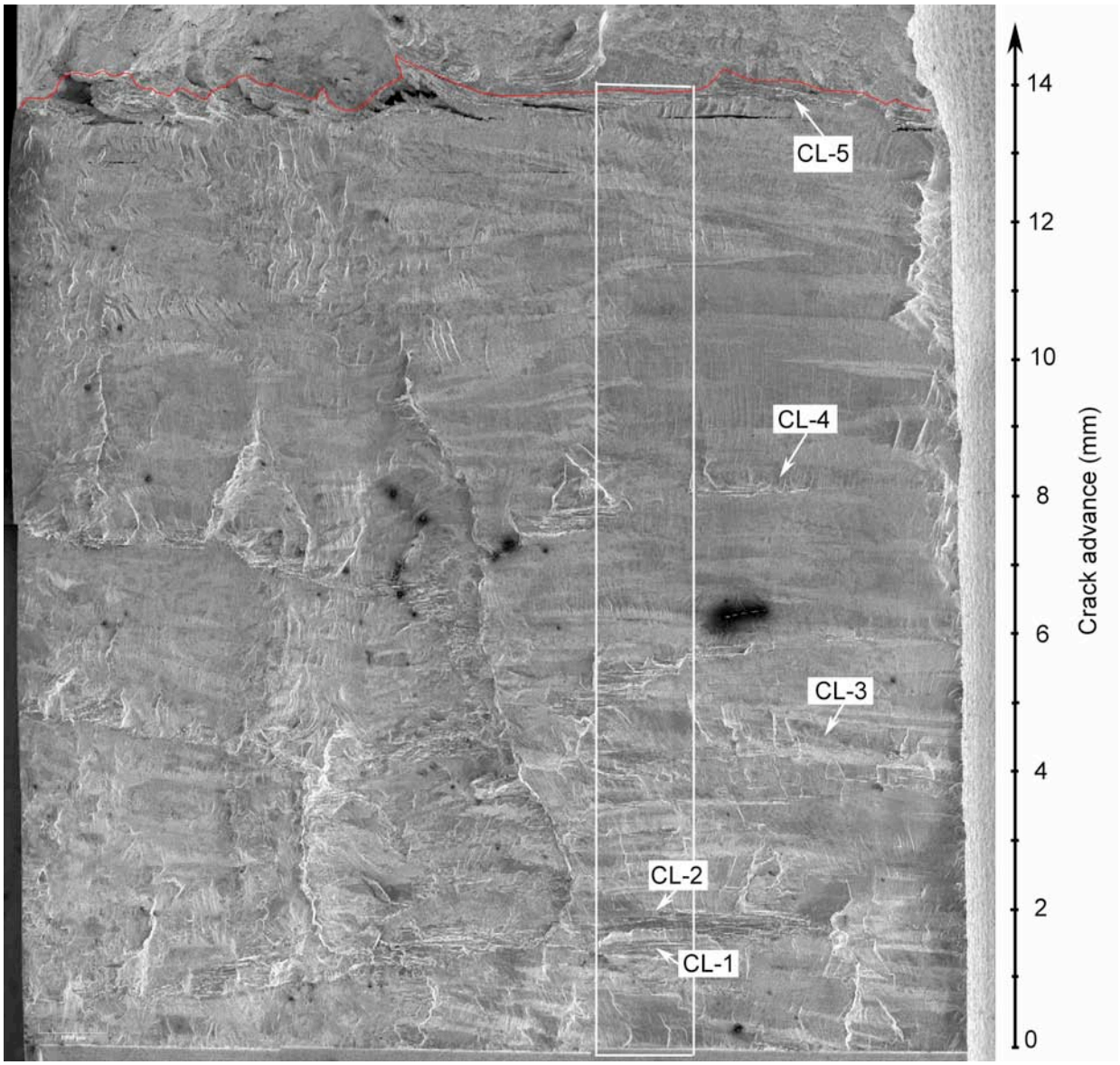

Figure 52. Fracture surface of Alloy 182 weld specimen CT933-TL. The regions dominated by IG fracture corresponding to the constant load (CL) periods are indicated in the figure. Crack advance from bottom to top. The different IG regions are indicated.

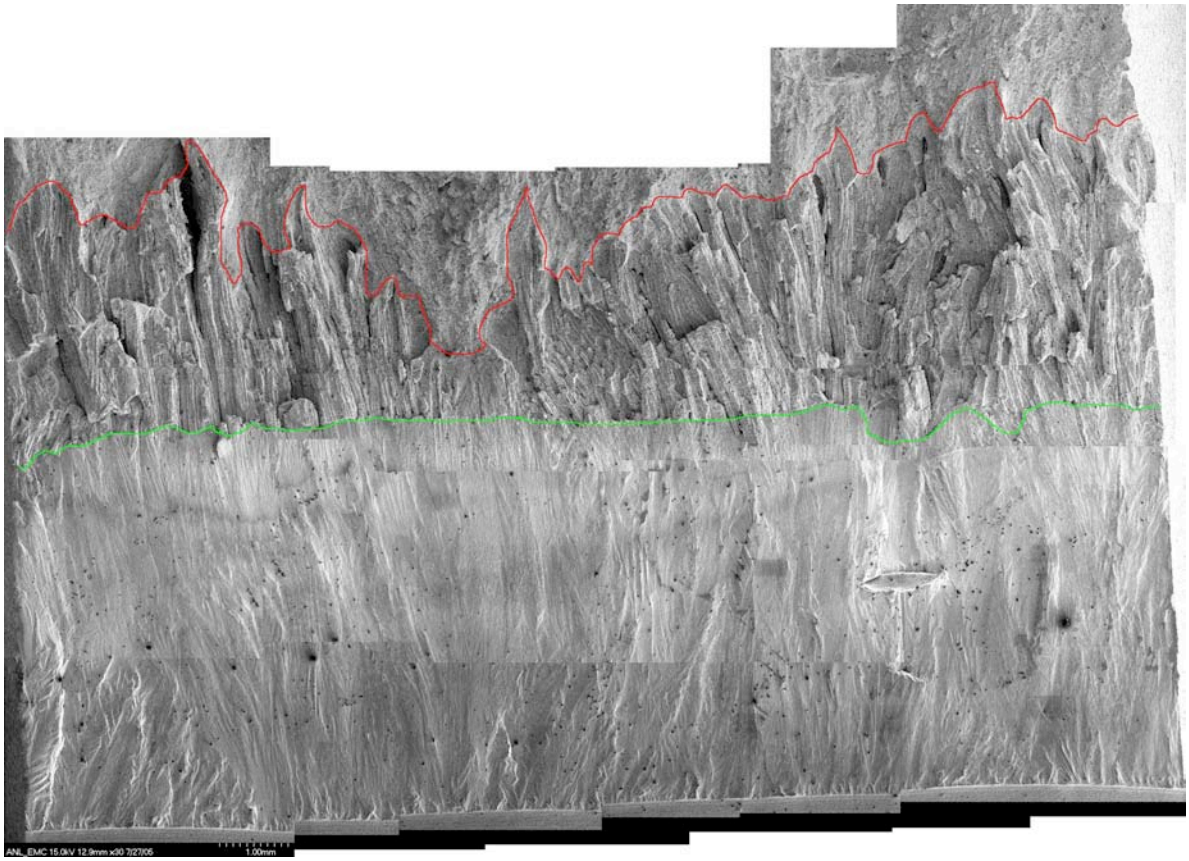

Figure 53. Crack front on fracture surface of sample CT933-LS. Crack extension is from bottom to top.

5.2.2.2 Crack Growth Rates under Cyclic Loading

The fatigue CGR data on Ni-alloy welds in simulated PWR environments are available from ≈120 tests conducted on Alloys 182, 82, 152, and 52 at 243-345°C (469-653°F).[156-160] The loading conditions for these tests include R = 0.1-0.75, K_{max} = 20-100 MPa $m^{1/2}$ (18.2-90.9 ksi $in.^{1/2}$), and rise time = 0.5-5000 s. The results indicate very little effect of PWR environment on the fatigue CGRs of Ni-alloy weld metals. However, only about 10% of the data was obtained under conditions for which significant environmental enhancement would be expected.

The experimental CGRs ($\dot{a}_{env,A182}$ in m/s) obtained by Van Der Sluys et al.[157] for Alloy 82 and by James and Mills[160] for Alloy 182 are plotted in Fig. 54 as a function of the CGRs predicted for Alloy 600 in air ($\dot{a}_{air,A600}$ in m/s) under the same loading conditions. The James and Mills[160] data are for 243°C (469°F), where environmental effects are expected to be small. Most of the data were obtained under loading conditions that result in CGRs greater than 1 x 10^{-9} m/s in air (i.e., load ratios ≤0.2 and rise times ≤10 s). Under these loading conditions, crack growth is primarily controlled by mechanical fatigue, and environmental effects are not expected to be significant even in materials susceptible to environmental enhancement. The data for Alloy 82 (Fig. 54a) extend into a loading region where strain-rate-dependent environmental enhancement would be expected in susceptible materials, although only a few data are in the region where significant enhancement would be expected. The available data show very little frequency-dependent environmental enhancement and are best represented by the expression

$$\dot{a}_{env,A182} = \dot{a}_{air,A600} + 0.12\,(\dot{a}_{air,A600})^{0.82}, \quad (47)$$

where $\dot{a}_{air,A600}$ is the growth rate predicted for Alloy 600 in air under the same loading conditions, although a simple constant multiplier would also represent the data almost as well.

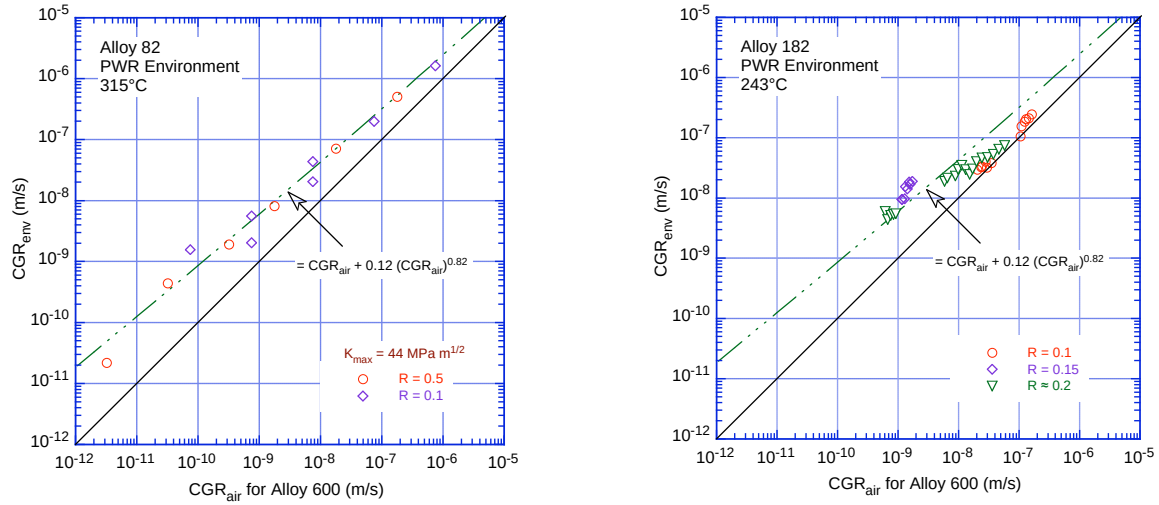

(a) (b)

Figure 54. Fatigue CGR data for (a) Alloy 82 and (b) Alloy 182 weld metal in PWR environment as a function of the growth rate for Alloy 600 in air under the same loading conditions. Data obtained by Van Der Sluys et al. (Ref. 157) and James and Mills (Ref. 160).

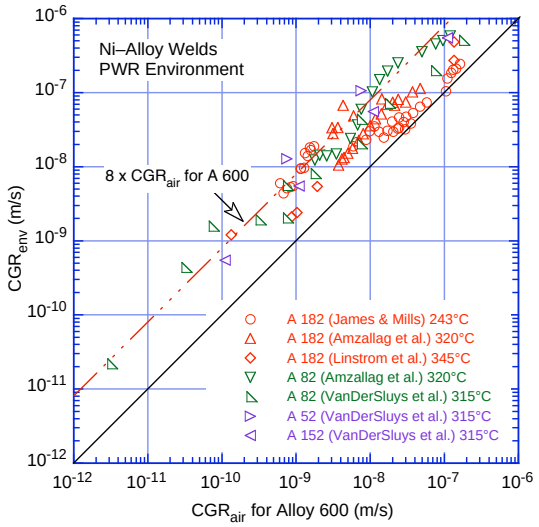

Figure 55.
Fatigue CGR data for Ni-alloy welds in PWR environment as a function of the growth rate for Alloy 600 in air under the same loading conditions. Data from Refs. 156-160.

Literature data on fatigue CGR for Ni-alloy welds in the PWR environment are shown in Fig. 55. The few data available for Alloys 52 and 152 are also included in the figure. Nearly 90% of the CGR data may be bounded by a curve that is a factor of eight greater than the growth rates predicted for Alloy 600 in air under the same loading conditions.

The ANL data on cyclic crack growth rates are shown in Fig. 56. They are consistent with the literature data, as they all seem to show little or no environmental enhancement. Nevertheless, as with the data from the literature, Eq. 47 appears to be a good descriptor of the observed behavior. However, most of the CGR data may be bounded by a curve that is a factor of ten greater than the growth rates predicted for Alloy 600 in air under the same loading conditions.

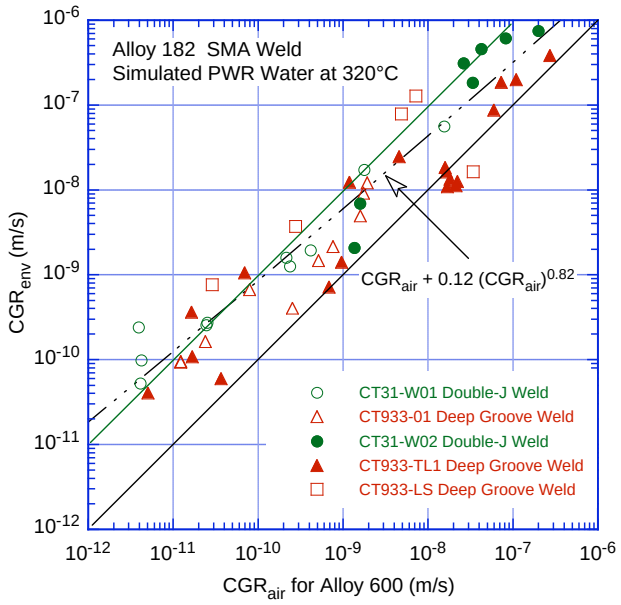

Figure 56.
Cyclic CGR data for laboratory-prepared Alloy 182 SMA weld specimens in simulated PWR environment at 320°C as a function of growth rates for Alloy 600 in air.

5.2.2.3 SCC Growth Rates

The existing SCC CGR database on Ni-alloy welds in simulated PWR environments includes results on Alloy 182 from Westinghouse,[167,168] Studsvik,[159] Electricite de France (EdF),[169] CEA,[170] and ETH;[171] on Alloys 182 and 82 from Westinghouse[172] and Lockheed Martin;[173] on Alloy 82 from Bechtel Bettis;[174,175] and on Alloy 132 from Mitsubishi Heavy Industries.[176] The data have been obtained at temperatures between 289 and 360°C (552 and 680°F) and K_{max} between 13 and 67 MPa $m^{1/2}$ (11.8-60.9 ksi $in.^{1/2}$). A majority of the tests at EdF and all of the ETH tests were performed using wedge-opening-loaded specimens with displacement control. The procedures for the EdF tests describe the need to check the loads at the completion of the test to determine the amount of relaxation that may have occurred, but the only data reported are for the stress intensity factors at the beginning of the test. Most of the tests at the other laboratories have been performed under active load control on specimens fatigue precracked in air.

The experimental CGRs obtained under constant load in the current tests are plotted as a function of stress intensity factor K in Fig. 57a and are compared with available CGR data for Ni-alloy welds[167-173] in Fig. 57b. The industry-proposed disposition CGR curve, based on Eq. 45 for Alloy 182[165] in the PWR environment, is also plotted in the figures; the curve in Fig. 57a was normalized to 320°C (608°F) using an activation energy of 130 kJ/mol. Also, for comparison with the available SCC CGR data, the current test results presented in Fig. 57b were normalized to 325°C (617°F). Most of the data for Alloys 182 and 82 welds are between the Alloy 600 average curve and a factor of 10 above this curve (Fig. 57b).

In the present tests, CGRs were measured along the plane of the columnar grains/dendrites in a direction parallel to the columnar grains (TS or LS orientation) and perpendicular to the columnar grains (TL orientation). Note that the crack planes for TS and LS orientations are along the columnar dendrites, although they are perpendicular to each other (Fig. 49). The results indicate that at high K values the CGRs for cracks propagating along the direction of dendrites (orientations TS and LS) are about a factor of two greater than the CGRs for crack propagation across the direction of dendrites (orientation TL) (Fig. 57a). Similar results have also been obtained in other studies.[167,168,174,175]

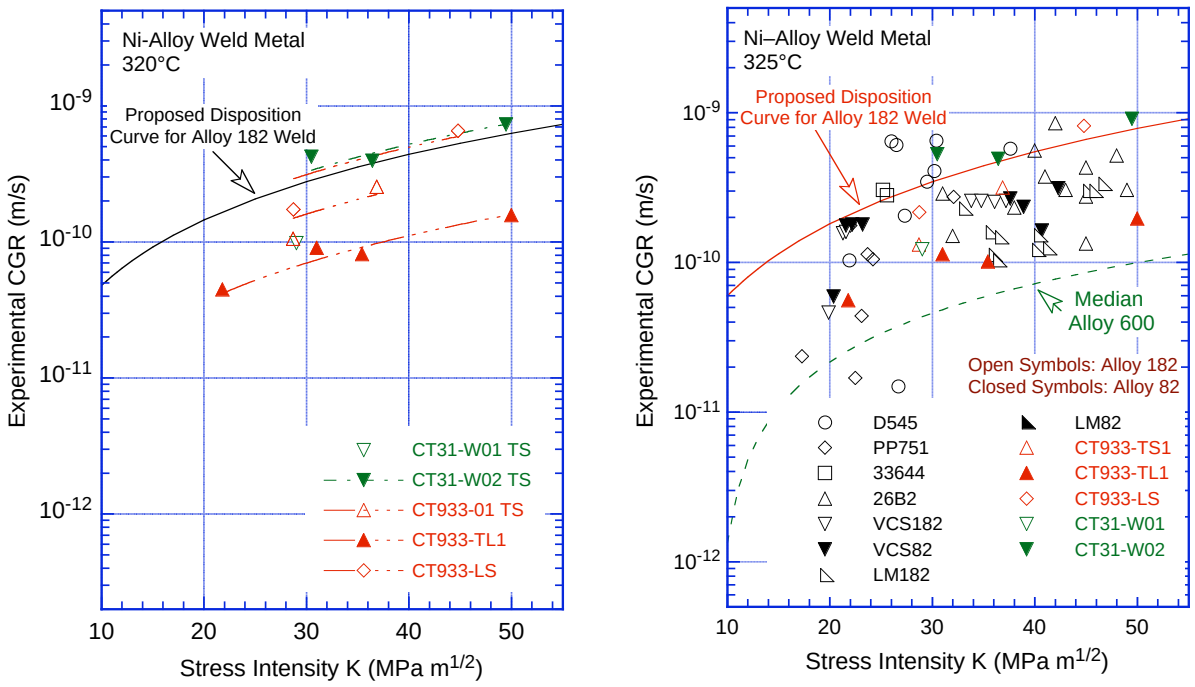

(a) (b)

Figure 57. SCC crack growth data for the Argonne Alloy 182 welds (a) plotted as a function of K and (b) compared with the available data for Alloy 182 and 82 welds in simulated PWR environment. Data from Refs. 159,167-173.

Some earlier studies used the DC potential drop technique to estimate crack extension during the test and shed load to maintain a constant K. However, the presence of unbroken ligaments, time-dependent changes in the resistivity of Ni alloys exposed to a PWR environment, and shifts in the Ni/NiO stability regime with changes in the dissolved hydrogen level can result in significant uncertainties in crack length measurements. Many laboratories concluded that DC potential drop measurements of crack length were not reliable for Alloy 182,[170,175] and use of potential drop was recommended only to detect initiation of active crack growth and to adhere to a "one set of conditions, one test specimen" protocol so that fractographic measurements could be used to determine the change in crack length. However, in some recent studies, including the present study, the reversed-current DC potential drop technique has been successfully used to monitor crack extension in Ni alloys in PWR environments.[159,172,176] Success may depend on the uniformity of the crack front. In addition, an internal reference sample made of the same material as the test specimen is commonly used to normalize the test results to compensate for possible changes in temperature, material resistivity, etc.

5.3 Crack Growth Rates of A182 and A82 Alloys from the Nozzle-to-Pipe Weld of V.C. Summer Reactor

This section presents experimental data on the CGR of weld butter and weld alloys from the nozzle-to-pipe weld spool piece removed from the hot leg of the V.C. Summer reactor. During the reporting period, an additional specimen (WLR-01) from the Alloy 82 weld was tested. As with similar tests described previously, the CGR testing was conducted in a simulated primary water environment and was complemented by post-test fractographic examinations.

5.3.1 Experimental

This section describes the alloys used, the geometry of the 1/2-T CT specimens, and the apparatus and conditions used for crack growth testing in a primary water environment.

5.3.1.1 Material and Specimen Geometry

The spool piece was contaminated with β- and γ-emitting radionuclides. A radiological survey conducted at ANL found a beta/gamma activity of 885 dpm/100 cm^2 on the inner surface and an activity of 1980 dpm/100 cm^2 on the outer surface. All work described herein was performed in accordance with procedures for handling radioactive materials.

Compact tension specimens were machined from the as-received piece; the configuration of the specimens is shown in Fig. 58. During the reporting period, one weld specimen (WLR-01) was tested. The orientations of this specimens relative to the as-received piece are shown in Fig. 59. The fracture planes for these tests are highlighted. The first letter in the specimen ID represents weld (W) of butter (B), and the second and third letters represent the orientation of the fracture plane and direction of crack growth, respectively. For the WLR weld specimen, the direction normal to the fracture plane is longitudinal (L), and the crack growth is in the radial (R) direction. As discussed later, the columnar grains were in the radial direction in the weld and the longitudinal direction in the butter. Thus, crack growth was along the columnar grains in this specimen. A radiological survey conducted prior to testing indicated less than 0.1 mR/h (beta/gamma) on contact and no loose activity.

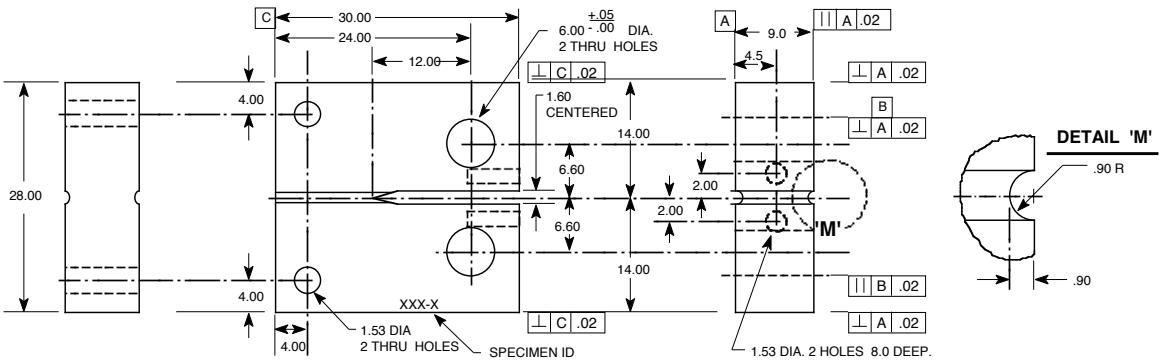

Figure 58. Configuration of the 1/2-T compact tension specimen.

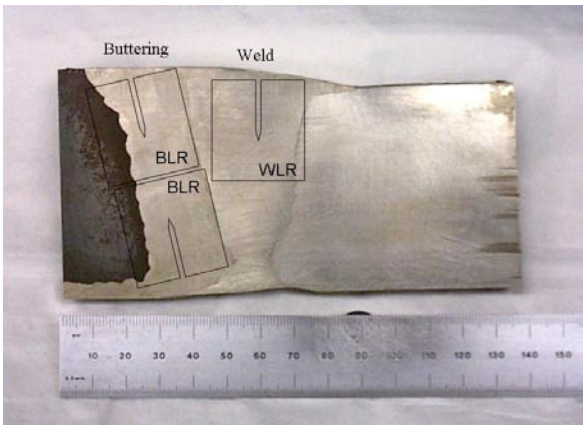

Figure 59.
Orientation and location of the test specimens taken from the V.C. Summer piece. Note that relative to the plane of this figure, the longitudinal (L), radial (R), and circumferential (C) directions, respectively, are horizontal, vertical, and into the page.

For the examination of the microstructure, coupons representative of both alloys were cut from the piece, mechanically polished through 1-μm diamond paste, and electrochemically etched in a 70% H_3PO_4 and water solution at 5 V. The microstructure was observed on planes representative of the CT specimens to be tested. Figure 60 shows micrographs of typical weld microstructures along and across the columnar grains for the Alloy 82 weld. Although the microstructure in the center of the weld along the circumferential plane is not shown in Fig. 60, it was similar to that observed for the butter, except the columnar grains were vertical. The average size of the columnar grains was ≈50 μm across and ≈150 μm along the length of the grains.

Details regarding the crack growth test facility and procedure have been presented earlier in Section 5.2.1.2.

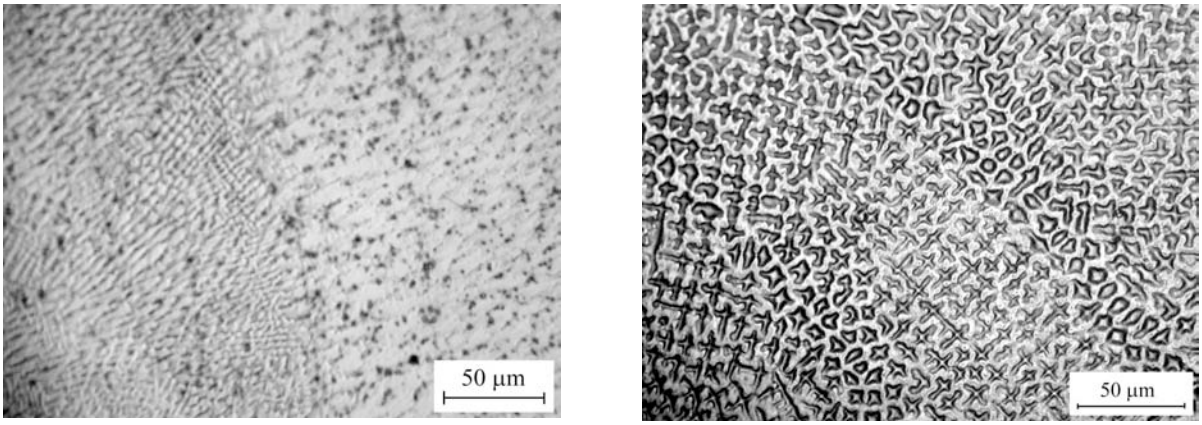

(a) Circumferential Plane, Butter/Weld Interface (b) Radial Plane, Weld

Figure 60. Microstructure of the V.C. Summer Alloy 82 weld.

5.3.2 Results

5.3.2.1 Crack Growth Rates in PWR Environment

The crack growth data along with the test conditions, resulting stress intensity factors K_{max}, and experimental and estimated CGRs for the WLR-01 specimen are given in Table 26.

The fracture surface of WLR-01 is shown in Fig. 61, and a higher magnification micrograph of the IG region is shown in Fig. 62. Cracking initiated in a TG mode under cyclic loading, changed to IG during the long rise-time periods of the test, and remained IG during the constant-load periods. The green and red lines mark the IG region. Secondary IG cracks were observed in the IG region, consistent with the previous observations on other V.C. Summer specimens. The IG region (green and red lines) was designated so as to encompass all these secondary cracks based on the assumption that they initiated and grew during the constant-load period.

Comparison between DC potential data and measurements based on the SEM micrograph yielded correction factors of 1.69 for the TG region and 1.91 for the IG region. The relatively large correction factor for the TG region is consistent with the observation of some IG features within the TG region. The experimental conditions and corrected crack lengths are given in Table 26.

Table 26. Crack growth results for Specimen WLR-01 of Alloy 82 SMA weld in PWR water[a] at 320°C.

Test Period	Test Time (h)	Cond.[b] (µS/cm)	O_2 Conc.[b] (ppb)	Load Ratio R	Rise Time (s)	Down Time (s)	Hold Time (s)	Kmax[c] (MPa $m^{1/2}$)	ΔK (MPa $m^{1/2}$)	CGR_{env} (m/s)	Estimated CGR_{air} (m/s)	Crack Length (mm)
Pre a	103	26	<10	0.30	0.5	0.5	0	19.8	13.8	8.22E-09	1.63E-08	12.640
Pre b	167	26	<10	0.30	50	2	0	19.6	9.8	2.61E-10	6.82E-11	12.719
Pre c	196	26	<10	0.30	1	1	0	16.7	8.4	1.35E-10	1.78E-09	12.729
Pre d	215	26	<10	0.30	0.5	0.5	0	19.7	9.8	2.82E-09	6.92E-09	12.837
Pre e	226	26	<10	0.30	0.25	0.25	0	19.3	13.5	1.20E-08	2.94E-08	13.017
Pre f	265	26	<10	0.50	1	1	0	23.0	11.5	1.52E-08	6.55E-09	14.251
1	315	26	<10	0.50	50	2	0	22.6	11.3	5.93E-10	1.21E-10	14.349
2	389	26	<10	0.70	1000	12	0	22.8	7.1	2.31E-10	1.74E-12	14.418
3	504	26	<10	0.70	1000	12	0	23.5	7.8	1.60E-10	2.29E-12	14.531
4	841	26	<10	1.00	-	-	-	23.2	-	2.07E-11	-	14.531
5	1082	26	<10	1.00	-	-	-	31.2	-	5.43E-12	-	14.590
6	1203	26	<10	0.70	1000	12	0	30.9	9.3	2.04E-11	5.53E-12	14.590
7	1392	26	<10	0.70	300	12	0	31.3	9.4	1.94E-11	1.94E-11	14.602
8	1398	26	<10	0.30	0.5	0.5	0	34.7	24.3	1.03E-07	1.62E-07	15.614
9	1417	26	<10	0.50	100	12	0	38.1	19.1	7.01E-09	5.21E-10	16.099
10	1439	26	<10	0.50	300	12	0	41.8	20.9	8.00E-08	2.55E-10	16.410
11	1466	26	<10	0.50	50	2	0	43.7	21.8	2.03E-09	1.80E-09	16.656
12	1531	26	<10	0.50	300	12	0	44.6	22.3	8.95E-10	3.27E-10	16.854
13	1634	26	<10	0.50	1000	12	0	46.6	23.3	4.12E-10	1.17E-10	16.964
14	2469	26	<10	1.00	-	-	-	49.8	-	7.71E-11	-	17.182

[a]Simulated PWR water with 2 ppm Li, 1100 ppm B, and 2 ppm dissolved hydrogen (≈23 cc/kg).
[b]Represents values in the effluent.
[c]At the end of the test the maximum allowed K_{max} was 22.6 MPa $m^{1/2}$.

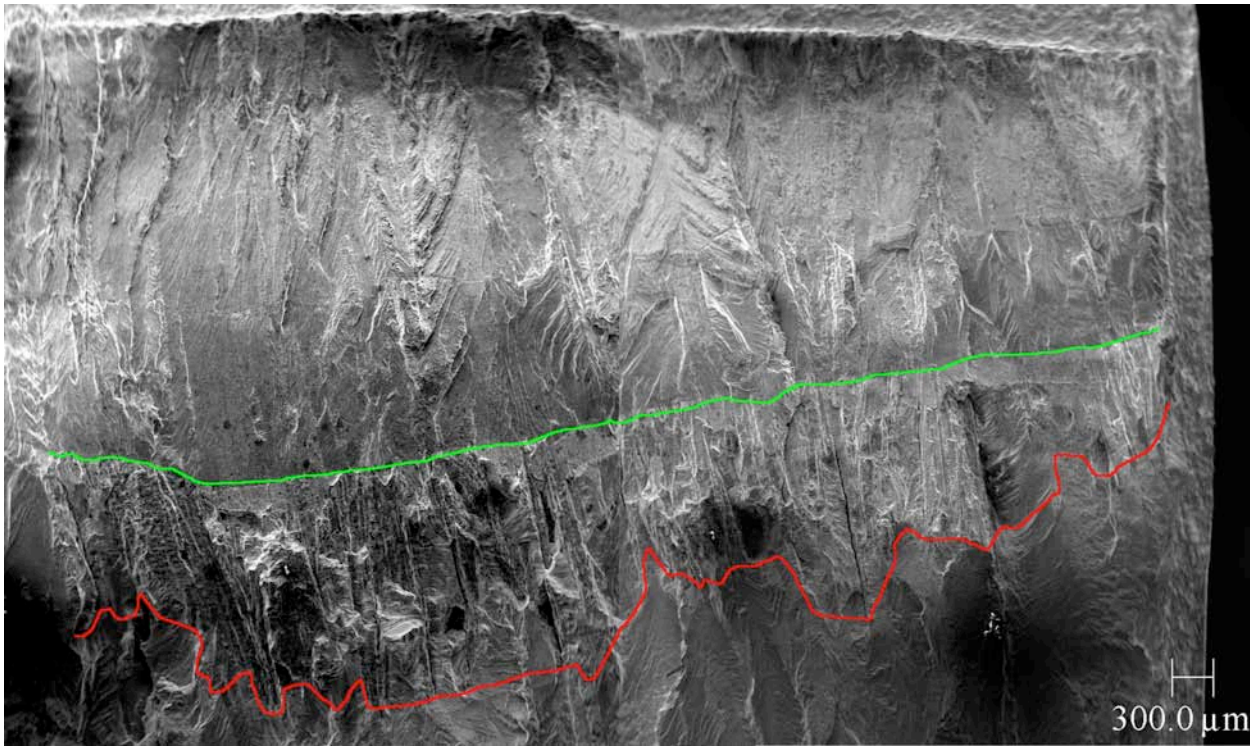

Figure 61. Micrograph of the fracture surface of the weld V.C. Summer WLR-01 specimen. Crack advance is from top to bottom.

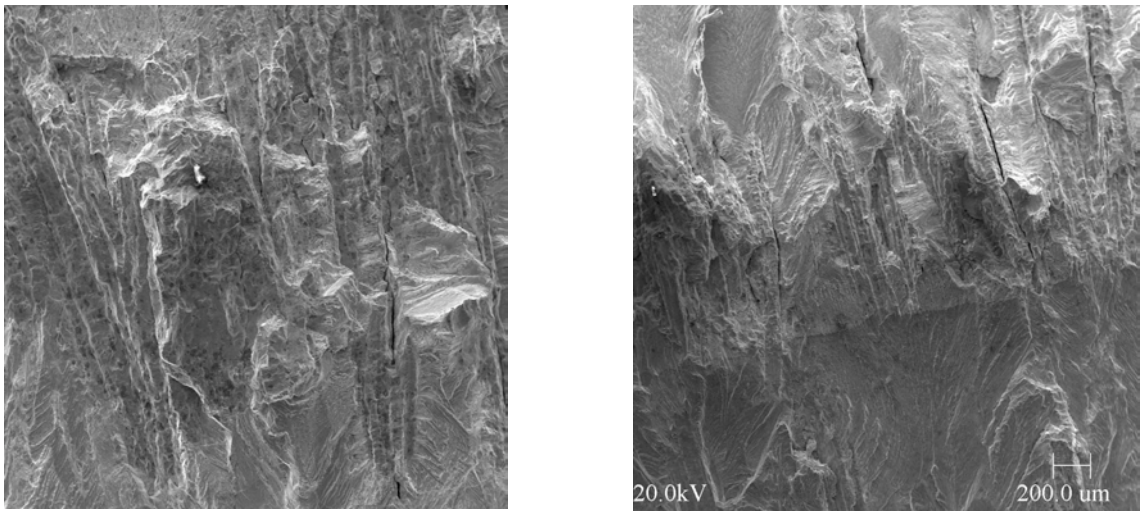

(a) (b)

Figure 62. Micrographs of the fracture surface of specimen BCR-01 at locations 1 (a) and 2 (b) in Fig. 61.

5.3.2.2 Crack Growth Rates under Cyclic Loading

Figure 63 shows the CGR rates under cyclic loading for the current (WLR-01) and the previous two specimens (WCR-01 and BCR-01) as a function of the CGRs obtained from Eqs. 42 and 43 for Alloy 600 in air under the same loading conditions. Experimental data obtained by Amzallag et al.,[156] Van Der Sluys et al.,[157,158] Lindstrom et al.,[159] and James and Mills[160] are also included in the figure. The results indicate that with the exception of the two V.C. Summer welds (WCR-01 and BCR-01), the CGR data are bound by the rates in air for Alloy 600 (solid line) and eight times those (dotted line). Under mechanical fatigue loading conditions (i.e., growth rates $>10^{-8}$ m/s), the CGRs of the two V. C. Summer welds are lower than those predicted by Eqs. 42 and 43 for Alloy 600 in air. Ideally, in Fig. 63 the data on the weld metals in the PWR environment should be compared with CGRs in air for the weld metals, not Alloy 600. Although the CGRs in the PWR environment are in most cases higher than those in air, much of this difference may not be due to environmental effects, but rather may simply reflect differences in the fatigue crack growth rates of Alloys 182 and 82 compared with that of Alloy 600.

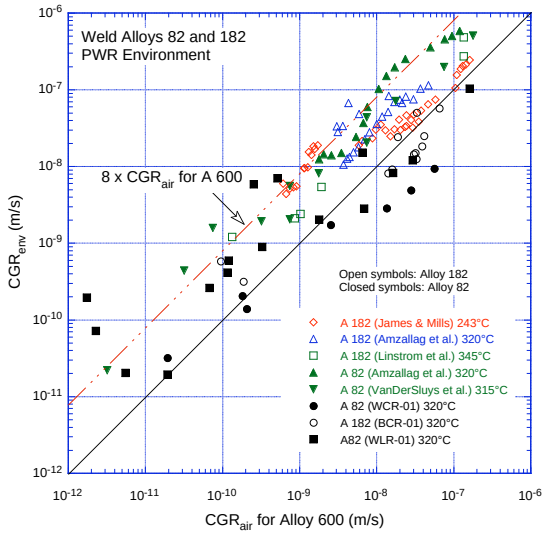

Figure 63.
Fatigue CGR data for Ni-alloy welds in PWR environment plotted as a function of the growth rate for Alloy 600 in air under the same loading conditions. Data from the current study and Refs. 156-160.

When environmental enhancement occurs, the relative CGRs in the PWR environment compared with those in air should be increasing with decreasing CGRs in air. It is not clear whether all the data of Fig. 63 show this behavior; however, most of the data were obtained under loading conditions where the crack growth is either controlled primarily by mechanical fatigue or, as is the case of James and Mills,[160] obtained at 243°C (469°F), a temperature where environmental effects are expected to be small. For the V. C. Summer Alloy 182 specimen, those loading conditions resulting in CGRs less than 1×10^{-9} m/s in air (i.e., load ratios greater than 0.5 and rise times greater than 30 s) appear to have resulted in enhanced CGRs in the PWR environment. On the fracture surface, these conditions are expected to correspond to the transition between TG and IG fracture modes.

5.3.2.3 SCC Growth Rates

Although each test period at constant load lasted in excess of 200 h (Table 26), the crack advanced quite slowly; hence, the crack length increments are relatively small. Thus, in the direction of crack advance, the crack typically grew less than a grain size in the allotted time period. Nevertheless, based on an average size of ≈50 μm across and ≈150 μm along the length of the columnar grains, it is estimated that across the full width of the sample, the crack advanced along ≈300 grain boundaries during each constant-load test period in Specimen WCR-01, where the crack front was along the columnar grains, and along ≈45 grain boundaries in Specimen BCR-01, where the crack front was across the columnar grains. A simple statistical formalism by Alexandreanu and Was[177] was used to analyze how well these samples of boundaries describe the material being tested, in other words, how representative are these samples of the full spectrum of boundary types in the material - the grain boundary character distribution (GBCD). Specifically, the fractional errors associated with the cracking-susceptible random boundaries that would result from boundary populations of these sizes were estimated. Assuming a random boundary fraction of 70%, typical for a weld alloy, the errors for the fractions of (cracked) random boundaries are ≈3.8% in WCR-01 and ≈9.7% in BCR-01. Both of these numbers are comparable with the degree of homogeneity of random boundaries in a Ni-base alloy; thus, as far as GBCD is concerned, no additional benefit can be obtained by considering larger populations of boundaries. Using the same approach, the benefit of doubling the test time (400 h instead of 200 h) was also estimated. In such a case, assuming a similar CGR, the population of cracked boundaries in BCR-01, for example, would double to approximately 90 in each constant-load period. As a result, the error in the fraction of random boundaries would drop to ≈6.9%. These results were somewhat expected: because random boundaries are quite abundant in Ni-alloy weld, fractional errors cannot be significantly improved by increasing the sample size, i.e., doubling the number of boundaries. From a crack advance viewpoint, it appears unlikely that minor changes, such as 9.7% vs. 6.9% in the population of random boundaries, would impact significantly the observed cracking behavior.

The experimental constant-load CGRs for the two V. C. Summer weld and butter alloys are compared with similar data obtained in the present study on laboratory-prepared welds (a double-J weld design and a deep-groove filled weld design)[164] in Fig. 64a. The proposed disposition curve for Alloy 182 welds in a PWR environment (i.e., represented by Eqs. 45 and 46) is also included in the figure.[165] The disposition curve was normalized to 320°C (608°F) using an activation energy of 130 kJ/mol. The results indicate that the CGRs of Alloy 82 weld material (Specimens WLR-01 and WCR-01) with growth direction along the dendrites are comparable to those of the Alloy 182 butter material (Specimen BCR-01) with growth direction transverse to the dendrites. Note that the crack planes for LR and CR orientations are along the columnar dendrites, although they are perpendicular to each other. In general, CGRs in Alloy 182 are a factor of 2.6 higher than in Alloy 82;[165] however, the rates along a direction transverse to the dendrites are a factor of ≈2 lower than those parallel to the dendrites.

The effects of alloy type and specimen orientation seem to have cancelled each other, yielding approximately the same growth rates for the weld and butter alloys.

The results also indicate that for similar orientations, the CGRs of the V. C. Summer weld and butter alloys are generally lower than those of the laboratory-prepared welds. For example, the crack plane and direction of crack growth for Specimen BCR (solid purple circles in Fig. 64a) of the V. C. Summer butter Alloy 182 are similar to those for Specimen CT933-TL1 (solid red triangles in Fig. 64a) of the laboratory-prepared Alloy 182 weld. The CGRs for the V. C. Summer alloy are a factor of ≈2 lower. Similarly, the crack plane and direction of crack growth for Specimen WCR or WLR (purple squares or circle in Fig. 64a) of the V. C. Summer Alloy 82 weld are similar to those for the laboratory-prepared Alloy 182 weld specimens in LS or TS orientations. The experimental CGRs of the V. C. Summer weld are a factor of ≈5 lower than those of the laboratory-prepared welds; typically, the growth rates of Alloy 82 are a factor of ≈2.6 lower than those of Alloy 182.[165]

Figure 64b shows the same V. C. Summer CGR data plotted along with data obtained by Jacko et al. on similar V. C. Summer weld and butter alloys in the PWR environment at 325°C (617°F);[172] the results from the present study were normalized to 325°C (617°F) for comparison. The CGRs from the present study are a factor of ≈4 lower than those obtained by Jacko et al. The reason for the differences in the results from the two studies is not clear. The crack fronts in the tests reported here are relatively straight. The crack fronts in the tests in Jacko et al.[172] do not appear to be as straight. Crack growth rates in isolated "fingers" may be more rapid than the overall growth of a straight crack front.

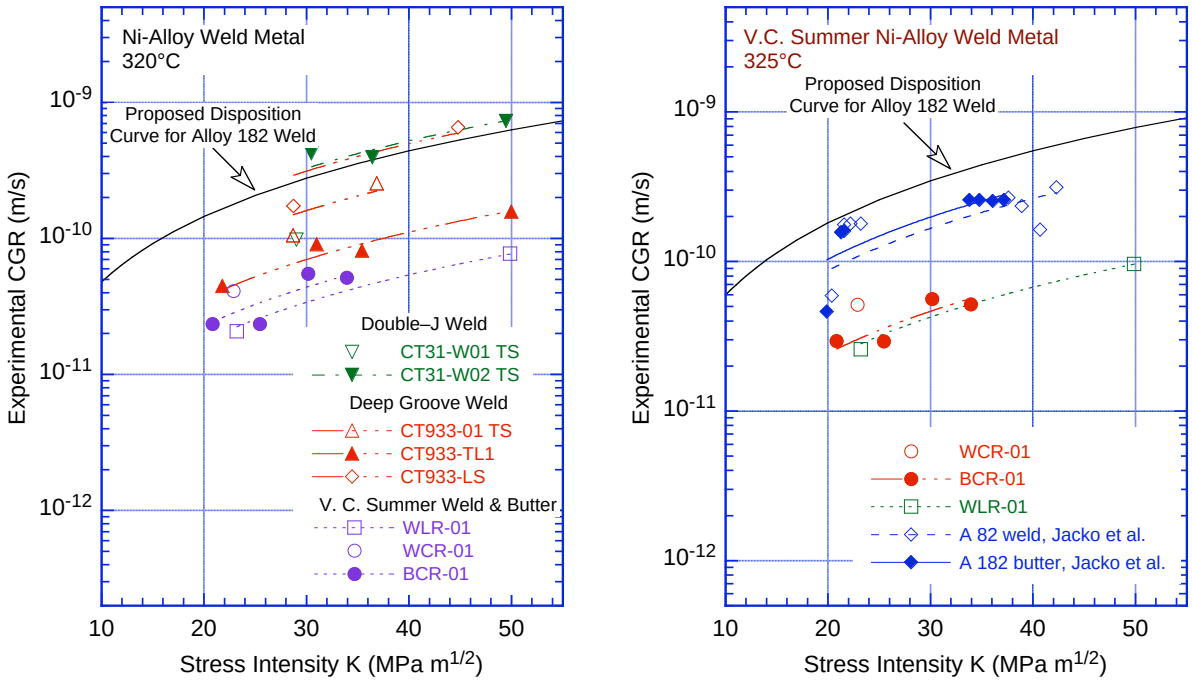

(a) (b)

Figure 64. Comparison of the CGR data for the V. C. Summer weld and butter alloys with the data obtained on (a) laboratory-prepared welds in the present study and (b) V. C. Summer weld and butter alloys by Jacko et al. (Ref. 172).

6 Summary

6.1 Environmental Effects on Fatigue ε-N Behavior

An overview of the existing fatigue ε-N data for carbon and low-alloy steels and wrought and cast austenitic SSs in air and LWR environments is presented. The data are evaluated to (a) identify the various material, environmental, and loading parameters that influence fatigue crack initiation and (b) establish the effects of key parameters on the fatigue life of these steels. The results indicate that in air, the ASME mean curve for low-alloy steels is in good agreement with the available experimental data, and the curve for carbon steels is somewhat conservative. However, in air, the ASME mean curve for SSs is not consistent with the experimental data at strain amplitudes <0.5% or stress amplitudes <975 MPa (<141 ksi); the ASME mean curve is nonconservative.

The fatigue lives of both carbon and low-alloy steels and austenitic SSs are decreased in LWR environments. The key parameters that influence fatigue life in these environments (e.g., temperature, DO level in water, strain rate, strain or stress amplitude, and, for carbon and low-alloy steels, S content of the steel) have been identified. Also, the range of the values of these parameters within which environmental effects are significant has been clearly defined. If these critical loading and environmental conditions exist during reactor operation, then environmental effects will be significant and need to be included in the ASME Code fatigue evaluations.

Statistical models developed earlier to predict fatigue lives of small, smooth specimens of carbon and low-alloy steels and wrought and cast austenitic SSs as a function of material, loading, and environmental parameters have been updated/revised by drawing upon a larger fatigue ε-N database. An approach that can be used to incorporate the effects of LWR coolant environments into the ASME Code fatigue evaluations, based on the environmental fatigue correction factor, F_{en}, is discussed. The fatigue usage for a specific stress cycle of load set pair based on the Code fatigue design curves is multiplied by the correction factor to account for environmental effects.

The report also presents a critical review of the ASME Code fatigue adjustment factors of 2 on stress and 20 on life and assesses the possible conservatism in the current choice of these factors. Data available in the literature have been reviewed to evaluate the margins on cycles and stress that are needed to account for such differences and uncertainties. Monte Carlo simulations were performed to determine the margin on cycles needed to obtain a fatigue design curve that would provide a somewhat conservative estimate of the number of cycles to initiate a fatigue crack in reactor components. The results suggest that the current ASME Code requirements of a factor of 20 on cycle to account for the effects of material variability and data scatter, as well as size, surface finish, and loading history in low cycle fatigue, contain at least a factor of 1.7 conservatism. To reduce this conservatism, fatigue design curves may be developed from the ANL statistical model by reducing the mean-stress adjusted best-fit curve by a factor of 2 on stress or 12 on cycles, whichever is more conservative.

6.2 Irradiation-Assisted Stress Corrosion Cracking of Austenitic Stainless Steel in BWRs

The effects of the GBE process on the IASCC behavior of austenitic SSs are being investigated. Slow-strain-rate tensile tests have been completed in high-purity 289°C (552°F) water on several austenitic SSs, Alloy 690, and their GBE counterparts that were irradiated to 2.0-2.4 dpa in the Halden phase-II study. In general, all materials showed significant irradiation hardening and loss of ductility

[e.g., the yield stress increased above 700 MPa (101.5 ksi)], and uniform elongation for all materials, except GBE Alloy 690, was less than 6%. Uniform elongation for the GBE Alloy 690 was ≈22%. Some strain hardening was observed for the high-C Types 304 and 316 SSs, whereas strain softening was observed for the low-C Type 304L SS. Fracture surface analyses have not been performed to determine the fraction of IG fracture for these materials. However, the results for uniform elongation suggest that, at the dose level of the present study (2.0-2.4 dpa), GBE does not seem to have a significant effect on the IASCC behavior of austenitic SSs.

The results from the Halden phase-II study are consistent with the finding from the Halden phase-I study, namely, that a minimum C content (≥0.04 wt.%) is required for IASCC resistance. However, a beneficial effect of low S on IASCC resistance as concluded in the Halden phase-I study is not obvious from the uniform elongations of the Halden phase-II materials. Also, no clear dependence can be observed between the Si and P contents and uniform elongations of the materials.

Crack growth rate tests have been conducted in BWR environments on Type 316 SS irradiated to 0.3, 0.9, and 2.0 x 10^{21} n/cm^2 (0.45, 1.35, and 3.0 dpa), and on sensitized Type 304 SS and SS weld HAZ material irradiated to 1.44 x 10^{21} n/cm^2 (2.16 dpa). The CGR tests on materials irradiated to 2.16 dpa were followed by a fracture toughness J-R curve test in the water environment. The weld HAZ specimens were obtained from an SMA weld prepared from a 30-mm plate of Type 304 SS (Heat 10285).

In the NWC BWR environment, the cyclic CGRs of SSs irradiated to ≈0.45 dpa are the same as those for nonirradiated materials, whereas the CGRs of SSs irradiated to 0.75-3.0 dpa are significantly higher. The CGRs are decreased by more than an order of magnitude when the DO level is decreased. A superposition model has been used to represent the experimental CGRs. The CGR in the environment is expressed as the superposition of the rate in air (mechanical fatigue) and the rates due to corrosion fatigue and SCC.

Similarly, in the NWC BWR environment, the SCC growth rates of nonirradiated SSs or materials irradiated to ≈0.45 dpa are either comparable to or slightly lower than the disposition curve in NUREG-0313 for sensitized SSs in water with 8 ppm DO. For austenitic SSs irradiated to 0.75-3.0 dpa, the CGRs are a factor of ≈6 higher than the NUREG-0313 disposition curve. The results also indicate a benefit from a low-DO environment. In general, for the materials and irradiation conditions investigated in the present study, the CGRs decreased more than an order of magnitude when the DO level was decreased from the NWC to the HWC BWR environment. However, a few specimens did not show the benefit of the low-DO environment; the reason for this behavior is not clear.

The results of the fracture toughness J-R curve tests in the NWC BWR environment show the same general trend observed for the tests in air; however, the J_{Ic} values in water are slightly lower than those in air. A water environment could influence fracture toughness in two ways. An IG starter crack compared to a TG fatigue crack used in nearly all the fracture toughness tests may decrease the J_{Ic} value for the test material, and the effect of the corrosion/oxidation reaction during crack extension may decrease the tearing modulus. Controlled companion tests in air on the same materials are in progress to accurately determine the effect of the water environment on fracture toughness.

6.3 Irradiation-Assisted Cracking of Austenitic Stainless Steel in PWRs

The objectives of this task are to investigate the susceptibility of austenitic SS core internals to IASCC in PWRs as a function of the fluence, material chemistry, and cold-work and to evaluate the void swelling behavior in austenitic SSs at PWR-relevant dose and temperature conditions. Both SSRT tests

and microstructure examination are being conducted on SS specimens irradiated in the BOR-60 reactor in Russia. A comprehensive irradiation experiment in the BOR-60 sodium-cooled breeder reactor is under way to obtain a large number of tensile and disk specimens irradiated at ≈325°C (≈617°F) to 5, 10, 20, and 40 dpa. Irradiations to the first three levels have been completed during irradiation cycle BORIS-6, and the specimens are available for testing.

The SSRT tests will be conducted in the facility currently being used for tests on the Halden specimens. The existing loading fixtures have been modified for the BOR-60 tensile specimens, which are smaller than the Halden specimens. To avoid bending or twisting of the specimens, a sample grip system has been designed for installing the specimens. To avoid the premature loading of the specimen during heating and pressurization, smaller pull rods have been fabricated and tested at the PWR pressure and temperature conditions. Also, to evaluate potential effects of neutron flux on IASCC susceptibility of austenitic SSs, several heats of materials that were included in both Halden and BOR-60 irradiations have been identified, and will be tested similarly.

Small specimen testing techniques have been reviewed to explore the possibility of extracting fracture toughness information from the 3-mm (0.118-in.) TEM disk samples. Several "punch" tests and instrumented micro-indentation tests have been developed over the years. The basic procedure of punch tests is to drive a small indenter into a flat sample mounted on a die, while load-displacement is recorded for the process. The results indicate that, although the instrumented micro-indentation test is the easiest one to implement because of its commercial availability, the ball punch (bulge) test shows the most promise of providing meaningful information on fracture toughness as well as tensile properties.

The available database on void swelling and density change of austenitic SSs has been critically reviewed. Irradiation conditions, test procedures, and microstructural characteristics were carefully examined, and key factors that are important to determine the relevance of the database to PWR conditions were evaluated. The results indicate that swelling in thin-walled tubes and baffle bolts in a PWR is not a concern. The PWR baffle reentrant corners are most susceptible to high swelling rates and, hence, high swelling at EOL, especially in limited regions where the irradiation temperature is high. However, void swelling in a reentrant corner will unlikely exceed the threshold level of ≈4% beyond which the swelling rate reaches the steady state of 1%/dpa. This estimation is only preliminary, and the maximum temperature of reentrant corners needs to be more accurately quantified.

6.4 Environmentally Assisted Cracking of Alloys 600 and 690 in LWR Water

The resistance of Ni alloys to EAC in simulated LWR environments has been evaluated. Crack growth tests are being conducted to establish the effects of relevant material, environmental, and loading conditions on the CGRs of Ni alloys and their welds. During the current reporting period, CGR tests were completed in the PWR environment on laboratory-prepared Alloy 182 weld, and Alloys 82 and 182 from the nozzle-to-pipe weld of the V. C. Summer reactor. The results are compared with the existing CGR data for Ni alloys and welds to determine the relative susceptibility of these materials to EAC under a variety of loading conditions.

The environmental enhancement of CGRs under cyclic loading was determined relative to the CGRs that would be expected under the same loading conditions for Alloy 600 in air. The results indicate little or no environmental enhancement of CGRs for Alloy 182 weld metal in the PWR environment. The CGRs of Alloy 182 in the PWR environment are a factor of ≈5 higher than those of Alloy 600 in air under the same loading conditions.

The experimental CGR for the Alloy 182 weld obtained under constant load was close to the expected CGR for the median behavior of Alloy 600 in the PWR environment. Most of the existing CGR data for Alloy 182 and 82 welds are a factor of 1-10 greater than the median value for Alloy 600. The effect of the stress intensity factor on SCC crack growth for Ni-alloy welds is represented by the Scott model. Heat-to-heat comparisons of the CGR data were made. The cumulative distribution of the parameter A in the Scott model was used to estimate the heat-to-heat variability of the population of Alloy 182 and 82 welds. Values of the parameter A as a function of the percentage of the population bounded and the confidence level were determined. Under similar loading and environmental (PWR) conditions, the mean CGRs for Ni-alloy welds appear to be a factor of ≈2 higher than the mean CGRs for Alloy 600.

A crack growth test on the nozzle-to-pipe weld specimen from the V. C. Summer reactor was conducted in a PWR environment at 320°C (608°F). Two similar specimens from the butter (Alloy 182) and the weld (Alloy 82) had been tested previously. The results indicate that cyclic loading with high load ratios and long rise times preceding the constant-load test initiates IG fracture and ensures a relatively straight crack front. Defects in the form of pores, cracks, and precipitates are present in the V. C. Summer alloys and may impede crack propagation. The fatigue CGRs of both Alloy 82 weld and Alloy 182 butter from the V. C. Summer weld spool piece are significantly lower than those typically observed for these alloys in air. The SCC growth rates for the V. C. Summer weld and butter alloys are lower than data obtained by others on the same alloys and lower than the proposed disposition curve. These results are not so statistically unlikely that they can be said to prove that there is a difference between field and laboratory welds, but such a difference would be consistent with the observations that operating experience indicates that PWSCC appears to occur more frequently in wrought Ni-base Alloy 600 components than in the weld metal Alloys 82 and 182 used with Alloy 600, despite the fact that in laboratory tests in PWR coolant environments, the SCC susceptibility of Alloy 182 is usually found to be greater than that of Alloy 600, while that of Alloy 82 is comparable to that of Alloy 600.

References

1. Langer, B. F., "Design of Pressure Vessels for Low-Cycle Fatigue," ASME J. Basic Eng. **84**, 389-402, 1962.

2. "Criteria of the ASME Boiler and Pressure Vessel Code for Design by Analysis in Sections III and VIII, Division 2," The American Society of Mechanical Engineers, New York, 1969.

3. Cooper, W. E., "The Initial Scope and Intent of the Section III Fatigue Design Procedure," Welding Research Council, Inc., Technical Information from Workshop on Cyclic Life and Environmental Effects in Nuclear Applications, Clearwater, Florida, Jan. 22-21, 1992.

4. Chopra, O. K., and W. J. Shack, "Effects of LWR Coolant Environments on Fatigue Design Curves of Carbon and Low-Alloy Steels," NUREG/CR-6583, ANL-97/18, March 1998.

5. Gavenda, D. J., P. R. Luebbers, and O. K. Chopra, "Crack Initiation and Crack Growth Behavior of Carbon and Low-Alloy Steels," Fatigue and Fracture 1, Vol. 350, S. Rahman, K. K. Yoon, S. Bhandari, R. Warke, and J. M. Bloom, eds., American Society of Mechanical Engineers, New York, pp. 243-255, 1997.

6. Chopra, O. K., and W. J. Shack, "Environmental Effects on Fatigue Crack Initiation in Piping and Pressure Vessel Steels," NUREG/CR-6717, ANL-00/27, May 2001.

7. Chopra, O. K., "Mechanisms and Estimation of Fatigue Crack Initiation in Austenitic Stainless Steels in LWR Environments," NUREG/CR-6787, ANL-01/25, Aug. 2002.

8. Hale, D. A., S. A. Wilson, E. Kiss, and A. J. Gianuzzi, "Low-Cycle Fatigue Evaluation of Primary Piping Materials in a BWR Environment," GEAP-20244, U.S. Nuclear Regulatory Commission, Sept. 1977.

9. Ranganath, S., J. N. Kass, and J. D. Heald, "Fatigue Behavior of Carbon Steel Components in High-Temperature Water Environments," Low-Cycle Fatigue and Life Prediction, ASTM STP 770, C. Amzallag, B. N. Leis, and P. Rabbe, eds., American Society for Testing and Materials, Philadelphia, pp. 436-459, 1982.

10. Nagata, N., S. Sato, and Y. Katada, "Low-Cycle Fatigue Behavior of Pressure Vessel Steels in High-Temperature Pressurized Water," ISIJ Intl. **31** (1), 106-114, 1991.

11. Higuchi, M., and K. Iida, "Fatigue Strength Correction Factors for Carbon and Low-Alloy Steels in Oxygen-Containing High-Temperature Water," Nucl. Eng. Des. **129**, 293-306, 1991.

12. Katada, Y., N. Nagata, and S. Sato, "Effect of Dissolved Oxygen Concentration on Fatigue Crack Growth Behavior of A533 B Steel in High Temperature Water," ISIJ Intl. **33** (8), 877-883, 1993.

13. Kanasaki, H., M. Hayashi, K. Iida, and Y. Asada, "Effects of Temperature Change on Fatigue Life of Carbon Steel in High Temperature Water," Fatigue and Crack Growth: Environmental Effects, Modeling Studies, and Design Considerations, PVP Vol. 306, S. Yukawa, ed., American Society of Mechanical Engineers, New York, pp. 117-122, 1995.

14. Nakao, G., H. Kanasaki, M. Higuchi, K. Iida, and Y. Asada, “Effects of Temperature and Dissolved Oxygen Content on Fatigue Life of Carbon and Low-Alloy Steels in LWR Water Environment,” Fatigue and Crack Growth: Environmental Effects, Modeling Studies, and Design Considerations, PVP Vol. 306, S. Yukawa, ed., American Society of Mechanical Engineers, New York, pp. 123-128, 1995.

15. Higuchi, M., K. Iida, and Y. Asada, “Effects of Strain Rate Change on Fatigue Life of Carbon Steel in High-Temperature Water,” Proc. of Symp. on Effects of the Environment on the Initiation of Crack Growth, ASTM STP 1298, American Society for Testing and Materials, Philadelphia, 1997.

16. Higuchi, M., K. Iida, and K. Sakaguchi, “Effects of Strain Rate Fluctuation and Strain Holding on Fatigue Life Reduction for LWR Structural Steels in Simulated PWR Water,” Pressure Vessel and Piping Codes and Standards, PVP Vol. 419, M. D. Rana, ed., American Society of Mechanical Engineers, New York, pp. 143-152, 2001.

17. Hirano, A., M. Yamamoto, K. Sakaguchi, T. Shoji, and K. Iida, “Effects of Water Flow Rate on Fatigue Life of Ferritic and Austenitic Steels in Simulated LWR Environment,” Pressure Vessel and Piping Codes and Standards - 2002, PVP Vol. 439, M. D. Rana, ed., American Society of Mechanical Engineers, New York, pp. 143-150, 2002.

18. Hirano, A., M. Yamamoto, K. Sakaguchi, and T. Shoji, “Effects of Water Flow Rate on Fatigue Life of Carbon and Stainless Steels in Simulated LWR Environment,” Pressure Vessel and Piping Codes and Standards - 2004, PVP Vol. 480, American Society of Mechanical Engineers, New York, pp. 109-119, 2004.

19. Higuchi, M., and K. Iida, “Reduction in Low-Cycle Fatigue Life of Austenitic Stainless Steels in High-Temperature Water,” Pressure Vessel and Piping Codes and Standards, PVP Vol. 353, D. P. Jones, B. R. Newton, W. J. O'Donnell, R. Vecchio, G. A. Antaki, D. Bhavani, N. G. Cofie, and G. L. Hollinger, eds., American Society of Mechanical Engineers, New York, pp. 79-86, 1997.

20. Tsutsumi, K., H. Kanasaki, T. Umakoshi, T. Nakamura, S. Urata, H. Mizuta, and S. Nomoto, “Fatigue Life Reduction in PWR Water Environment for Stainless Steels,” Assessment Methodologies for Preventing Failure: Service Experience and Environmental Considerations, PVP Vol. 410-2, R. Mohan, ed., American Society of Mechanical Engineers, New York, pp. 23-34, 2000.

21. Tsutsumi, K., T. Dodo, H. Kanasaki, S. Nomoto, Y. Minami, and T. Nakamura, “Fatigue Behavior of Stainless Steel under Conditions of Changing Strain Rate in PWR Primary Water,” Pressure Vessel and Piping Codes and Standards, PVP Vol. 419, M. D. Rana, ed., American Society of Mechanical Engineers, New York, pp. 135-141, 2001.

22. Tsutsumi, K., M. Higuchi, K. Iida, and Y. Yamamoto, “The Modified Rate Approach to Evaluate Fatigue Life under Synchronously Changing Temperature and Strain Rate in Elevated Temperature Water,” Pressure Vessel and Piping Codes and Standards - 2002, PVP Vol. 439, M. D. Rana, ed., American Society of Mechanical Engineers, New York, pp. 99-107, 2002.

23. Chopra, O. K., “Effects of LWR Coolant Environments on Fatigue Design Curves of Austenitic Stainless Steels,” NUREG/CR-5704, ANL-98/31, 1999.

24. Chopra, O. K., and W. J. Shack, "Review of the Margins for ASME Code Design Curves - Effects of Surface Roughness and Material Variability," NUREG/CR-6815, ANL-02/39, Sept. 2003.

25. Chopra, O. K., B. Alexandreanu, and W. J. Shack, "Effect of Material Heat Treatment on Fatigue Crack Initiation in Austenitic Stainless Steels in LWR Environments," NUREG/CR-6878, ANL-03/35, July 2005.

26. Terrell, J. B., "Effect of Cyclic Frequency on the Fatigue Life of ASME SA-106-B Piping Steel in PWR Environments," J. Mater. Eng. **10**, 193-203, 1988.

27. Lenz, E., N. Wieling, and H. Muenster, "Influence of Variation of Flow Rates and Temperature on the Cyclic Crack Growth Rate under BWR Conditions," Environmental Degradation of Materials in Nuclear Power Systems - Water Reactors, The Metallurgical Society, Warrendale, PA, 1988.

28. Garud, Y. S., S. R. Paterson, R. B, Dooley, R. S. Pathania, J. Hickling, and A. Bursik, "Corrosion Fatigue of Water Touched Pressure Retaining Components in Power Plants," EPRI TR-106696, Final Report, Electric Power Research Institute, Palo Alto, Nov. 1997.

29. Kilian, R., J. Hickling, and R. Nickell, "Environmental Fatigue Testing of Stainless Steel Pipe Bends in Flowing, Simulated PWR Primary Water at 240°C," Third Intl. Conf. Fatigue of Reactor Components, MRP-151, Electric Power Research Institute, Palo Alto, CA, Aug. 2005.

30. Amzallag, C., P. Rabbe, G. Gallet, and H.-P. Lieurade, "Influence des Conditions de Sollicitation sur le Comportement en Fatigue Oligocyclique d'Aciers Inoxydables Austénitiques," Memoires Scientifiques Revue Metallurgie, pp. 161-173, 1978.

31. Solomon, H. D., C. Amzallag, A. J. Vallee, and R. E. De Lair, "Influence of Mean Stress on the Fatigue Behavior of 304L SS in Air and PWR Water," Proc. of the 2005 ASME Pressure Vessels and Piping Conf., July 17-21, 2005, Denver, CO, paper # PVP2005-71064.

32. Solomon, H. D., C. Amzallag, R. E. De Lair, and A. J. Vallee, "Strain Controlled Fatigue of Type 304L SS in Air and PWR Water," Proc. Third Intl. Conf. on Fatigue of Reactor Components, Seville, Spain, Oct. 3-6, 2004.

33. Jaske, C. E., and W. J. O'Donnell, "Fatigue Design Criteria for Pressure Vessel Alloys," Trans. ASME J. Pressure Vessel Technol. **99**, 584-592, 1977.

34. Mehta, H. S., "An Update on the EPRI/GE Environmental Evaluation Methodology and its Applications," Probabilistic and Environmental Aspects of Fracture and Fatigue, PVP Vol. 386, S. Rahman, ed., American Society of Mechanical Engineers, New York, pp. 183-193, 1999.

35. Van Der Sluys, W. A., "PVRC's Position on Environmental Effects on Fatigue Life in LWR Applications," Welding Research Council Bulletin 487, Welding Research Council, Inc., New York, Dec. 2003.

36. O'Donnell, W. J., W. J. O'Donnell, and T. P. O'Donnell, "Proposed New Fatigue Design Curves for Austenitic Stainless Steels, Alloy 600, and Alloy 800," Proc. of the 2005 ASME Pressure Vessels and Piping Conf., July 17-21, 2005, Denver, CO, paper # PVP2005-71409.

37. Johnson, L. G., “The Median Ranks of Sample Values in Their Population with an Application to Certain Fatigue Studies,” Ind. Math. **2**, 1-9, 1951.

38. Lipson, C., and N. J. Sheth, Statistical Design and Analysis of Engineering Experiments, McGraw Hill, New York, 1973.

39. Kooistra, L. F., E. A. Lange, and A. G. Pickett, “Full-Size Pressure Vessel Testing and Its Application to Design,” J. Eng. Power **86**, 419-428, 1964.

40. Manjoine, M. J., “Fatigue Damage Models for Annealed Type 304 Stainless Steel under Complex Strain Histories,” Trans. 6th Intl. Conf. on Structural Mechanics in Reactor Technology (SMiRT), Vol. L, 8/1, North-Holland Publishing Co., pp. 1-13, 1981.

41. Nian, L., and Du Bai-Ping, “The Effect of Low-Stress High-Cycle Fatigue on the Microstructure and Fatigue Threshold of a 40Cr Steel,” Int. J. Fatigue **17** (1), 43-48, 1995.

42. Haibach, E., and D. Schutz, “Fatigue Life Evaluation with Particular Attention to Local Strain and Stress Time Histories,” Proc. Inst. Mech. Eng., 1974.

43. USNRC Generic Letter 94-03, “Intergranular Stress Corrosion Cracking of Core Shrouds in Boiling Water Reactors,” U.S. Nuclear Regulatory Commission, July 25, 1994.

44. USNRC Information Notice 92-57, “Radial Cracking of Shroud Support Access Hole Cover Welds,” U.S. Nuclear Regulatory Commission, August 11, 1992.

45. USNRC IE Bulletin No. 80-07, “BWR Jet Pump Assembly Failure,” U.S. Nuclear Regulatory Commission, April 4, 1980.

46. USNRC Information Notice 93-101, “Jet Pump Hold-Down Beam Failure,” U.S. Nuclear Regulatory Commission, December 17, 1993.

47. USNRC Information Notice 97-02, “Cracks Found in Jet Pump Riser Assembly Elbows at Boiling Water Reactors,” U.S. Nuclear Regulatory Commission, February 6, 1997.

48. USNRC Information Notice 95-17, “Reactor Vessel Top Guide and Core Plate Cracking,” U.S. Nuclear Regulatory Commission, March 10, 1995.

49. NUREG-1544, “Status Report: Intergranular Stress Corrosion Cracking of BWR Core Shrouds and Other Internal Components,” U.S. Nuclear Regulatory Commission, March, 1996.

50. USNRC Information Notice 98-11, “Cracking of Reactor Vessel Internal Baffle Former Bolts in Foreign Plants,” U.S. Nuclear Regulatory Commission, March 25, 1998.

51. Jacobs, A. J., G. P. Wozadlo, K. Nakata, T. Yoshida, and I. Masaoka, “Radiation Effects on the Stress Corrosion and Other Selected Properties of Type-304 and Type-316 Stainless Steels,” Proc. 3rd Intl. Symp. Environmental Degradation of Materials in Nuclear Power Systems - Water Reactors, G. J. Theus and J. R. Weeks, eds., The Metallurgical Society, Warrendale, PA, pp. 673-680, 1988.

52. Garzarolli, F., D. Alter, P. Dewes, and J. L. Nelson, "Deformability of Austenitic Stainless Steels and Ni-Base Alloys," Proc. 3th Intl. Symp. on Environmental Degradation of Materials in Nuclear Power Systems - Water Reactors, G. J Theus and J. R. Weeks, eds., The Metallurgical Society, Warrendale, PA, pp. 657-664, 1988.

53. Bruemmer, S. M., and G. S. Was, "Microstructural and Microchemical Mechanisms Controlling Intergranular Stress Corrosion Cracking in Light-Water-Reactor Systems," J. Nucl. Mater. **216,** 348-363, 1994.

54. Scott, P., "A Review of Irradiation Assisted Stress Corrosion Cracking," J. Nucl. Mater. **211**, 101-122, 1994.

55. Osozawa, K., and H. J. Engell, "The Anodic Polarization Curves of Iron-Nickel-Chromium Alloys," Corr. Sci. **6**, 389-393, 1966.

56. Tedmon, C. S., Jr., D. A. Vermilyea, and J. H. Rosolowski, "Intergranular Corrosion of Austenitic Stainless Steel," J. Electrochem. Soc. **118**, 192-202, 1971.

57. Bruemmer, S. M., L. A. Charlot, and D. G. Atteridge, "Sensitization Development in Austenitic Stainless Steel - Measurement and Prediction of Thermomechanical History Effects," Corrosion **44**, 427, 1987.

58. Andresen, P. L., F. P. Ford, S. M. Murphy, and J. M. Perks, "State of Knowledge of Radiation Effects on Environment Cracking in Light Water Reactor Core Materials," Proc. 4th Intl. Symp. on Environmental Degradation of Materials in Nuclear Power Systems - Water Reactors, NACE, Houston, TX, pp. 1.83-1.121, 1990.

59. Chung, H. M., W. R. Ruther, and R. V. Strain, "Irradiation-Assisted Stress Corrosion Cracking of Model Austenitic Stainless Steels Irradiated in the Halden Reactor," NUREG/CR-5608, ANL-98/25, March 1999.

60. Chung, H. M., W. R. Ruther, R. V. Strain, and W. J. Shack, "Irradiation-Assisted Stress Corrosion Cracking of Model Austenitic Stainless Steel Alloys," NUREG/CR-6687, ANL-00/21, Oct. 2000.

61. Chung, H. M., W. R. Ruther, and R. V. Strain, "Irradiation-Assisted Stress Corrosion Cracking Behavior of Austenitic Stainless Steels Applicable to LWR Core Internals," NUREG/CR-6892, ANL-04/10, Jan. 2006.

62. Chung, H. M., and R. W. Strain, "Slow-Strain-Rate-Tensile Test of Model Austenitic Stainless Steels Irradiated in the Halden Reactor," Environmentally Assisted Cracking in Light Water Reactors, Annual Report, January-December 2003, NUREG/CR-4667 Vol. 34, ANL-05/17, May 2006.

63. Was, G. S., "Recent Developments in Understanding Irradiation Assisted Stress Corrosion Cracking," Proc. 11th Int. Symp. on Environmental Degradation of Materials in Nuclear Power Systems - Water Reactors, Stevenson, WA, pp. 965-985, 2003.

64. Gertsman, V. Y., and K. Tangri, "Grain Boundary Distributions, Texture and Orientation Correlations in Austenitic Stainless Steels," Scripta Metall. et Mater. **33** (7), 1037-1042, 1995.

65. Lin, P., G. Palumbo, U. Erb, and K. T. Aust, "Influence of Grain Boundary Character Distribution on Sensitization and Intergranular Corrosion of Alloy 600," Scripta Metall. et Mater. **33** (9), 1387-1392, 1995.

66. Was, G. S., B. Alexandreanu, P. Andresen, and M. Kumar, "Role of Coincident Site Lattice Boundaries in Creep and Stress Corrosion Cracking," Interfacial Engineering for Optimized Properties III, Materials Research Society Symposium Proceedings, Vol. 819, pp. 87-100, 2004.

67. Bruemmer, S. M., et al., "Critical Issue Reviews for the Understanding and Evaluation of Irradiation-Assisted Stress Corrosion Cracking," EPRI TR-107159, Electric Power Research Institute, Palo Alto, CA, 1996.

68. Herrera, M. L., et al., "Evaluation of the Effects of Irradiation on the Fracture Toughness of BWR Internal Components," Proc. ASME/JSME 4th Intl. Conf. on Nucl. Eng. (ICONE-4), Vol. 5, A. S. Rao, R. M. Duffey, and D. Elias, eds., American Society of Mechanical Engineers, New York, pp. 245-251, 1996.

69. Mills, W. J., "Fracture Toughness of Type 304 and 316 Stainless Steels and their Welds," Intl. Mater. Rev. **42**, 45-82, 1997.

70. Kanasaki, H., I. Satoh, M. Koyama, T. Okubo, T. R. Mager, and R. G. Lott, "Fatigue and Stress Corrosion Cracking Behaviors of Irradiated Stainless Steels in PWR Primary Water," Proc. 5th Intl. Conf. on Nuclear Engineering, ICONE5-2372, pp. 1-7, 1997.

71. Jenssen, A., and L. G. Ljungberg, "Irradiation Assisted Stress Corrosion Cracking of Stainless Alloys in BWR Normal Water Chemistry and Hydrogen Water Chemistry," Proc. Sixth Intl. Symp. on Environmental Degradation of Materials in Nuclear Power Systems - Water Reactor, R. E. Gold and E. P. Simonen, eds., Minerals, Metals & Materials Society, Warrendale, PA, pp. 547-553, 1993.

72. Brown, K. S., and G. M. Gordon, "Effects of BWR Coolant Chemistry on the Propensity for IGSCC Initiation and Growth in Creviced Reactor Internals Components," Proc. Third Intl. Symp. on Environmental Degradation of Materials in Nuclear Power Systems - Water Reactor, AIME, Littleton, CO, pp. 243-248, 1987.

73. Gordon, G. M., and K. S. Brown, "Dependence of Creviced BWR Component IGSCC Behavior on Coolant Chemistry," Proc. 4th Intl. Symp. on Environmental Degradation of Materials in Nuclear Power Systems - Water Reactor, Daniel Cubicciotti, ed., NACE, Houston, TX, pp. 14.46-14.61, 1990.

74. Garzarolli, F., D. Alter, and P. Dewes, "Deformability of Austenitic Stainless Steels and Nickel-Base Alloys in the Core of a Boiling and a Pressurized Water Reactor," Proc. Intl. Symp. on Environmental Degradation of Materials in Nuclear Power Systems - Water Reactor, American Nuclear Society, La Grange Park, IL, pp. 131-138, 1986.

75. Kodama, M., et al., "IASCC Susceptibility of Austenitic Stainless Steels Irradiated to High Neutron Fluence," Proc. Sixth Intl. Symp. on Environmental Degradation of Materials in Nuclear Power Systems - Water Reactor, R. E. Gold and E. P. Simonen, eds., Minerals, Metals & Materials Society, Warrendale, PA, pp. 583-588, 1993.

76. Kodama, M., et al., "Effects of Fluence and Dissolved Oxygen on IASCC in Austenitic Stainless Steels," Proc. Fifth Intl. Symp. on Environmental Degradation of Materials in Nuclear Power Systems - Water Reactor, American Nuclear Society, La Grange Park, IL, pp. 948-954, 1991.

77. Clark, W. L., and A. J. Jacobs, "Effect of Radiation Environment on SCC of Austenitic Materials," Proc. First Intl. Symp. on Environmental Degradation of Materials in Nuclear Power Systems - Water Reactor, NACE, Houston, TX, p. 451, 1983.

78. Andresen, P. L., and F. P. Ford, "Irradiation Assisted Stress Corrosion Cracking: From Modeling and Prediction of Laboratory & In-Core Response to Component Life Prediction," Corrosion/95, NACE, Houston TX, Paper No. 419, 1995.

79. Jenssen, A., and L. G. Ljungberg, "Irradiation Assisted Stress Corrosion Cracking: Post Irradiation CERT Tests of Stainless Steels in a BWR Test Loop," Proc. Seventh Intl. Symp. on Environmental Degradation of Materials in Nuclear Power Systems - Water Reactor, G. Airey et al., eds., NACE, Houston, TX, pp. 1043-1052, 1995.

80. Chopra, O. K., E. E. Gruber, and W. J. Shack, "Fracture Toughness and Crack Growth Rates of Austenitic Stainless Steels," NUREG/CR-6826, ANL-03/22, Aug. 2004.

81. Chopra, O. K., B. Alexandreanu, E. E. Gruber, R. S. Daum, and W. J. Shack, "Crack Growth Rates of Irradiated Austenitic Stainless Steel Weld Heat Affected Zone in BWR Environments," NUREG/CR-6891, ANL-04/20, Jan. 2006.

82. Hazelton, W. S., and W. H. Koo, "Technical Report on Material Selection and Processing Guidelines for BWR Coolant Pressure Boundary Piping, Final Report," NUREG-0313, Rev. 2, 1988.

83. Gruber, E. E., and O. K. Chopra, "Crack Growth Rate Test of Austenitic Stainless Steels Irradiated in the Halden Reactor," Environmentally Assisted Cracking in Light Water Reactors, Annual Report, January-December 2003, NUREG/CR-4667, Vol. 34, ANL-05/17, pp. 32-61, 2005.

84. Chung, H. M., and W. J. Shack, "Irradiation-Assisted Stress Corrosion Cracking Behavior of Austenitic Stainless Steels Applicable to LWR Core Internals," NUREG/CR-6892, ANL-04/10, Jan. 2006.

85. Odette, G. R., and G. E. Lucas, "The Effects of Intermediate Temperature Irradiation on the Mechanical Behavior of 300-Series Austenitic Stainless Steels," J. Nucl. Mater. **179-181**, 572-576, 1991.

86. James, L. A., and D. P. Jones, "Fatigue Crack Growth Correlation for Austenitic Stainless Steels in Air," Proc. Conf. on Predictive Capabilities in Environmentally-Assisted Cracking, PVP Vol. 99, R. Rungta, ed., American Society of Mechanical Engineers, New York, pp. 363-414, 1985.

87. Shack, W. J., and T. F. Kassner, "Review of Environmental Effects on Fatigue Crack Growth of Austenitic Stainless Steels," NUREG/CR-6176, ANL-94/1, May 1994.

88. Andresen, P. L., "Similarity of Cold Work and Radiation Hardening in Enhancing Yield Strength and SCC Growth of Stainless Steel in Hot Water," Corrosion/02, NACE, Houston, TX, Paper No. 02509, 2002.

89. Gruber, E. E., and O. K. Chopra, "Crack Growth Rate Test of Austenitic Stainless Steels Irradiated in the Halden Reactor," Environmentally Assisted Cracking in Light Water Reactors, Annual Report, January-December 2004, NUREG/CR-4667, Vol. 35, ANL-05/31, pp. 27-55, 2006.

90. Andresen, P. L., T. M. Angeliu, W. R. Catlin, L. M. Young, and R. M. Horn, "Effect of Deformation on SCC of Unsensitized Stainless Steel," Corrosion/2000, NACE, Houston, TX, Paper No. 00203, 2000.

91. Angeliu, T. M., P. L. Andresen, E. Hall, J. A. Sutliff, and S. Sitzman, "Strain and Microstructure Characterization of Austenitic Stainless Steel Weld HAZs," Corrosion/2000, NACE, Houston, TX, Paper No. 00186, 2000.

92. Andresen, P. L., T. M. Angeliu, L. M. Young, W. R. Catlin, and R. M. Horn, "Mechanism and Kinetics of SCC in Stainless Steels," Proc. Tenth Intl. Symp. on Environmental Degradation of Materials in Nuclear Power Systems - Water Reactor, NACE, Houston, TX, 2001.

93. Garzarolli, F., H. Rubel, and E. Steinberg, "Behavior of Water Reactor Core Materials with Respect to Corrosion Attack," Proc. 3th Intl. Symp. on Environmental Degradation of Materials in Nuclear Power Systems - Water Reactors, Myrtle Beach, South Carolina, August 22-25, 1983, NACE, Houston, TX, pp. 1-24, 1984.

94. Bruemmer, S. M., J. I. Cole, F. A. Garner, and L. R. Greenwood, "Critical Issue Reviews for the Understanding and Evaluation of Irradiation-Assisted Stress Corrosion Cracking," EPRI TR-107159, pp. 3-9, Nov. 1996.

95. Berge, Ph., and F. de Keroulas, "The Present Situation Regarding Environmental Degradation of Components in Pressurized Water Reactors," Proc. 4th Int. Symp. on Environmental Degradation of Materials in Nuclear Power Systems - Water Reactors, NACE, Houston, TX, pp. 1-11, 1990.

96. Andresen, P. L., F. P. Ford, S. M. Murphy, and J. M. Perks, "State of Knowledge of Radiation Effects on Environmental Cracking in Light Water Reactor Core Materials," Proc. 4th Intl. Symp. on Environmental Degradation of Materials in Nuclear Power Systems - Water Reactors, NACE, Houston, TX, pp. 1.83-1.121, 1990.

97. Scott, P., "A Review of Irradiation Assisted Stress Corrosion Cracking", J. Nucl. Mater. **211**, 101-122, 1994.

98. Mansur, L. K., "Theory and Experimental Background on Dimensional Changes in Irradiated Alloys," J. Nucl. Mater. **216**, 97-123, 1994.

99. Garner, F. A., "Irradiation Performance of Cladding and Structural Steels in Liquid Metal Reactors," Materials Science and Technology - A Comprehensive Treatment, R.W. Cahn, P. Haasen, E. J. Kramer, eds., VCH Publishers Inc., New York, 1994.

100. Garner, F. A., and M. B. Toloczko, "Irradiation Creep and Void Swelling of Austenitic Stainless Steels at Low Displacement Rates in Light Water Energy Systems," J. Nucl. Mater. **251**, 252-261, 1997.

101. Chung, H. M., "Assessment of Void Swelling in Austenitic Stainless Steel Core Internals," NUREG/CR-6897, ANL-04/28, Jan. 2006.

102. Electric Power Research Institute, "CIR II Program: Description of the Boris 6 Experiment in the BOR-60 Fast Breeder Reactor," Report No. 1009418, EPRI, Palo Alto, CA, 2004.

103. Lucas, G. E., J. W. Sheckherd, G. R. Odette, and S. Panchanadeeswaran, "Shear Punch Tests for Mechanical Property Measurements in TEM Disc-Sized Specimens," J. Nucl. Mater. **122&123**, 429-434, 1984.

104. Hankin, G. L., M. B. Toloczko, M. J. Hamilton, F. A. Garner, and R. G. Faulkner, "Shear Punch Testing of 59Ni Isotopically-Doped Model Austenitic Alloys after Irradiation in FFTF at Different He/dpa Ratios," J. Nucl. Mater. **258-263**, 1657-1663, 1998.

105. Hankin, G. L., M. B. Toloczko, M. J. Hamilton, and R. G. Faulkner "Validation of the Shear Punch-Tensile Correlation Technique using Irradiated Materials," J. Nucl. Mater. **258-263**, 1651-1656, 1998.

106. Toloczko, M. B., M. L. Hamilton, and G. E. Lucas, "Ductility Correlations between Shear Punch and Uniaxial Tensile Test Data," J. Nucl. Mater. **283-287**, 987-991, 2000.

107. Toloczko, M. B, R. J. Kurtz, A. Hasegawa, and K. Abe, "Shear Punch Tests Performed Using a New Low Compliance Test Fixture," J. Nucl. Mater. **307-311**, 1619-1623, 2002.

108. Hamilton, M. L., F. A. Garner, M. B. Toloczko, S. A. Maloy, W. F. Sommer, M. R. James, P. D. Ferguson, and M. R. Louthan Jr., "Shear Punch and Tensile Measurements of Mechanical Property Changes Induced in Various Austenitic Alloys by High-Energy Mixed Proton and Neutron irradiation at Low Temperatures," J. Nucl. Mater. **283-287**, 418-422, 2000.

109. Manahan, M. P., A. S. Argon, and O. K. Harling, "The Development of a Miniaturized Disk Bend Test for the Determination of Postirradiation Mechanical Properties," J. Nucl. Mater. **103&104**, 1545-1550, 1981.

110. Huang, F. H., M. L. Hamilton, and G. L. Wire, "Bend Testing for Miniature Disks," Nucl. Tech. **57**, 234-242, 1982.

111. Jia, X., and Y. Dai, "Small Punch Tests on Martensitic/Ferritic Steels F82H, T91 and Optimax-A Irradiated in SINQ Target-3," J. Nucl. Mater. **323**, 360-367, 2003.

112. Mao, X., and H. Takahashi, "Development of a Further-Miniaturized Specimen of 3 mm Diameter for TEM Disk (ϕ=3 mm) Small Punch Tests," J. Nucl. Mater. **150**, 42-52, 1987.

113. Murty, K. L, M. D. Mathew, P. Q. Miraglia, F. M. Haggag, and V. N. Shah, "Application of Automated-Ball-Indentation Technique in Assessing Tensile and Fracture Properties of Reactor Pressure Vessel Weldment," EPRI Report PC-110202, EPRI Reactor Pressure Vessel Inspection Conference, Santa Fe, New Mexico, June 22-24, 1998.

114. Murty K. L, P. Q. Miraglia, M. D. Mathew, V. N. Shah, and F. M.Haggag, "Characterization of Gradients in Mechanical Properties of SA-533B Steel Welds Using Ball Indentation," Int. J. of Press. Vess. Piping **76**, 361-369, 1999.

115. Haggag, F. M., "Effects of Irradiation Temperature on Embrittlement of Nuclear Pressure Vessel Steels," Effects of Radiation on Materials: 16th International Symposium, ASTM STP 1175, Arvind S. Kumar, David S. Gelles, Randy K. Nanstad, and Edward A. Little, eds., American Society for Testing and Materials, Philadelphia, 1993.

116. Bayoumi, M. R., and M. N. Bassim, "Experimental Correlation between Ductility and J-Integral in the Transition Region of 1045 Steel," Eng. Fract. Mech. **18** (3), 679-69, 1983.

117. Mao, X., M. Saito, and H. Takahashi, "Small Punch Test to Predict Ductile Fracture Toughness J_{IC} and Brittle Fracture Toughness K_{IC}," Scripta Metal. **25**, 2481-2485, 1991.

118. Foulds, J. R., R. J. Woyowitz, T. K. Parnell, C. W. Jewett, and A. H. Kadarman, "Small Punch Testing for Fracture Toughness Measurement," EPRI, TR-105130, Palo Alto, CA, 1995.

119. Foulds, J. R., "Small Punch Testing for Irradiation Embrittlement," EPRI, TR-105131, Palo Alto, CA, 1995.

120. Shinohara, K., G. E. Lucas, and G. R. Odette, "Shear Punch and Ball Microhardness Measurements of 14 MeV Neutron Irradiation Hardening in Five Metals," J. Nucl. Mater. **133&134**, 326-331, 1985.

121. Byrne, S., F. A. Garner, S. Fyfitch, and I. L. Wilson, "Application of Void Swelling Data to Evaluation of Pressurized Water Reactor Components," Proc. 10th Intl. Conf. on Environmental Degradation of Materials in Nuclear Power Systems - Water Reactors, NACE/ANS/TMS, Aug. 5-9, 2001, Lake Tahoe, NV.

122. Edwards, D. J., F. A. Garner, B. A. Oliver, and S. M. Bruemmer, "Microstructural Evaluation of a Cold-Worked 316SS Baffle Bolt Irradiated in a Commercial PWR," Proc. 10th Intl. Conf. on Environmental Degradation of Materials in Nuclear Power Systems - Water Reactors, NACE/ANS/ TMS, Aug. 5-9, 2001, Lake Tahoe, NV.

123. Thomas, L., and S. Bruemmer, "Analytical Transmission Microscopy (ATEM) Characterization of Stress Corrosion Cracks in LWR-Irradiated Austenitic Stainless Steel Components," EPRI-1003422, Electric Power Research Institute, Palo Alto, CA, May 2002.

124. Garner, F. A., B. M. Oliver, L. B. Greenwood, D. J. Edwards, S. Bruemmer, and M. L. Grossbeck, "Generation and Retention of Helium and Hydrogen in Austenitic Steels Irradiated in a Variety of LWR and Test-Reactor Spectral Environments," Proc. 10th Intl. Conf. on Environmental Degradation of Materials in Nuclear Power Systems - Water Reactors, NACE/ANS/TMS, Aug. 5-9, 2001, Lake Tahoe, NV.

125. Fujii, K., K. Fukuya, G. Furutani, T. Torimaru, A. Kohyama, and Y. Katoh, "Swelling in 316 Stainless Steel Irradiated to 53 dpa in a PWR," Proc. 10th Intl. Conf. on Environmental Degradation of Materials in Nuclear Power Systems - Water Reactors, NACE/ANS/TMS, Aug. 5-9, 2001, Lake Tahoe, NV.

126. Foster, J. P., D. L. Potter, D. L. Harrod, T. R. Mager, and M. G. Burke, "316 Stainless Steel Cavity Swelling in a PWR," J. Nucl. Mater. **224**, 207, 1995.

127. Allen, T. R., H. Tsai, R. S. Daum, D. L. Porter, J. I. Cole, T. Yoshitake, N. Akasaka, T. Donomae, S. Mizuta, J. Ohta, K. Dohi, and H. Kusanagi, "Effects of Irradiation on the Swelling and Mechanical Properties of 316 Stainless Steel," Proc. 11th Intl. Conf. on Environmental Degradation of Materials in Nuclear Power Systems - Water Reactors, Aug. 10-14, 2003, Stevenson, WA, pp. 911-919, 2003.

128. Chung, H. M., R. V. Strain, and W. J. Shack, "Tensile and Stress Corrosion Cracking of Type 304 Stainless Steel Irradiated to Very High Dose," Nucl. Eng. Des. **208**, 221-234, 2001.

129. Scott, P., "An Analysis of Primary Water Stress Corrosion Cracking in PWR Steam Generators," Proc. of the Specialists Meeting on Operating Experience with Steam Generators, Brussels, Belgium, pp. 5-6, 1991.

130. Cattant, F., "Lessons learned from the examination of tubes pulled from Electricite de France steam generators," Nucl. Eng. Des. **168**, 241-253, 1997.

131. Diercks, D. R., W. J. Shack, and J. Muscara, "Overview of Steam Generator Tube Degradation and Integrity Issues," Nucl. Eng. Des. **194**, 19-30, 1999.

132. USNRC Information Notice No. 90-10, "Primary Water Stress Corrosion Cracking (PWSCC) of Inconel 600," Feb. 1990.

133. USNRC Generic Letter 97-01, "Degradation of Control Rod Drive Mechanism and Other Vessel Closure Head Penetrations," April 1, 1997.

134. Economou, J., A. Assice, F. Cattant, J. Salin, and M. Stindel, "NDE and Metallurgical Examination of Vessel Head Penetrations," 3rd Intl. Symp. of Fontevraud, Sept. 12-16, 1994.

135. Robinson, M. R., "Oconee Unit 1 and Unit 3 Reactor Vessel Head Leakage, Cracking of RV Head Penetrations due to Primary Water Stress Corrosion Cracking," presented at the NRC Meeting with the NEI EPRI Material Reliability Program Regarding CRDM Nozzle Crackling Issues, Rockville, MD, April 2001.

136. Frye, C. R., T. Alley, M. L. Arey, Jr., and M. R. Robinson, "Cracking in Alloy 600/182 Reactor Vessel Head Penetrations," PVP-Vol. 437, Service Experience and Failure Assessment Applications, P. S. Lam, ed., American Society of Mechanical Engineers, New York, pp. 171-178, 2002.

137. USNRC Information Notice 2001-05, "Through-Wall Circumferential Cracking of Reactor Pressure Vessel Head Control Rod Drive Mechanism Penetration Nozzle at Oconee Nuclear Station, Unit 3," April 30, 2001.

138. USNRC Bulletin 2001-01, "Circumferential Cracking of Reactor Pressure Vessel Head Penetration Nozzles," Aug. 3, 2001.

139. USNRC Information Notice 2000-17, "Crack in Weld Area of Reactor Coolant System Hot Leg Piping at V. C. Summer," Oct. 18, 2000; Suppl. 1, Nov. 16, 2000; Suppl. 2, Feb. 28, 2001.

140. Jenssen, A., K. Norrgard, J. Lagerstrom, G. Embring, and D. Tice, "Assessment of Cracking in Dissimilar Metal Welds," Proc. of the Tenth Intl. Conf. on Environmental Degradation of Materials in Nuclear Power Systems - Water Reactors, NACE International, Houston, TX, 2001.

141. Bennetch, J. I., G. E. Modzelewski, L. L. Spain, and G. V. Rao, "Root Cause Evaluation and Repair of Alloy 82/182 J-Groove Weld Cracking of Reactor Vessel Head Penetrations at North Anna Unit 2," PVP-Vol. 437, Service Experience and Failure Assessment Applications, P. S. Lam, ed., American Society of Mechanical Engineers, New York, pp. 179-185, 2002.

142. USNRC Information Notice 2002-11, "Recent Experience with Degradation of Reactor Pressure Vessel Head," March 12, 2002.

143. USNRC Information Notice 2003-11, "Leakage Found on Bottom-Mounted Instrumentation Nozzles," Aug. 13, 2003; Suppl. 1, Jan. 8, 2004.

144. USNRC Bulletin 2003-02, "Leakage from Reactor Pressure Vessel Lower Head Penetrations and Reactor Coolant Pressure Boundary Integrity," Aug. 21, 2003.

145. Ruther, W. E., W. K. Soppet, and T. F. Kassner, "Corrosion Fatigue of Alloys 600 and 690 in Simulated LWR Environments," NUREG/CR-6383, ANL-95/37, April 1996.

146. Ruther, W. E., W. K. Soppet, and T. F. Kassner, "Environmentally Assisted Cracking of Alloys 600 and 690 in Simulated LWR Water," Environmentally Assisted Cracking in Light Water Reactors, Semiannual Report, July 1997-December 1997, NUREG/CR-4667, Vol. 25, ANL-98/18, pp. 42-75, Sept. 1998.

147. Ruther, W. E., W. K. Soppet, T. F. Kassner, and W. J. Shack, "Environmentally Assisted Cracking of Alloys 600 and 690 in Simulated LWR Water," Environmentally Assisted Cracking in Light Water Reactors, Semiannual Report, January 1998-July 1998, NUREG/CR-4667, Vol. 26, ANL-98/18, pp. 25-32, March 1999.

148. Ruther, W. E., W. K. Soppet, T. F. Kassner, and W. J. Shack, "Environmentally Assisted Cracking of Alloys 600 and 690 in Simulated LWR Water," Environmentally Assisted Cracking in Light Water Reactors, Semiannual Report, July 1998-December 1998, NUREG/CR-4667, Vol. 27, ANL-99/11, pp. 45-54, Oct. 1999.

149. Soppet, W. K., O. K. Chopra, and W. J. Shack, "Environmentally Assisted Cracking of Alloys 600 and 690 in Simulated LWR Water," Environmentally Assisted Cracking in Light Water Reactors, Semiannual Report, July 1999-December 1999, NUREG/CR-4667, Vol. 29, ANL-00/23, pp. 39-45, Nov. 2000.

150. Chopra, O. K., W. K. Soppet, and W. J. Shack, "Effects of Alloy Chemistry, Cold Work, and Water Chemistry on Corrosion Fatigue and Stress Corrosion Cracking of Nickel Alloys and Welds," NUREG/CR-6721, ANL-01/07, April 2001.

151. Cassagne, T. B., and A. Gelpi, "Crack Growth Rate Measurements on Alloy 600 Steam Generator Tubes in Steam and Primary Water," Proc. of the Fifth Intl. Symp. on Environmental Degradation of Materials in Nuclear Power Systems - Water Reactors, American Nuclear Society, La Grange Park, IL, pp. 518-524, 1991.

152. Foster, J. P., W. H. Bamford, and R. S. Pathania, "Initial Results of Alloy 600 Crack Growth Rate Testing in a PWR Environment," Proc. of the Seventh Intl. Symp. on Environmental Degradation of Materials in Nuclear Power Systems - Water Reactors, NACE International, Houston, TX, pp. 25-39, 1995.

153. Magdowski, R., F. Vaillant, C. Amzallag, and M. O. Speidel, "Stress Corrosion Crack Growth Rates of Alloy 600 in Simulated PWR Coolant," Proc. of the 8th Intl. Symp. on Environmental Degradation of Materials in Nuclear Power Systems - Water Reactors, S. M. Bruemmer, ed., American Nuclear Society, La Grange Park, IL, pp. 333-338, 1997.

154. Le Hong, S., C. Amzallag, and A. Gelpi, "Modeling of Stress Corrosion Crack Initiation on Alloy 600 in Primary Water of PWRs," Proc. of the Ninth Intl. Symp. on Environmental Degradation of Materials in Nuclear Power Systems - Water Reactors, F. P. Ford, S. M. Bruemmer, and G. S. Was, eds., The Minerals, Metals, and Materials Society, Warrendale, PA, pp. 115-122, 1999.

155. Raquet, O., and G. Santarini, "Stress Corrosion Crack Propagation Rate of Alloy 600 in the Primary Water of PWR Influence of a Cold Worked Layer," Proc. of the Ninth Intl. Symp. on Environmental Degradation of Materials in Nuclear Power Systems - Water Reactors, F. P. Ford, S. M. Bruemmer, and G. S. Was, eds., The Minerals, Metals, and Materials Society, Warrendale, PA, pp. 207-213, 1999.

156. Amzallag, C., G. Baudry, and J. L. Bernard, "Effects of PWR Environment on the Fatigue Crack Growth of Different Stainless Steels and Inconel Type Alloy," Proc. IAEA-Specialists Meeting on Subcritical Crack Growth, NUREG/CP-0044, Vol. 1, pp. 263-294, 1983.

157. Van Der Sluys, W. A., B. A. Young, and D. Doyle, "Corrosion Fatigue Properties on Alloy 690 and Some Nickel-Based Weld Metals," Assessment Methodologies for Preventing Failure: Service Experience and Environmental Considerations, PVP Vol. 410-2, R. Mohan, ed., American Society of Mechanical Engineers, New York, pp. 85-91, 2000.

158. Psaila-Dombrowski, M. J., C. S. Wade, J. M. Sarver, W. A. Van Der Sluys, and P. E. Doherty, "Evaluation of Weld Metals 82, 152, 52, and Alloy 690 Stress Corrosion Cracking and Corrosion Fatigue Susceptibility," Proc. of the 8th Intl. Symp. on Environmental Degradation of Materials in Nuclear Power Systems - Water Reactors, S. M. Bruemmer, ed., American Nuclear Society, La Grange Park, IL, pp. 412-421, 1997.

159. Lindstrom, R., P. Lidar, and J. Lagerstrom, "Crack Growth of Alloy 182 in Simulated Primary Side PWR Environment," Proc. of the 8th Intl. Symp. on Environmental Degradation of Materials in Nuclear Power Systems - Water Reactors, S. M. Bruemmer, ed., American Nuclear Society, La Grange Park, IL, pp. 422-429, 1997.

160. James, L. A., and W. J. Mills, "Fatigue-Crack Propagation Behavior of Wrought Alloy 600 and Weld-Deposited EN82H in an Elevated Temperature Aqueous Environment," Service Experience, Structural Integrity, Severe Accident, and Erosion in Nuclear and Fossil Plants, PVP Vol. 303, American Society of Mechanical Engineers, New York, pp. 21-36, 1995.

161. Scott, P. M., "Prediction of Alloy 600 Component Failures in PWR Systems," Proc. of Corrosion '96 Research Topical Symposia, Part 1 - Life Prediction of Structures Subject to Environmental Degradation, NACE, International, Houston, TX, pp. 135-160, 1996.

162. Scott, P. M., and C. Benhamou, "An Overview of Recent Observations and Interpretations of IGSCC in Ni-Base Alloys in PWR Primary Water," Proc. of the 10th Intl. Symp. on Environmental Degradation of Materials in Nuclear Power Systems - Water Reactors, NACE International, Houston, TX, 2001.

163. Amzallag, C., S. Le Hong, C. Benhamou, and A. Gelpi, "Methodology Used to Rank the Stress Corrosion Susceptibility of Alloy 600 PWR Components," Assessment Methodologies for Preventing Failures: Service Experience and Environmental Considerations, PVP Vol. 410-2, Vol. 2, R. Mohan, ed., American Society of Mechanical Engineers, New York, pp. 163-170, 2000.

164. Alexandreanu, B., O. K. Chopra, and W. J. Shack, "Crack Growth Rates of Nickel Alloy Welds in a PWR Environment," NUREG/CR-6907, ANL-04/3, May 2006.

165. White, G., J. Hickling, and C. Harrington, "MRP Development of Crack Growth Rate Disposition Curves for Primary Water Stress Corrosion Cracking (PWSCC) of Thick-Section Alloy 600 Components and Alloy 82, 182 and 132 Weldments," EPRI International PWSCC of Alloy 600 Conference, Santa Ana Pueblo, NM, March 7-10, 2005.

166. White, G. A., J. Hickling, and L. K. Mathews, "Crack Growth Rates for Evaluating PWSCC of Thick-Wall Alloy 600 Material," Proc. of the 11th Intl. Symp. on Environmental Degradation of Materials in Nuclear Power Systems - Water Reactors, NACE International, Houston, TX, pp. 166-179, 2003.

167. Bamford, W. H., J. P. Foster, and R. S. Pathania, "An Investigation of Alloy 182 Stress Corrosion Cracking in Simulated PWR Environment," Proc. of the Ninth Intl. Symp. on Environmental Degradation of Materials in Nuclear Power Systems - Water Reactors, F. P. Ford, S. M. Bruemmer, and G. S. Was, eds., The Minerals, Metals, and Materials Society, Warrendale, PA, pp. 279-294, 1999.

168. Bamford, W. H., J. P. Foster, K. R. Hsu, L. Tunon-Sanur, and A. McIlree, "Alloy 182 Weld Crack Growth, and its Impact on Service-Induced Cracking in Operating PWR Plant Piping," Proc. Tenth Intl. Conf. on Environmental Degradation of Materials in Nuclear Power Systems - Water Reactors, NACE International, Houston, TX, 2001.

169. Le Hong, S., J. M. Boursier, C. Amzallag, and J. Daret, "Measurement of Stress Corrosion Cracking Growth Rates in Weld Alloy 182 in Primary Water of PWR," Proc. Tenth Intl. Conf. on Environmental Degradation of Materials in Nuclear Power Systems - Water Reactors, NACE International, Houston, TX, 2001.

170. Cassagne, T., D. Caron, J. Daret, and Y. Lefevre, "Stress Corrosion Crack Growth Rate Measurements in Alloys 600 and 182 in Primary Loops Under Constant Load," Proc. of the Ninth Intl. Symp. on Environmental Degradation of Materials in Nuclear Power Systems - Water Reactors, F. P. Ford, S. M. Bruemmer, and G. S. Was, eds., The Minerals, Metals, and Materials Society, Warrendale, PA, pp. 217-224, 1999.

171. Magdowski, R., and M. Speidel, "Stress Corrosion Crack Growth of Weld Material Alloy 182 in Simulated PWR Environments," Institute of Metallurgy, Swiss Federal Institute, Internal Report No. 226, Zurich, Jan. 2001.

172. Jacko, R. J., R. E. Gold, G. V. Rao, K. Koyama, and A. Kroes, "Results of Accelerated SCC Testing of Alloy 82, Alloy 182 and Alloy 52M Weld Metals," The Vessel Penetration Inspection, Crack Growth and Repair Conference, Oct. 2, 2003, Gaithersburg, MD, Vol. 1, pp. 413-426, 2003.

173. Attanasio, S., J. V. Mullen, J. W. Wuthrich, W. W. Wilkening, and D. S. Morton, "Stress Corrosion Crack Growth Rates (SCCGRs) for Alloy 182 and 82 Welds," The Vessel Penetration Inspection, Crack Growth and Repair Conference, Oct. 2, 2003, Gaithersburg, MD, Vol. 1, pp. 267-296, 2003.

174. Brown, C. M., and W. J. Mills, "Effect of Water on Mechanical Properties and Stress Corrosion Behavior of Alloy 600, Alloy 690, EN82H Welds, and EN52 Welds," Corrosion **55** (2), 173-186, 1999.

175. Mills, W. J., and C. M. Brown, "Stress Corrosion Crack Growth Rates for Alloy 82H Welds in High Temperature Water," Proc. 11th Intl. Conf. on Environmental Degradation of Materials in Nuclear Power Systems - Water Reactors, NACE International, Houston, TX, pp. 1240-1254, 2003.

176. Tsutsumi, K., H. Kanasaki, K. Yoshimoto, Y. Nomura, S. Asada, and T. Yonezawa, "SCC Growth Rate of Nickel Based Alloy 132 Weld Metal in PWR Water," Proc. 11th Intl. Conf. on Environmental Degradation of Materials in Nuclear Power Systems - Water Reactors, NACE International, Houston, TX, pp. 1255-1265, 2003.

177. Alexandreanu, B., and G. S. Was, "A Priori Determination of the Sampling Size for Grain Boundary Character Distribution and Grain Boundary Degradation Analysis," Phil. Mag. A, **81** (8), 1951-1965, 2001.

This page is intentionally left blank

NRC FORM 335
(9-2004)
NRCMD 3.7

U. S. NUCLEAR REGULATORY COMMISSION

BIBLIOGRAPHIC DATA SHEET

(See instructions on the reverse)

1. REPORT NUMBER

NUREG/CR–4667. Vol. 36
ANL–06/33

2. TITLE AND SUBTITLE

Environmentally Assisted Cracking in Light Water Reactors, Annual Report, January–December 2005

3. DATE REPORT PUBLISHED

MONTH	YEAR
	2006

4. FIN OR GRANT NUMBER

Y6388

5. AUTHOR(S)

B. Alexandreanu, Y. Chen, O. K. Chopra, H. M. Chung, E. E. Gruber, W. J. Shack, and W. K. Soppet

6. TYPE OF REPORT

Technical

7. PERIOD COVERED (Inclusive Dates)

8. PERFORMING ORGANIZATION – NAME AND ADDRESS *(If NRC, provide Division, Office or Region, U.S. Nuclear Regulatory Commission, and mailing address; if contractor, provide name and mailing address.)*

Argonne National Laboratory
9700 South Cass Avenue
Argonne, IL 60439

9. SPONSORING ORGANIZATION – NAME AND ADDRESS *(If NRC, type "Same as above": if contractor, provide NRC Division, Office or Region, U.S. Nuclear Regulatory Commission, and mailing address.)*

Division of Fuel, Engineering and Radiological Research
Office of Nuclear Regulatory Research
U.S. Nuclear Regulatory Commission
Washington, DC 20555–0001

10. SUPPLEMENTARY NOTES

W. H. Cullen, Jr., NRC Project Manager

11. ABSTRACT (200 words or less)

This report summarizes work performed from January to December 2005 by Argonne National Laboratory on fatigue and environmentally assisted cracking in light water reactors (LWRs). Existing test data for carbon and low–alloy steels and austenitic stainless steels in air and LWR environments have been reviewed, and an approach for incorporating the effects of LWR environments into ASME Section III fatigue evaluations has been described. Crack growth rate tests and slow strain rate tensile tests are being conducted on various austenitic stainless steels irradiated in the Halden boiling water reactor. Results are given on the susceptibility of these materials to stress corrosion cracking as a function of fluence level, water chemistry, and material chemistry. The susceptibility of austenitic stainless steel core internals to stress corrosion cracking and void swelling in pressurized water reactors is also being evaluated. These materials had been irradiated in the BOR-60 reactor in Russia to doses up to 20 dpa. Crack growth rate data in pressurized water reactor environments are presented for Ni alloys and laboratory-prepared Ni alloy welds to determine their susceptibility to environmentally enhanced cracking under various load conditions.

12. KEY WORDS/DESCRIPTORS *(List words or phrases that will assist researchers in locating this report.)*

Fatigue Crack Initiation
Crack Growth Rate
Irradiation–Assisted Stress Corrosion Cracking
Radiation–Induced Segregation
Stress Corrosion Cracking
Nickel Alloys
Austenitic Stainless Steels
Fracture Toughness J–R Curve

13. AVAILABILITY STATEMENT

unlimited

14. SECURITY CLASSIFICATION

(This Page)
unclassified

(This Report)
unclassified

15. NUMBER OF PAGES

16.PRICE